ANALYSIS OF HEAT TRANSFER IN SILICATE SLAGS

by

JOHN DANA NAUMAN

B.S., South Dakota School of Mines and Technology

Rapid City, South Dakota

1972

Submitted in partial fulfillment of the requirements

for the degree of

DOCTOR OF SCIENCE

at the

Massachusetts Institute of Technology

September 1976

Signature of Author .....
Department of Materials Science and Engineering
August 9, 1976

Certified by .....
Thesis Supervisor

Accepted by .....
Chairman, Departmental Committee on Graduate Students

ABSTRACT

ANALYSIS OF HEAT TRANSFER IN SILICATE SLAGS

by

JOHN DANA NAUMAN

Submitted to the Department of Materials Science and Engineering on August 9, 1976 in partial fulfillment of the requirements for the degree of Doctor of Science.

The heat transfer in ferrous silicate slags was studied by measuring the rise in the temperature of a cold metal sphere which was immersed in the liquid slag. Several liquid silicates at iron saturation were studied. These silicates included synthetic iron refining and copper smelting slags. The experimental variables were the initial temperature of the sphere, the size of the sphere, the composition and density of the sphere, the temperature of the liquid slag, and the convection of the liquid slag around the sphere. The types of convection were natural convection, forced convection by spinning the sphere, and forced convection by bubbling gas into the slag.

To provide a general understanding of the heat transfer from the liquid slag to the cold metal sphere, a mathematical model of the flow of heat was developed and tested. The model was used to calculate the temperature distribution in the metal sphere and the solid slag shell which froze on the sphere using the known properties of the slag and metal. The rates of heating of the sphere in the slag were calculated with this model and compared to the rates observed in the experiments. It was shown that the most critical properties which determine the heating of the sphere are the temperature at the surface of the solid slag shell and the thermal conductivity of this solid slag. Most of the slags in this study solidified and melted with a smooth or planar solid-liquid interface which was at the solidus temperature of the slag. It was also shown that convection in the liquid slag had a large effect on the heating of the metal sphere.

The mathematical model was also used to simulate conditions of an electric furnace-pellet feeding operation. This simulation predicted the melting times of various iron pellets in the slag of an electric furnace. It was shown that the most critical factors controlling the melting of the pellets in the furnace were the density of the pellets and the heat transfer coefficient in the liquid slag.

Thesis Supervisor: John F. Elliott

Title: Professor of Metallurgy

TABLE OF CONTENTS

LIST OF TABLES

LIST OF FIGURES

LIST OF FIGURES (Cont'd.)

LIST OF FIGURES (Cont'd.)

LIST OF FIGURES (Cont'd.)

LIST OF FIGURES (Cont'd.)

LIST OF FIGURES (Cont'd.)

LIST OF FIGURES (Cont'd.)

LIST OF FIGURES (Cont'd.)

LIST OF TERMS

A_A area of alumina sphere

A_c cross-sectional area of bubble column

A_i surface area of finite element i

A_M surface area of metal sphere

A_n surface area of iron pellet n in an electric furnace

A_R surface area of liquid-solid slag interface

C specific heat

C_A specific heat of alumina

C_L specific heat of liquid slag

C_M specific heat of metal

C_S specific heat of solid slag

d diameter of a pore

D diameter of the sphere

f_{rad} fraction of radiation heat flux in a boundary layer

f_L fraction of slag solidifying at the liquidus temperature

f_s fraction of slag solidifying at the solidus temperature

F gas flow rate

$\tilde{T}$ view factor

$\bar{h}_L$ heat transfer coefficient in liquid slag

h_I interfacial resistance

K thermal conductivity

K^* thermal conductivity of non porous solid

K_A thermal conductivity of alumina

K_c thermal conductivity by phonons

K_p thermal conductivity of in pore

K_r thermal conductivity by photons

K_L thermal conductivity of liquid slag

K_M thermal conductivity of metal

K_S thermal conductivity of solid slag

ℓ_j distance from the farthest temperature node to the moving boundary

L_j distance from the center of the sphere to the moving boundary

M mass feeding rate of iron pellets

N total number of pellets in an electric furnace

N_{Gr} Grassoff number

N_{Mo} Morton number

$\bar{N}_{Nu}$ Nusselt number

$\bar{N}_{Nu}$ power dissipation Nusselt number

N_{Pr} Prandlt number

N_{Re_b} bubble Reynolds number

N_{Re_o} orifice Reynolds number

N_{Re_s} spinning Reynolds number

N_{Re_v} laminar flow Reynolds number

N_{We} Weber number

q heat flux total

q_c heat flux by conduction

q_r heat flux by radiation

Q_s heat flow in boundary layer

r radial distance

r_b radius of a rising bubble

r_p	radius of an iron pellet
R	radius of the sphere
S	optical thickness
t	time
t_m	melting time
T	temperature
$T_{i,j}$	temperature of finite element i at time j
T_M	temperature of metal
T_n	temperature of the surface of an iron pellet n
T_p	temperature in a pore
T_o	initial temperature of the sphere
T_s	temperature of the solid slag
T_∞	temperature of the bulk liquid
U_s	Stokes velocity
U	overall heat transfer coefficient
V_f	velocity of flowing fluid
V_b	velocity of rising bubble
V_i	volume of finite element i
V_M	volume of metal present
X	horizontal distance
y	vertical distance
Y	height of liquid slag
Q_c	heat flow into a furnace by combustion
Q_E	heat flow into a furnace from an electric arc
Q_L	heat loss from a furnace

w	spinning frequency
α_{eff}	effective thermal diffusivity of slag
α_L	thermal diffusivity of liquid slag
α_M	thermal diffusivity of metal
α_s	thermal diffusivity of solid slag
p	linear coefficient of expansion
γ	extinction coefficient
ΔH	heat of fusion of the slag
ΔH_m	heat of fusion of the metal
ΔH_p	enthalpy for heating and melting porous iron
ΔT	DTA temperature difference between the reference and the sample
ε_A	total normal emissivity of alumina
ε_{Ni}	total normal emissivity of nickel
ε_{Pt}	total normal emissivity of platinum
ε_S	total normal emissivity of solid slag
θ^*	solidus fraction
θ	dimensionless temperature
λ	bulk absorption coefficient
μ	viscosity
ρ_L	density of liquid slag
ρ_M	density of metal
ρ_p	density of porous iron
ρ_s	density of solid slag
σ	Stephan Boltzman constant

τ	dimensionless time
ϕ_1	volume fraction of phase 1
ϕ_2	volume fraction of phase 2
ϕ	volume fraction of rising bubbles
ψ	pore fraction

ACKNOWLEDGEMENTS

The author wishes to express his sincere appreciation to Professor John F. Elliott for his critical guidance and valuable discussions which were essential to the completeness of the work and the application of this investigation to practical conditions.

The author also wishes to thank Professors Warren R. Rosenhowe and Borivoje B. Mikic for their very helpful discussions on the treatment of the heat transport equations in the presence of a moving boundary.

The National Science Foundation is gratefully acknowledged for their financial support.

I. INTRODUCTION

Silicate slags are important as heat transfer media in pyrometallurgical operations and fossil fuel fired boilers and turbines. Liquid slag transfers heat to particles of metal, flux, and oxides which are normally added during the refining in pyrometallurgical operations. The slag becomes the sole source for heating and melting of the particles, when they become entrapped in the slag layer. Also, solid and liquid slag which collect in boilers and turbines form barriers to the transfer of heat to the tubes and walls and provide a corrosive environment.

Several factors are important in the determination of heat transfer in silicate slags. The thermal conductivity of the slag is the most important of these factors. It depends upon the slag composition, temperature, and even the structure of the solid slag. The melting temperature of the slag, the convection in the liquid, and the properties of other materials present in the immediate environment are also factors in the heat transfer in silicate slags.

The purpose of the present investigation is to analyze the heat transfer from a liquid slag to a cold metal particle. The investigation is divided into two stages. First, in a specially designed laboratory experiment, the effects of the slag composition, the liquid slag temperature, the convection in the liquid, and the composition in the metal sphere are measured. Then a mathematical model is developed which simulates the heat transfer to a cold metal particle immersed in a liquid slag. This mathematical model uses the available data on the

thermal properties of the silicate slags and various boundary conditions for the solidification and melting of the slag on the metal particle.

The experimental results and the mathematical model are compared to analyze the effects of the thermal conductivity of the slag, the convection in the liquid slag, the solidification and melting of the slag, and the properties of the metal particle. The mathematical model is also modified to simulate the melting of prereduced iron particles in an electric furnace slag.

II. LITERATURE SURVEY

There are three general areas which are essential for this study of heat transfer in silicate slags: 1) measurements of the thermal conductivity and thermal diffusivity of liquid and solid slag, 2) practical heat transfer problems encountered in the use of silicate slags for metallurgical refining and coal combustion, and 3) mathematical models of heat transfer associated with a moving boundary.

II.A. Thermal Properties of Slag

Relatively few measurements of thermal conductivity and bulk radiation transport for silicate slags are available. These measurements indicate the factors which control heat transfer and directly apply to heat transfer in the slags in which the measurements were made. Radiation transport may be especially important for silicate slags because they are semi-transparent and allow substantial heat transfer by photons in the liquid and glassy states.

Fine and Elliott (1, 3) measured the thermal diffusivity and radiation transport of several liquid synthetic steelmaking slags. Using a cylindrical slag sample, the thermal diffusivity was obtained by measuring the phase shift between a periodic current impressed on a wire at the center of the sample and the temperature response at the outer wall. They measured the thermal diffusivity at various concentrations of iron oxide and various lime to silica ratios. Most of these slags were prepared at iron saturation and had very low concentrations of ferric (III) iron. The results of these measurements of liquid slags containing

between 11.9 wt.% FeO and 20.9 wt.% FeO, with a lime to silica ratio, B, equal to 1.0 and 1.5 were represented by the Equation (1)

$$\alpha_{eff} = 0.001\ (1.5-0.5B) + 0.018\ \frac{(T/1500)^3}{(wt.\%\ FeO)}\ 0.8 \qquad (1)$$

$$B = \frac{wt.\%\ CaO}{wt.\%\ SiO_2} \qquad T < 1750°K$$

with an error of 10%. Apparently the thermal diffusivity decreases with increasing wt.% FeO because of decreasing radiation transport in the bulk of the slag. The effect of lime to silica ratio, B, on the effective thermal diffusivity was traced to the probable increase in the mean free path, L, for photon and phonon conduction as the viscosity of the slag was reduced by the addition of lime.

Fine and Elliott (1, 3) suggested that the radiation contribution to transport in these iron oxide slags was of the same order as the conduction contribution (phonon conduction). The transport of thermal radiation in a semi-transparent medium affects the temperature distribution, depending upon the optical thickness of the specimen. The optical thickness is defined

$$s = \lambda x \qquad (2)$$

where λ is the bulk absoption coefficient and x is the thickness of the specimen. If the optical thickness of the specimen is greater than about 4, then the thermal radiation contribution to the conduction can be simply added to the phonon conduction to constitute an "effective" thermal conductivity. The apparatus used by Fine and Elliott was designed so that the specimens were sufficiently optically thick for the measurements of "effective" thermal diffusivity.

Thermal radiation through a semi-transparent specimen may also be important in determining heat transfer at a phase boundary. The absorption of thermal radiation at a solid boundary in a liquid glass specimen was modeled and measured at a steady state by Eryou and Glicksman (74). A non-linear temperature distribution in the glass and an increase in the heat flux at the boundary was observed, which depended upon the magnitude of the bulk absorption coefficient in the glass. The bulk absorption coefficient for glassy slags at 0 to 14% FeO concentrations was measured by Fine and Elliott (3). The scattering coefficient for polycrystalline slags also limits the transport of thermal radiation through a specimen. In most cases the scattering coefficient is several orders of magnitude greater than the bulk absorption coefficient.

More recent measurements with the periodic steady state apparatus, reported by Nauman, Foo and Elliott (4) of ferrous silicates and synthetic copper smelting slags, indicated no general relationship between slag composition and effective thermal diffusivity. The thermal diffusivity of the solid slag was also measured in the periodic source apparatus. The typical value of thermal diffusivity of a ferrous silicate, composed principally of fayalite, was 0.0042 cm^2/sec. This value applied for the liquid as well as the solid slag. The effect of radiation on the heat transfer in these slags was not appreciable due to the very high concentration of FeO (50.1 to 69.5%). All of these slags were prepared at iron saturation.

Braun (13) measured the thermal conductivity of several coal ash slags with a calibrated thermal gradient technique. These slags were

obtained from a slagging boiler and contained 20 to 64.4 wt.% Fe_2O_3. Under various oxygen pressures, which attempted to simulate boiler conditions, the conductivity increased with exposure to oxidizing atmosphere. This increase was probably due to the oxidation of ferrous iron to the ferric state.

Gibby and Bates (6) measured the thermal diffusivity of basalt using a high temperature laser pulse technique. Similar to other measurements on terrestrial rock (5), the thermal diffusivity decreased with increasing temperature near the melting point. A value of about 0.0045 $cm^2/sec.$ was recorded for a liquid basalt about 1400°C.

Using the same laser pulse technique, Bates (7) measured the thermal diffusivity of several synthetic and real power plant coal ash slags. His measurements indicated that the diffusivity of the solid slag decreased with increasing temperature. This contradicts the measurements made by Braun in which the thermal conductivity of solid coal ash increased with increasing temperature. Also Bates' measurements demonstrated that slags of nearly identical compositions have distinctly different thermal diffusivities. The only explanation given for the different diffusivities was that the degree of crystallization and heat treatment seemed to have an effect. The microstructure of these nearly identical slags may have been quite different, but there is insufficient information presented to asses this.

In general, the thermal diffusivity from available data on silicate slags ranges from 0.003 to 0.007 $cm^2/sec.$ for both the high temperature

solid and liquid. The works of Bates and Braun demonstrated that solid slags which have similar compositions may not exhibit the same thermal conductivity of thermal diffusivity, if the slags are given different treatments.

II.B. Practical Slag Heat Transfer

There are several practical processes in metallurgical operations and electric power generation where heat transfer in the slag is critical. Some of these processes are electric furnace steelmaking with reduced iron pellets, electroslag remelting, strand casting with a slag flux, coal fired boilers, and open cycle magnetohydrodynamic generators.

The continuous charging of reduced iron pellets into an electric furnace may be limited by heat transfer in the refining slag layer within the furnace. Many of the present day reduced pellets have densities less than that of the refining slag, and the melting of these pellets is accomplished almost entirely within the slag layer. Sibakin et al. (14) reported that such a practice with reduced iron pellets was feasible, if precautions were taken to minimize the freezing of slag and pellets into "islands". Formation of these islands was greatly affected by the distribution of pellets in the furnace and convection in the liquid slag.

In the electroslag remelting process, heat transfer in the slag is extremely critical for melting to electrode and solidification of the ingot in the copper mold. Heating in this process is primarily by joule heating of the slag contained between the electrode and the formed ingot. Mitchell and Joshi (15) determined that among the most important factors controlling

the heat generation in the remelting of an ingot were the electrical and thermal properties of the slag. Also the depth of the liquid metal pool and thus the solidification of the ingot depended upon the thermal insulation by the layer of slag that forms on the ingot.

In boilers which are fired with coal, slag forms from the ash on the fire side of the tube walls. This slag increases the resistance of the walls to heat flow, so the burner temperature must be increased to maintain the operation of the boiler. At the higher temperatures the flow of heat through the slag is irregular because there are variations in the thickness of the slag and the radiation properties of the surface (57). A thin layer of slag or a large radiation absorption results in catastrophic tube wall temperatures (68, 69). Similarly, in the technology of open cycle magnetohydrodynamic power systems, the thermal properties of the ash and slag become critical. At wall temperatures below 1700°C, Bogdanska et al. (12) reported that a significant quantity of slag condenses. The condensation and freezing of slag was controlled by heat transfer in the walls and slag. It was found that the slag coating on the electrodes and insulators caused severe corrosion of oxide electrodes and insulators, while actually protecting the metal electrodes. Therefore the presence of the condensed layer of slag can be very critical to the operation of the generator.

II.C. Heat Transfer at a Phase Boundary

Liquid slag solidifies on the surfaces of cold metal particles refractory tubes, and walls in practical operations. With the presence of solids and liquids, heat transfer in these systems involves a moving

solid-liquid phase boundary accompanied by absorption or release of the enthalpy of fusion. The heat balance at the moving boundary is given by

$$K_L \left.\frac{dT}{dX}\right|_L - K_S \left.\frac{dT}{dX}\right|_S = \rho_s \Delta H \frac{dL}{dt} \qquad (3)$$

where K_L and K_S are the thermal conductivities of the liquid and the solid slag, respectively; ρ_s is the density of the solid slag, ΔH is the enthalpy of fusion; and dL is the change in the thickness of the solid slag. The temperature at this boundary may be fixed at a melting temperature; it may reflect under cooling during solidification or overheating during melting; or, since most slags melt over a range, the boundary temperature may vary over this melting range.

Mathematical models of heat transfer in the presence of a moving boundary and flowing liquids have been investigated only for specific conditions as yet. The exact solutions due to Stefan and Newmann (22) apply to the more elementary problems of solidification of a stationary liquid at the melting temperature, bounded by a plane wall at a constant temperature. Goodman's integral method has been applied assuming solidification on a plane wall of uniform and constant temperature, and assuming constant heat flux from the liquid to the solid phase (23, 24, 26, 27). Variational methods, such as those developed by Biot and Green (28, 29) have been applied to moving boundary problems for cylindrical and spherical walls. However, the evaluation of the integrals in all of these methods presents considerable difficulties when dealing with problems of solidification and convection in the liquid boundary layer. Also,

according to the investigations by Megerlin (75), the Goodman integral method does not yield very accurate results in problems of melting solidification.

Numerical methods can become very complex due to the nonlinear boundary conditions for heat flux at the phase boundary. The usual procedure is to estimate the thickness of the solid layer, then to determine the temperature distribution, which provdes a new value for the thickness of the layer (33, 34). Several numerical methods have also been proposed which lump together the specific heat and the enthalpy of fusion at the melting temperature of the materials (30, 31, 32, 35). In these methods the moving interface is never actually defined.

A further survey of the previous work on mathematical models and convection in the liquid, which apply directly to the present experimental study, is included in Chapter V on mathematical modeling.

III. EXPERIMENTAL

In this chapter the design and the procedure of the laboratory experiments for the study of heat transfer in silicate slags are described. The principal laboratory experiments consisted of immersing a cold metal sphere in a "semi-infinite" liquid slag. The metal sphere enters the slag at a predetermined temperature, and the temperature at the center of the sphere is measured continuously. From this continuous measurement of temperature it is possible to determine the transfer of heat from the slag to the sphere as a function of time. During this experiment the flow of liquid slag was controlled by spinning the sphere, or holding the sphere static and stirring with rising gas bubbles. The experiments were conducted in different compositions of liquid slag at various temperatures. The metal objects which were immersed into the liquid slag were nickel spheres, nickel cylinders, copper spheres, and porous iron spheres.

During the immersion of the metal sphere into the liquid slag, the slag solidifies around the cold sphere and then melts away as shown in Figure III-1. Stage 1 shows the sphere and the slag at constant temperatures upon the initial immersion. Stage 2 shows the slag shell solidifying on the sphere, and the temperature distribution within the sphere as it begins to heat. Stages 3 and 4 show the slag shell at a maximum thickness and as it begins to melt. After the slag shell is completely remelted, stages 5 and 6 show the sphere continuing to heat to the slag bath temperature. Heat transfer in such a system is

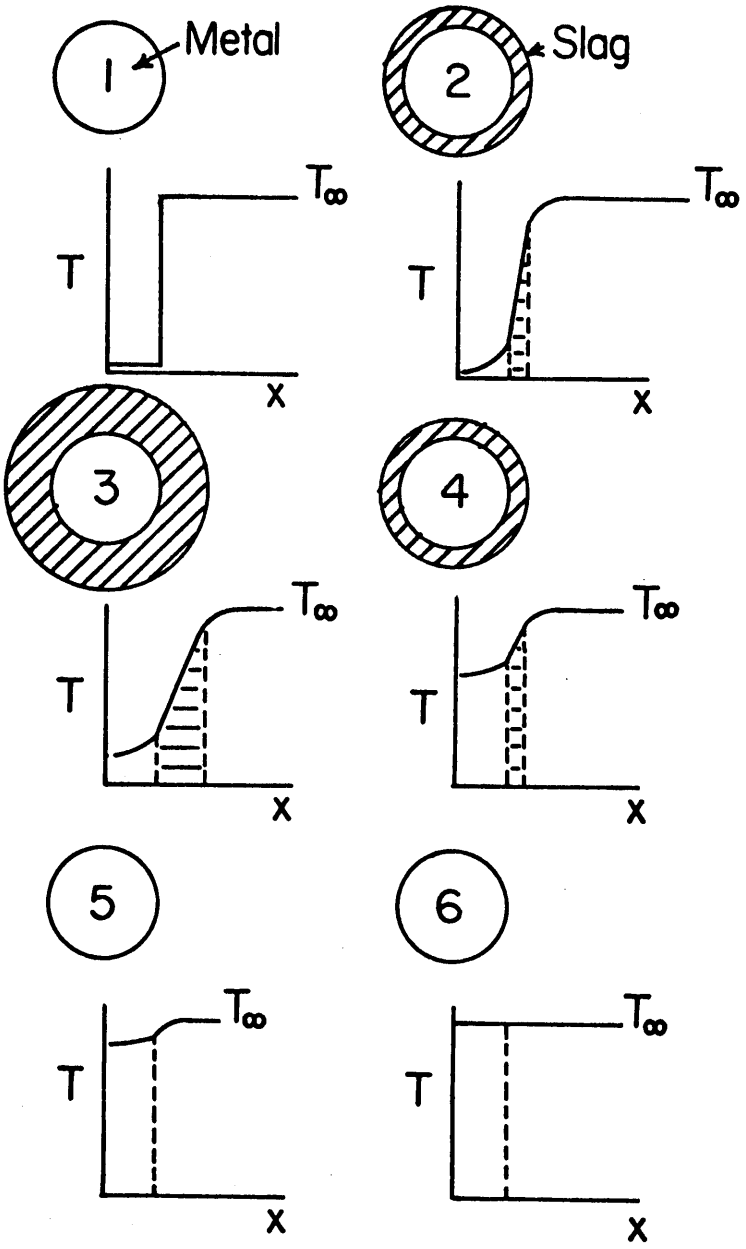

Figure III-1 Six stages of heating a cold metal sphere in a liquid slag

determined by the thermal properties of the metal sphere, the solid slag, and the convection in the liquid.

The melting range of the slags studied was measured by differential thermal analysis. This melting range was necessary for the mathematical model which is described in Chapter V.

III.A. Preparations for Experiments

III.A.1. Preparation of the Slag

The slags were prepared for these experiments by mixing together reagent grade powders of pure oxides to obtain the compositions shown in Table III-1. After mixing the powders for 10 to 20 hours by tumbling, the mixture was charged into an iron crucible and melted. The iron crucible consisted of a 21 cm. section of a 6 inch diameter steel tube (0.7 wall thickness) which was closed on the bottom by a 1/2 inch steel plate welded to the tube. On the top of this iron crucible was placed a lid of 1/4 inch steel plate with a 5 cm. hole in the center. This lid prevented the formation of a solid slag crust on the top of the liquid.

The crucible was surrounded by bubble grain alumina and high temperature refractory brick as shown in Figure III-2. Heat was applied to the iron crucible by an induction furnace (Tocco Meltmaster, 50KVAR, 9720 Hertz). When an optical pyrometer sighted on the inside wall of the crucible, the temperature was increased to 10°C above the melting temperature of the slag mixture. This temperature was held constant until most of the mixture became liquid, and then more powder was stirred

Table III-1. Calculated Compositions of Slags Based on the Mixed Powders.**

Slag	weight percent							Description
	Total Fe	FeO	Fe_2O_3	SiO_2	CaO	Al_2O_3	Other	
N-2W	60.2 (60.1)*	74.4	3.2	22.4				wustite saturation, near the fayalite-wustite peritectic
N-FA	59.2 (58.9)	73.5	3.0	23.5				Fayalite-wustite peritectic
N-1W	58.1 (58.1)	72.9	2.6	24.6				Fayalite saturation, near the fayalite-wustite peritectic
N-FB	54.7 (54.7)	69.5	1.8	28.7				Fayalite (Fe_2SiO_4)
N-FC	47.6 (48.6)	60.5	1.4	38.1				Fayalite-silicate peritectic
N-1A	43.2 (43.5)	55.1	1.2	34.7		9.0		N-FC + 9% Al_2O_3
N-2A	39.3 (40.3)	50.1	1.1	31.5		17.3		N-FC + 18% Al_2O_3
N-CA	43.2 (43.1)	55.1	1.2	34.6	9.1			N-FC + 9% CaO
N-1CU	32.8 (35.2)	40.5	5.0	40.5	7.0	5.0	1.0 MgO; 1.0 S	high silica synthetic copper smelting slag
N-2CU	38.5 (40.2)	45.5	5.0	35.5	7.0	5.0	1.0 MgO; 1.0 S	high FeO synthetic copper smelting slag
N-IR	11.0	14.2		31.4	31.4	12.5	10.5 MgO	synthetic steelmaking

*Found by analysis as described in Appendices C and G.

**Mixed composition at iron saturation based on available phase diagrams.

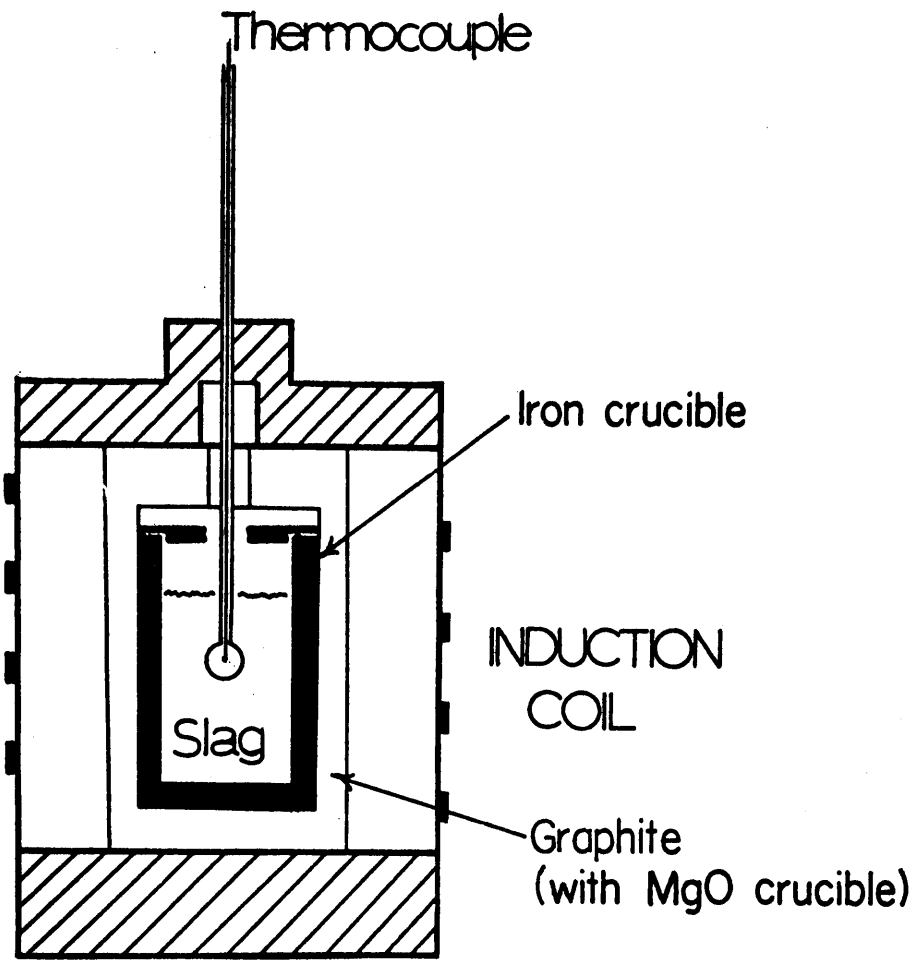

Figure III-2 Experimental furnace for heat transfer measurements

in and melted to obtain a liquid slag of 14 cm. depth. Before starting any experiments the liquid slag was kept at a constant temperature for 30 to 40 minutes. The single charge could be reused for several experiments.

Because of the higher working temperatures for slag N-IR (1300-1400°C), a MgO crucible (1.4 cm. wall thickness) was used instead of the iron crucible. Heat was provided by a 1.5 cm. thick graphite susceptor surrounding the MgO crucible. A 3 cm. thick graphite lid with a 5 cm. hole in the center prevented the formation of a slag crust on the top of the liquid.

Samples of the slag were taken from the liquid and analyzed for total iron to check the expected composition (see Appendix G).

III.A.2. Preparation of the Metal Spheres

The nickel and copper spheres were prepared by investment casting, while the porous iron spheres were prepared by sintering iron powder.

The spherical patterns for the investment molds were made in the following manner. Standard ball bearings of 1 1/4, 1, and 3/4 inch diameter were mounted separately on wax pedestals. They were then surrounded by silicone rubber (Allied Resin Co., RTV 664). After the silicone rubber hardened (24 hours) the ball bearings were removed by carefully cutting along a vertical cross-section of the rubber block with a sharp knife. By leaving a portion of the rubber uncut, the rubber mold could be reassembled and filled with wax.

These spherical wax patterns were then used to make lost wax investment molds. A pattern was attached to a cylindrical wax stem which was 0.8 cm. in diameter and 1.0 cm. long. Two or three of these assemblies were then attached to a cylindrical riser which was 3.0 cm. in diameter and 6 cm. long, as suggested by Taylor et al. (64). A 0.8 cm. diameter runner and a 1.0 cm. diameter sprue were fitted to the bottom of the riser, and would funnel the liquid metal into the riser during pouring. The entire wax pattern was inverted on a metal into the riser during pouring. The entire wax pattern was inverted on a metal plate, and surrounded with a section of steel pipe. Ferrous investment material (Ransom and Randolf 711) was mixed, 10 parts to 1 part water, and poured around the wax pattern. The green mold was then vibrated to eliminate gas bubbles.

After setting overnight, the green mold was removed from the plate and placed in a furnace at 100°C for 4 to 12 hours to remove the wax. The temperature of the mold was then increased at a rate of 100 to 200 degrees per hour to reach 900°C. At this temperature the investment mold was allowed to burn clean, set, and reach a steady temperature. Then the mold was removed from the furnace and was ready for casting.

For the nickel castings, pure nickel shot was melted inductively and brought to 1550°C in a dense MgO crucible (15.2 cm. deep and 1 cm. wall thickness). The temperature was monitored by an optical pyrometer. To deoxidize the melt, 1 to 2 grams of aluminum were added just before the nickel was poured into the hot investment mold. For the copper

castings, electrical grade copper was melted in a graphite crucible which was heated inductively. Argon was bubbled into the melt for 3 minutes prior to casting to help purge oxygen from the copper. The copper was poured at 1150°C.

The nickel and copper castings were removed from the investment after 4 to 8 hours of cooling. The stem of each sphere was cut close to the riser to remove the sphere. The stem was machined to fit into the iron tube (5/16 inch inside diameter) as shown in Figure III-2, and the hole for the thermocouple was drilled to the center of the sphere. While mounted in a lathe the surface of the sphere was lightly sanded and polished with 320 emery paper. Later, the sphere and hole were cleaned with acetone.

The porous iron spheres were sintered using the ferrous investment molds, but in a different configuration. Spherical wax patterns were made from the silicone rubber molds of 3.0 cm. diameter, with cylindrical stems 2.5 cm. long. The spheres with stems were mounted vertically on a metal plate and cast in the ferrous investment material. After the investment was set as described above, the investment mold was removed from the furnace and filled with either 50 mesh iron filings or 100 mesh iron powder. Then iron tubes (5/16" outside diameter 3/16"inside and 2.5 cm. diameter long)were pressed into the iron filings, such that 0.5 cm. of the iron tube extended into the spherical cavity of the investment mold. The tube was carefully centered, straightened, and packed securely in the filings. A small amount of graphite powder was spread on top of the iron filings and the mold to minimize the oxidation during

Table III-2. Properties of Metal Spheres

Metal	Diameter cm.	Density g/cm^3	Thermal Diffusivity $cm^2/sec.$	Specific heat (cal/g-°C)**
Nickel	3.06	8.2	0.14	0.13
Nickel	1.83	8.2	0.14	0.13
Copper	3.06	8.7	0.90	0.11
Iron (50 mesh)	3.06	3.8	*	*
Iron (100 mesh)	3.06	4.5	*	*

*See Section V.F.

**At 800°C

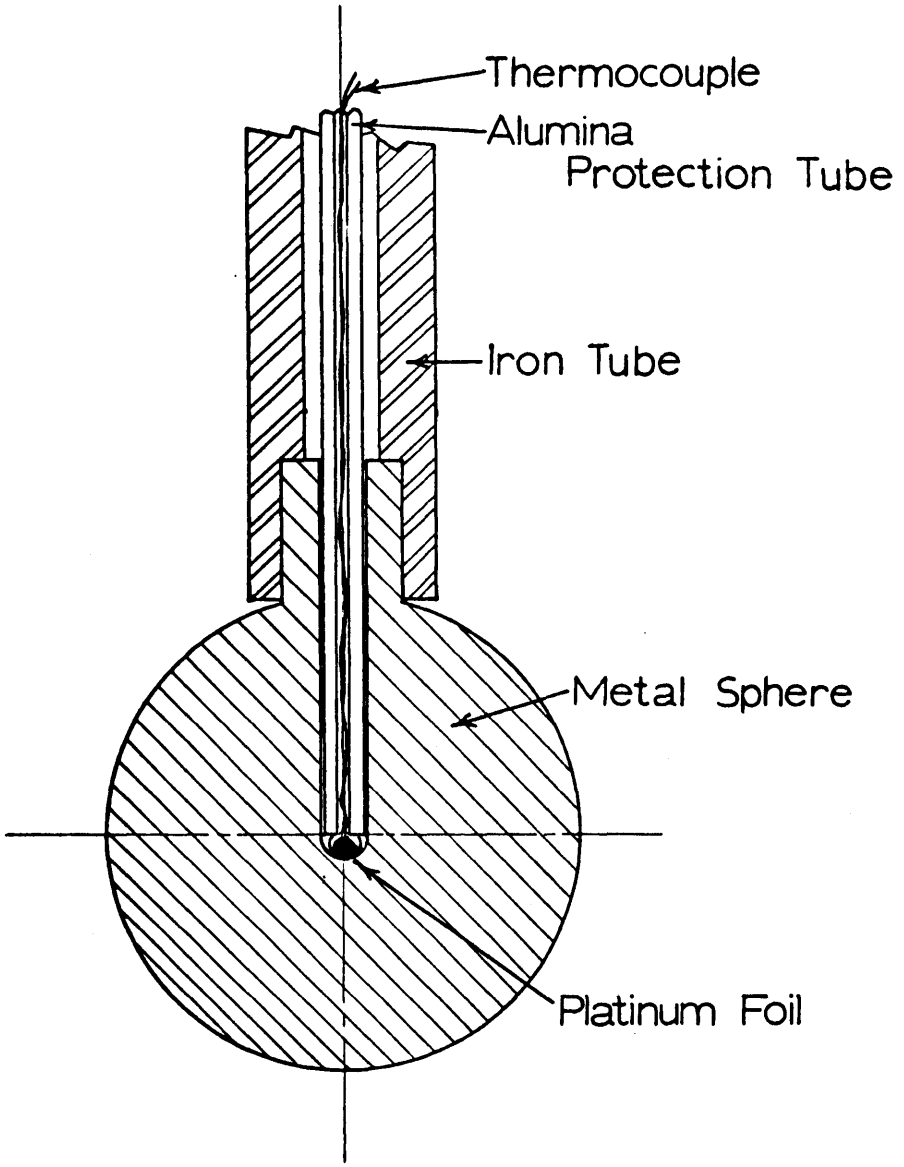

Figure III-3 Metal sphere and iron support tube

sintering. The mold was placed in the furnace and heated to 900°C. After three hours at 900°C the mold was removed and allowed to cool. The sintered spheres were removed very carefully and cleaned. As with the copper and nickel spheres, a 0.3 cm. hole for the thermocouple was drilled carefully into the sphere.

The densities of the metal spheres were calculated from the weight and the size of the spheres and stems. Values at room temperature are given in Table III-2, along with other properties. The estimation of the thermal diffusivity of the porous iron sphere is discussed in Section V.F.

The thermocouple which was inserted into the metal sphere shown in Figure III-3 was a platinum platinum-10% rhodium couple of 10 mil wire. In the experiments with slag N-IR, the thermocouple was protected by a 0.1 cm. thick alumina protection tube. In the experiments with all other slags, the thermocouple bead was protected by platinum foil which was placed in direct contact with the metal sphere. The effects of the protection on the response of the thermocouple are discussed in Appendix A.

The iron tube which supported the sphere was 60 cm. long and 1.2 cm. in diameter. At the bottom end of the iron tube, the metal sphere was held in place with two set screws. The thermocouple wires, which were protected by an alumina insulator, ran from the sphere and along the inside of the tube. The tube was mounted in ball bearing pillow blocks which were fixed to the transite carriage as shown in Figure III-4.

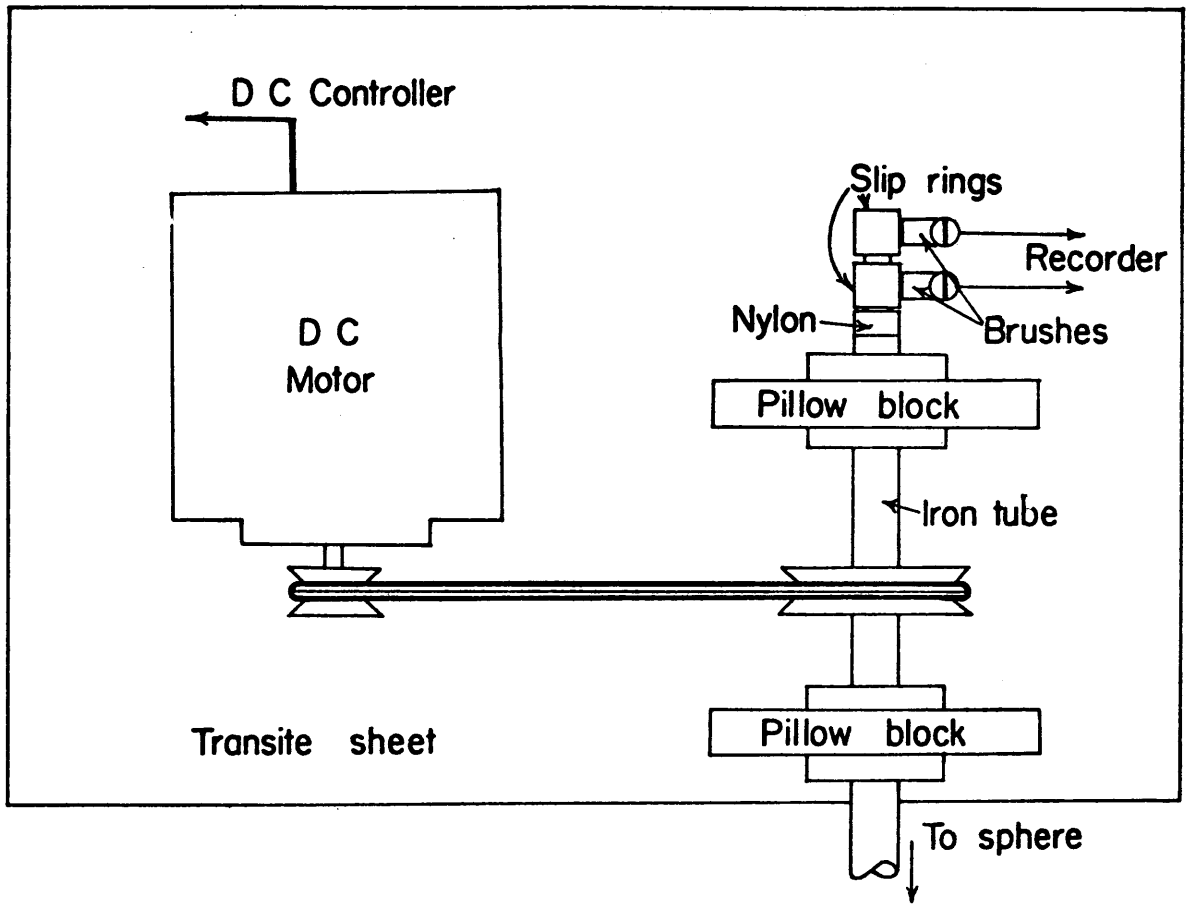

Figure III-4 Transite carriage supporting the DC motor, pillow block bearings and the slip rings and brushes for the spinning tube and sphere

Along with these pillow blocks, a DC motor and a set of electrical contacting brushes were mounted on the carriage. The metal brushes were in contact with two copper slip rings which were connected to the thermocouple wires at the top of the iron tube. These contacting brushes and slip rings allowed the tube and sphere to spin freely about their vertical axis without disturbing the output of the thermocouple.

III.B. Heat Transfer Experiments in Liquid Slag

The experimental conditions for the heat transfer experiments with liquid slag are shown in Table III-3.

III.B.1. Forced Convection by Spinning

Heat transfer experiments were conducted in liquid slag with spinning nickel spheres. Forced convection by spinning produces the conditions of flow which are shown in Figure III-5 (11). The fluid flows vertically toward the sphere at the poles and proceeds spirally along the surface to the equator. There an outward jet forms in the shape of an equatorial plate. Under the conditions of the present experiments in liquid slags, the flow along the surface of the sphere is laminar, based on the empirical criteria (11)

$$\frac{wD^2}{\mu}\rho_L < 10^5$$

where w is the spinning frequency; D is the diameter of the sphere; ρ_L is the density of the liquid; and μ is the viscosity of the liquid slag.

Table III-3. EXPERIMENTAL CONDITIONS

Slag	Run No.	Slag Temperature (°C)	Convection	Metal
N-Fa	10A	1250	0 rpm	Ni (3cm)
	10B	1250	700 rpm	Ni (3cm)
	10C	1250	700 rpm	Ni (3cm)
	10D	1310	700 rpm	Ni (3cm)
N-FB	2A	1250	900 rpm	Ni (3cm)
	2B	1250	900 rpm	Ni (3cm)
	2C	1200	700 rpm	Ni (3cm)
	3A	1220	0 rpm	Ni (1.8cm)
	3B	1220	310 rpm	Ni (1.8cm)
	3C	1220	710 rpm	Ni (1.8cm)
	3D	1220	680 rpm	Ni (1.8cm)
	3E	1220	930 rpm	Ni (1.8cm)
	10F	1250	700 rpm	Ni (3cm)
	15A	1250	700 rpm	(300°C)
	15B	1250	700 rpm	(550°C)
N-FC	11A	1200	700 rpm	Ni (3cm)
	11B	1245	700 rpm	Ni (3cm)
	11C	1275	700 rpm	Ni (3cm)
	19A	1240	700 rpm	Ni (3cm)
	19B	1240	700 rpm	Ni (3cm)
	20A	1230	700 rpm	Fe (50 mesh)
	20B	1230	700 rpm	Cu
	20C	1200	700 rpm	Ni (3cm)
	20D	1220	700 rpm	Ni (3cm)
N-1A	11D	1240	700 rpm	Ni (3cm)
	6A	1230	700 rpm	Ni (3cm)
	6B	1225	700 rpm	Ni (3cm)
N-2A	6C	1220	700 rpm	Ni (3cm)
	4A	1170	700 rpm	Ni (3cm)
	4B	1170	700 rpm	Ni (3cm)
	4C	1205	700 rpm	Ni (3cm)
	4D	1260	700 rpm	Ni (3cm)
	4E	1250	700 rpm	Ni (3cm)
	4F	1140	700 rpm	Ni (3cm)
	4G	1200	700 rpm	Ni (3cm)
N-CA	19C	1240	700 rpm	Ni (3cm)
	19D	1240	700 rpm	Ni (3cm)
	19E	1240	700 rom	Ni (3cm)

Table III-3. EXPERIMENTAL CONDITIONS (Cont'd.)

Slag	Run No.	Slag Temperature (°C)	Convection	Metal
	19C	1240	700 rpm	Ni (3cm)
	9C	1140		(550°C)
	9D	1150		(300°C)
N-2CU	17A	1120	700 rpm	Ni (3cm)
	17B	1130	700 rpm	Ni (3cm)
	17C	1210	700 rpm	Ni (3cm)
	17D	1230	700 rpm	Ni (3cm)
	17E	1220	700 rpm	Ni (3cm)
	17F	1220	50 cm^3/sec	Ni (3cm)
	17G	1200	300 cm^3/sec	Ni (3cm)
N-1W	15C	1230	static	Ni (3cm)
	15D	1230	700 rpm	(500°C)
	15E	1230	700 rpm	Ni (3cm)
	15F	1240	700 rpm	Ni (3cm)
N-2W	15G	1250	700 rpm	Ni (3cm)
	7A	1150	700 rpm	Ni (3cm)
	7B	1170	700 rpm	Ni (3cm)
	7C	1200	700 rpm	Ni (3cm)
N-IR	12A	1360	600 rpm	Ni (3cm)
	12B	1360	600 rpm	Ni (3cm)
	12C	1340	330 rpm	Ni (3cm)
	12D	1350	550 rpm	Ni (3cm)
	8A	1350	700 rpm	Ni (3cm)
	8B	1340	900 rpm	Ni (3cm)
	8C	1350	500 rpm	Ni (3cm)
	8D	1400	700 rpm	Ni (3cm)
	21A	1300	static	Ni (3cm)
	21B	1350	static	Ni (3cm)
	21C	1390	static	Ni (3cm)
	21D	1360	static	Ni (3cm)
	21E	1380	static	Ni (3cm)
	21F	1350	static	Cu

Table III-3. EXPERIMENTAL CONDITIONS (Cont'd.)

Slag	Run No.	Slag Temperature (°C)	Convection	Metal
N-1CU	18A	1200	700 rpm	Ni (3cm)
	9A	1150	700 rpm	Ni (3cm)
	9B	1150	700 rpm	Ni (3cm)
	13A	1160	700 rpm	Ni (3cm)
	13B	1200	700 rpm	Ni (3cm)
	14A	1210	700 rpm	Ni (3cm)
	14B	1240	700 rpm	Ni (3cm)
	14C	1300	700 rpm	Ni (3cm)
	14D	1300	700 rpm	Ni (3cm)
	14E	1230	700 rpm	Ni (3cm)
	18B	1200	0-300 rpm	Ni (3cm)
	18C	1200	300-0 rpm	Ni (3cm)
	16A	1160	700 rpm	Ni cylinder
	16B	1180	700 rpm	Ni (3cm)
	16C	1200	700 rpm	Ni (3cm)
	16D	1200	700 rpm	Fe (100 mesh)
	16E	1200	700 rpm	Fe (50 mesh)
	18D	1200	40 cm^3/sec	Ni (3cm)
	18E	1200	250 cm^3/sec	Ni (3cm)
	18F	1200	410 cm^3/sec	Ni (3cm)
	16F	1200	330 cm^3/sec	Ni (3cm)

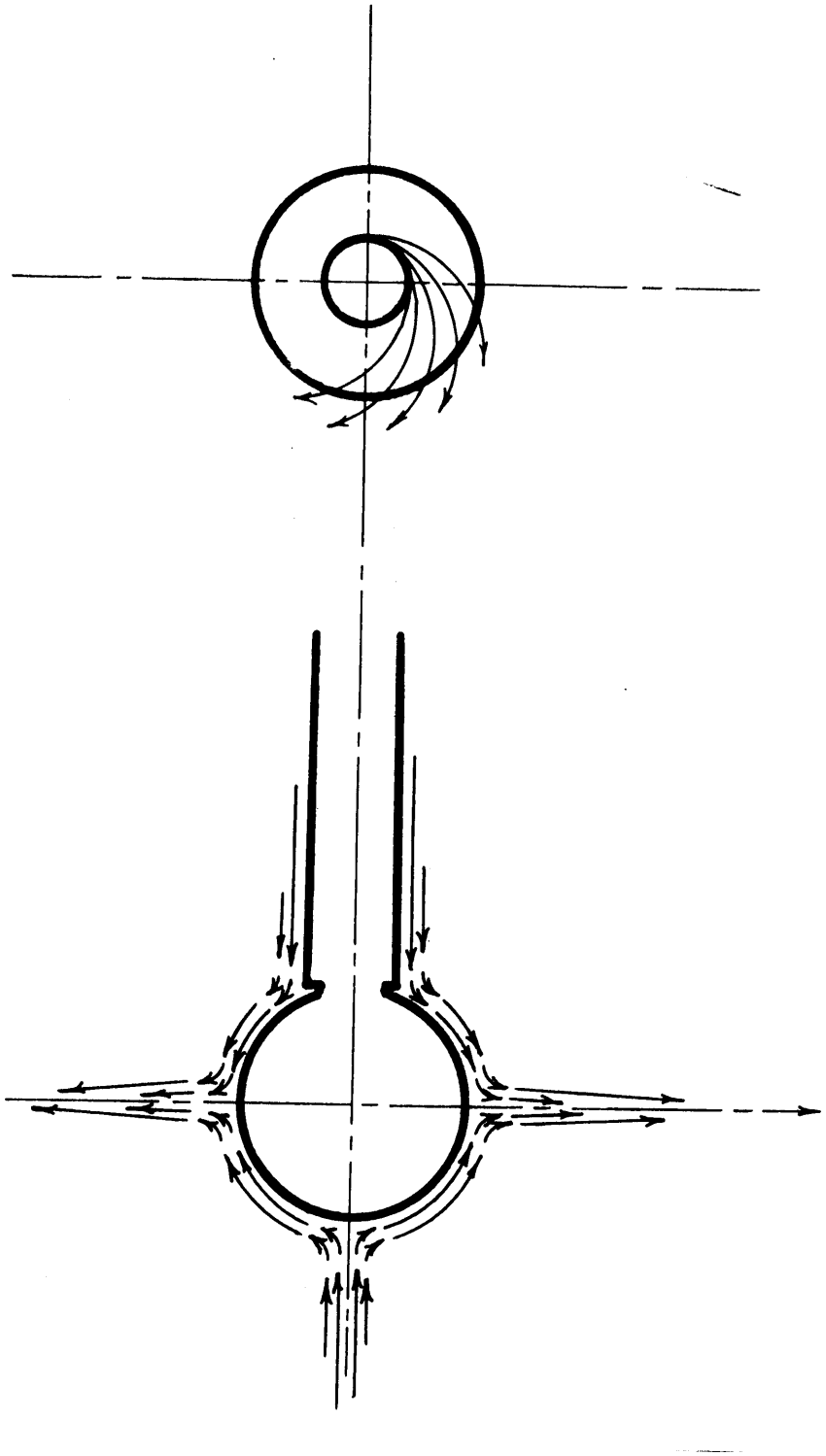

Figure III-5 Fluid flow about a spinning sphere, arrows indicate streamlines

It will be shown in Section V.D. that heat transfer coefficients for forced convection by spinning can be determined from empirical correlations. Also, in Section VI.D.3. it will be shown that the temperature distribution in the liquid boundary layer of a spinning sphere reaches a steady state very quickly. Both the heat transfer coefficient and the steady temperature distribution in the boundary layer are essential to the calculations in the mathematical model which is presented in Chapter V.

Heat transfer experiments involving spinning were conducted in the following manner. The thermocouple was positioned at the center of the 3 cm. nickel sphere, which was attached to the iron tube. Then the iron tube was mounted in the pillow block bearings shown in Figure III-4, and the slip rings and brushes were connected. After the liquid slag in the crucible shown in Figure III-2 remained at temperature, the temperature was measured with an optical pyrometer. The slag was stirred by hand with an iron rod to improve the uniformity of the temperature of the slag. Using the controlled DC motor, the spinning velocity (revolutions per minute) of the sphere and tube assembly was set at a particular value as noted in Table III-2. This velocity was measured with a stroboscopic tachometer before immersing the sphere into the slag. After starting the millivolt recorder, the spinning metal sphere was immersed into the liquid slag by manually lowering the transite carriage along two vertical metal tracks located just above the furnace. The carriage was quickly lowered until the center of the sphere was 7 cm. beneath the surface of the liquid slag. The spinning

velocity was again measured with the tachometer, and the temperature of the liquid was measured with an optical pyrometer, which was sighted on the surface of the slag. The metal sphere remained immersed in the liquid slag until the temperature recorded by the thermocouple at the center of the sphere indicated no further change. At this time, the electric motor was shut off, and the sphere and assembly were removed from the furnace.

Usually the sphere and assembly could be reused, after the iron tube was checked for straightness, and the metal sphere was cleaned off and allowed to cool to room temperature. Often the tube could be straightened, if it became bent. Some metal spheres were used for as many as eight separate experiments.

The errors which are inherent in this experiment are discussed in Appendices A, B and C.

III.B.2. Forced Convection by Bubble Stirring

The purposes of conducting heat transfer experiments in silicate slags stirred by rising bubbles were to test another form of convection in the slag, and to simulate practical mixing conditions in an electric furnace steelmaking operation. Bubbling was a good alternative method of convection because it was less severe than spinning, yet direct enough for estimating heat transfer coefficients in the liquid. Also, bubbling is the predominant means by which the slag is stirred during electric furnace steelmaking operations.

The procedure for the experiments which used stirring by rising bubbles was similar to that for the experiments which used the spinning sphere. A horizontal iron tube provided the flow of gas bubbles in the experiment as shown in Figure III-6. This iron tube was 5 cm. long and 1.2 cm. in diameter with 24 1 mm. orifices on the upper one fourth of its surface. Nitrogen gas flowed into this bubbling tube from another 1.2 cm. iron tube, rising vertically through the top of the crucible shown in Figure VII-6. The flow of nitrogen was measured by a mercury manometer and a capillary flowmeter. As shown in Table III-3 the range of flow rates was 0 to 410 cm^3/sec. Only slags N-1CU and N-2CU were used in these experiments.

After the slag was completely melted inside the iron crucible, the bubbling tube was lowered through the hole in the top of the lid, immersed into the liquid slag, and set at the bottom of the crucible. Gas flowed through the orifices of the bubbling tube until the temperature of the slag and the tubing reached a steady state. Once this steady state was achieved at a set gas flow rate, the nickel sphere (not spinning) was quickly immersed into the liquid slag and fixed in position immediately above the column of rising bubbles. The temperature at the center of the sphere was recorded as a function of time after immersion until the temperature reached a steady value. All other procedures were identical to those with the sphere spinning, Section III.B.1.

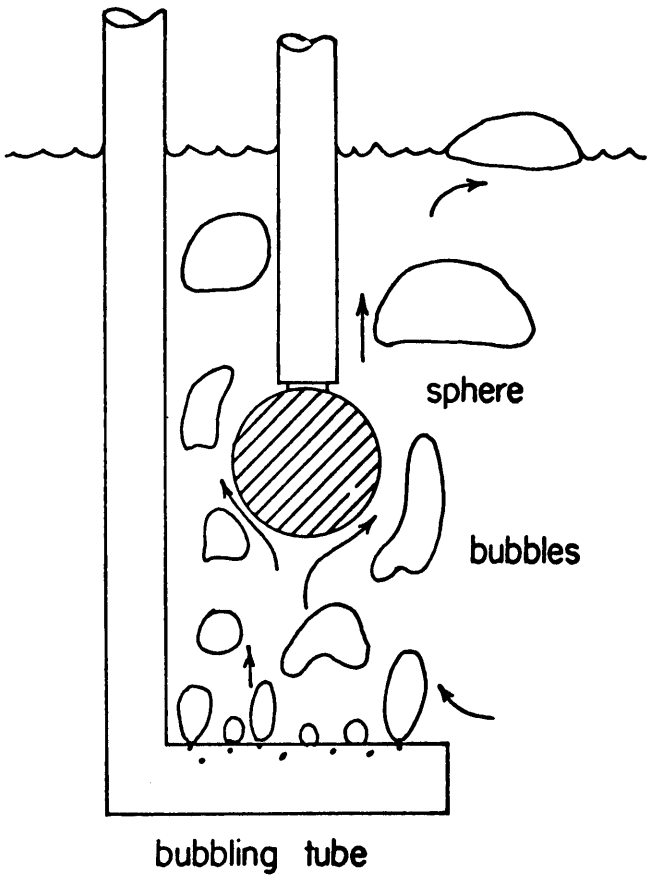

Figure III-6 Bubbling tube arrangement

III.B.3. Experiments with Various Slag Compositions

Several different types of slags were studied under the conditions outlined in Table III-2. The chemical compositions and descriptions of these slags are given in Table III-1. For the ferrous silicate slags, N-1W, N-FA, N-2W, N-FB, and N-FC, the locations of the compositions are shown in the polythermal projection of the liquidus of the $FeO-Fe_2O_3-SiO_2$ system in Figure III-7. The measured and estimated properties of some of these slags are shown in Table III-4 and III-5. The sources of these values are discussed in detail in Section V.E.

III.B.4. Experiments with Various Metal Objects

The purpose of using various metal objects in these heat transfer experiments was to assess the effects of 1) the initial temperature of the metal object, 2) the size of the metal object, 3) the shape of the object, 4) the thermal conductivity of the metal, and 5) the melting of the object.

The initial temperature of the spinning nickel sphere was varied by preheating the sphere above the furnace before immersing it into the liquid slag. The initial temperature of the sphere in Table III-2 was obtained by heating the nickel sphere 10 to 20 degrees above the predetermined initial temperature and then placing it inside a refractory shield to cool uniformly. Once the initial temperature was obtained, the spinning sphere was immersed into the slag and the normal experimental procedures were followed.

Table III-4. Thermal Properties of Liquid Slags at Iron Saturation*

	Symbol	Slag Designation							
		N-FA	N-FB	N-FC	N-1A	N-2A	N-CA	N-1CU	N-IR
Specific heat, cal/g °C	C_L	0.28	0.28	0.28	0.28	0.28	0.28	0.28	0.28
Density, g/cm^3	ρ_L	3.8	3.7	3.6	3.5	3.5	3.5	3.5	2.9
Thermal diffusivity ($cm^2/sec \times 10^4$)	α_L	47.	40.	52.	32.	32.	53.	47.	40.
Thermal conductivity, cal/sec-cm-°C x 10^4	K_L	48.	41.	52.	31.	31.	53.	47.	32
Viscosity, poise	μ	1.5	2.	2.	2.	2.	2.	2.	5.
Linear coefficient of thermal expansion, /°C x 10^6	β	50	50.	50.	50.	50.	50.	50.	50.

*See Section V.E.1 for complete references

Table III-5. Thermal Properties of Solid Slags*

	Symbol	N-FA	N-FB	N-FC	N-1A	N-2A	N-CA	N-1CU
Specific heat, cal/g-°C	C_S	0.24	0.25	0.25	0.25	0.25	0.25	0.25
Density, g/cm^3	ρ_S	4.3	4.2	3.7	3.8	3.8	3.9	3.8
Thermal diffusivity, cm^2/sec x 10^4	α_S	51.	47.	64.	37.	37.	48.	45.
Thermal conductity, cal/sec-cm-°C x 10^4	K_S	52.	44.	59.	35.	35.	47.	43.
Solidus temperature, °C**	T_S	1152.	1170.	1150.	1070.	1070.	1060.	1125.
Heat of fusion, cal/g	ΔH	110.	115.	80.	80.	80.	80.	80.

*See Section V.E.2 for complete references

**See Section IV.B.

The following metal objects were studied in the heat transfer experiments: 1) nickel and copper spheres of 3.06 cm. diameter, 2) nickel spheres of 1.8 cm. diameter, and 3) a nickel cylinder of 1.5 cm. diameter and 8.8 cm. length. The conditions for these experiments are shown in Table III-2. In the case of the copper sphere, the copper melted was allowed to fall to the bottom of the crucible.

Some heat transfer experiments were conducted with porous iron spheres as described in Section III.A.2. These experiments simulated the heat transfer to low thermal conductivity porous iron pellets used in electric furnace operations. The experimental conditions are shown in Table III-2. Procedures were identical to those used for a spinning sphere.

III.C. Differential Thermal Analysis of Slags

The melting temperature for the solidified slag shell was determined by differential thermal analysis. A 20 mg. sample of powdered slag was placed inside an iron crucible (1.4 mm. inside diameter) as shown in Figure III-8. A 20 mg. reference of Baker reagent grade alumina was placed in an identical iron crucible. Positioned in a K-28 firebrick which was surrounded by a graphite susceptor, these crucibles were heated to a temperature 50°C below the suspected solidus. Then the heating rate was adjusted to 10 degrees per minute and the temperature was raised through the melting temperature of the slag. During the melting, a platinum/platinum-10% rhodium thermocouple which was in direct contact with the powdered slag recorded the temperature of the

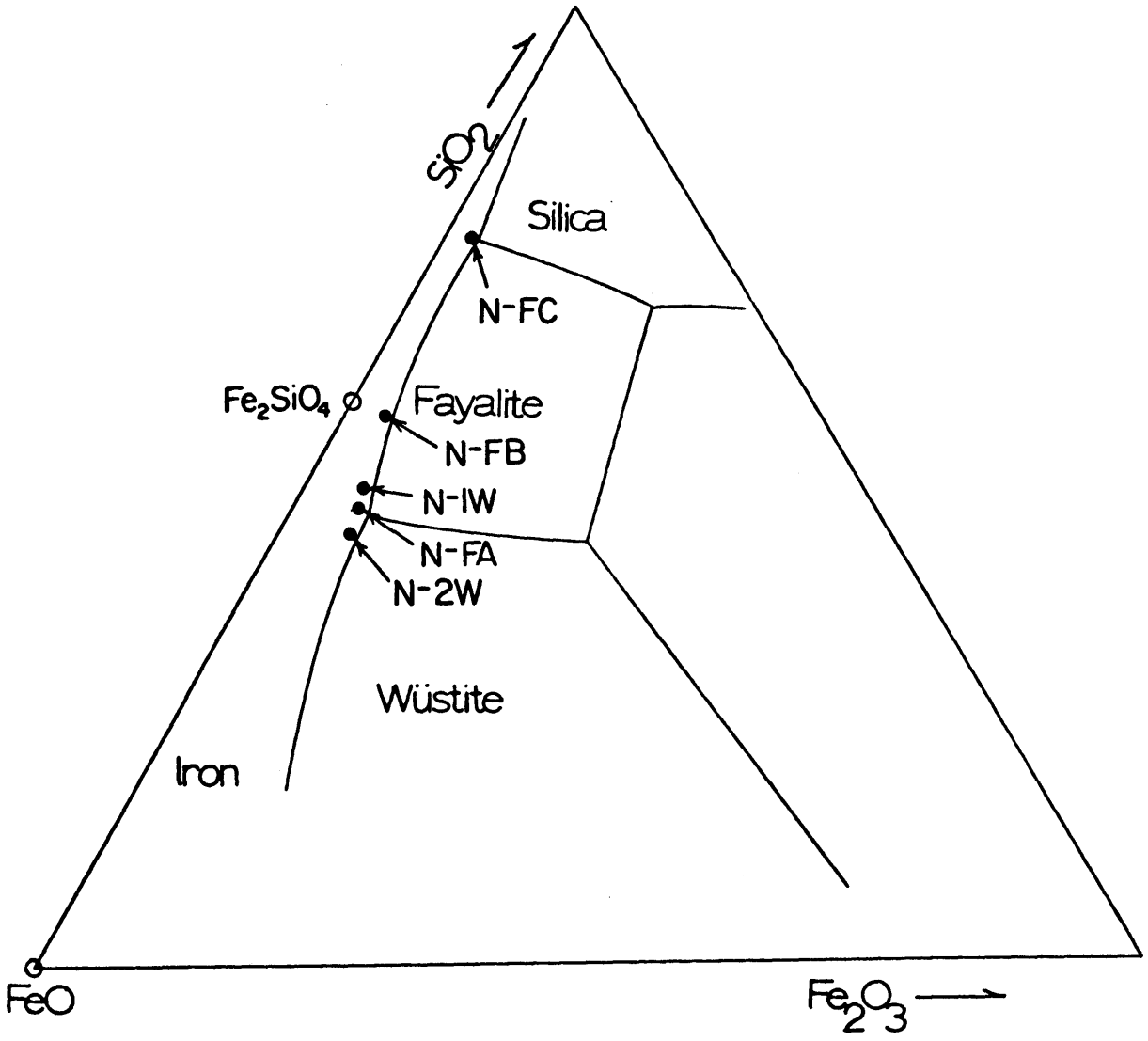

Figure III-7 $FeO-SiO_2-Fe_2O_3$ phase diagram for ferrous silicate slags (72)

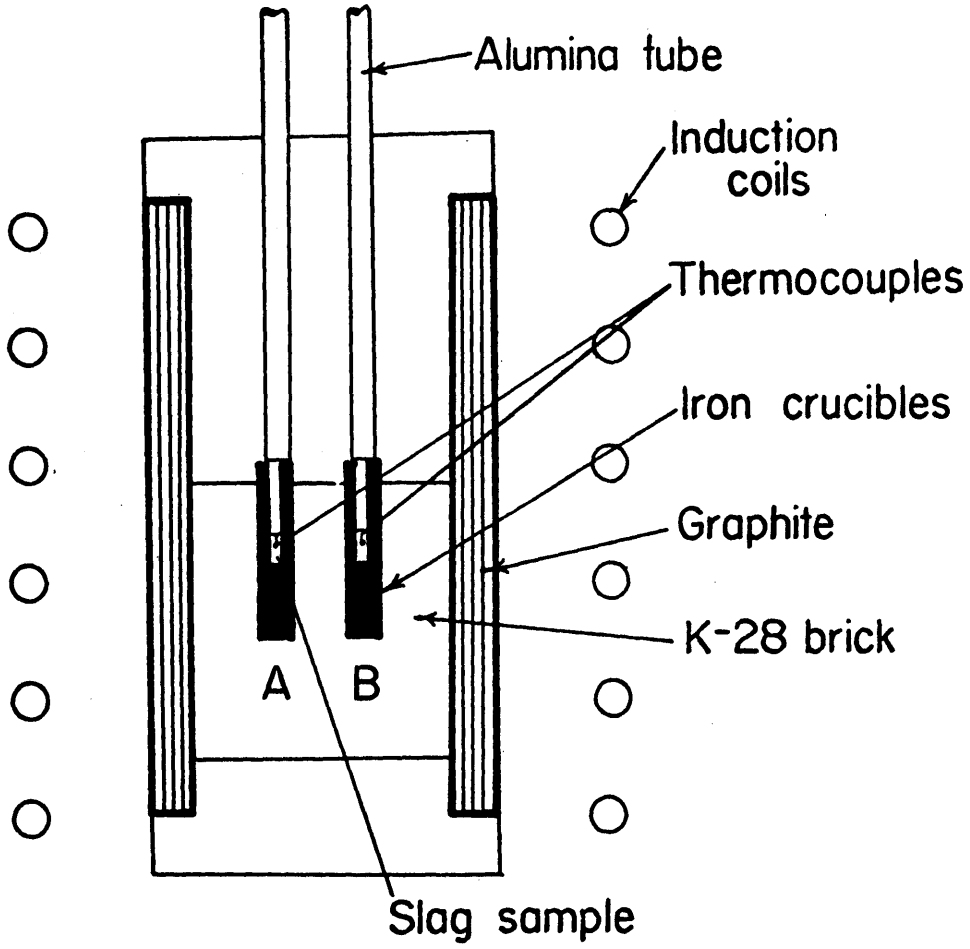

Figure III-8 Differential thermal analysis apparatus

slag. The temperature of the slag was plotted against the temperature difference between the slag and the alumina to indicate the presence of phase changes.

This differential thermal analysis technique was tested with samples of KCl. Cooling as well as heating DTA curves were recorded with some of the samples of slag to test the measurement of the melting range. The slag samples for the analysis were obtained from the solid slag shell formed on the nickel sphere after 30 seconds of immersion in the particular liquid slag.

IV. EXPERIMENTAL RESULTS

IV.A. Heat Transfer Experiments in Liquid Slags

Selected experimental results for the heat transfer experiments described in Chapter III are presented under the titles of the following experimental conditions: 1) Spinning and national convection, 2) bubble stirring, 3) variations in slag composition, 4) liquid slag temperatures, and 5) variations in initial temperature, size, shape, and composition of the metal object.

IV.A.1. Spinning and Natural Convection

The difference between heating a nickel sphere which is in spinning convection or only natural convection is shown in Figure IV-1. The temperature recorded by the thermocouple at the center of the sphere is plotted as a function of the time of immersion for a 3 cm. nickel sphere in slag N-IR. The lower heating curve results from the heat transfer to the sphere with no spinning; thus, only natural convection is present. The upper curve results from heat transfer to the sphere spinning at 550 rmp. During the initial 30 seconds of the experiments, a delay in the response of the thermocouple is observed. This delay is especially pronounced because the thermocouple is surrounded by an alumina tube as described in Chapter III. The delay in the thermocouple response is discussed in detail in Appendix A.

The effect of the spinning rate on the temperature at the center of the sphere immersed in slag N-IR at 1320°C is shown in Figure IV-2.

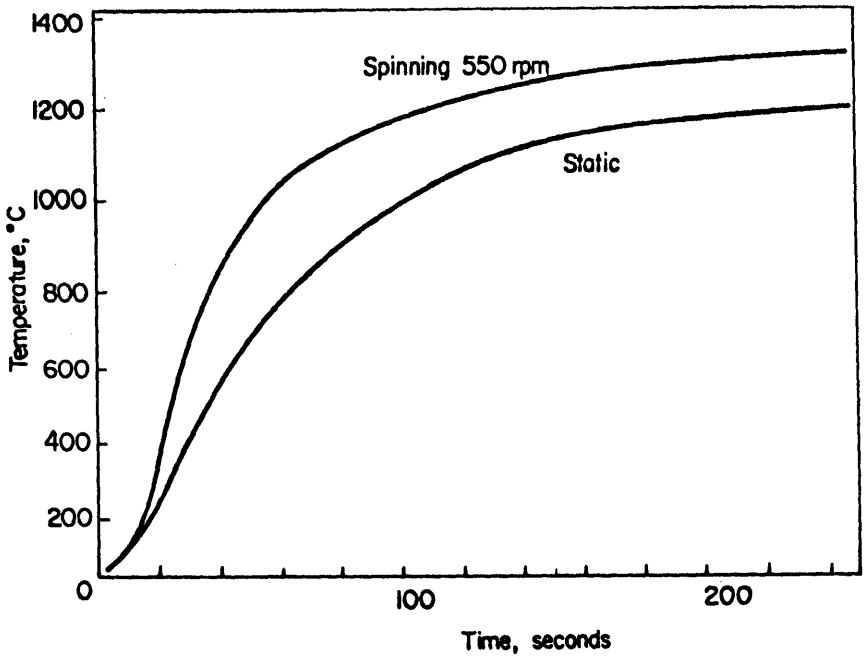

Figure IV-1 Comparison of heating curves of a spinning and a static sphere. Conditions: 3 cm. nickel sphere; slag N-IR, and bath temperature 1350°C

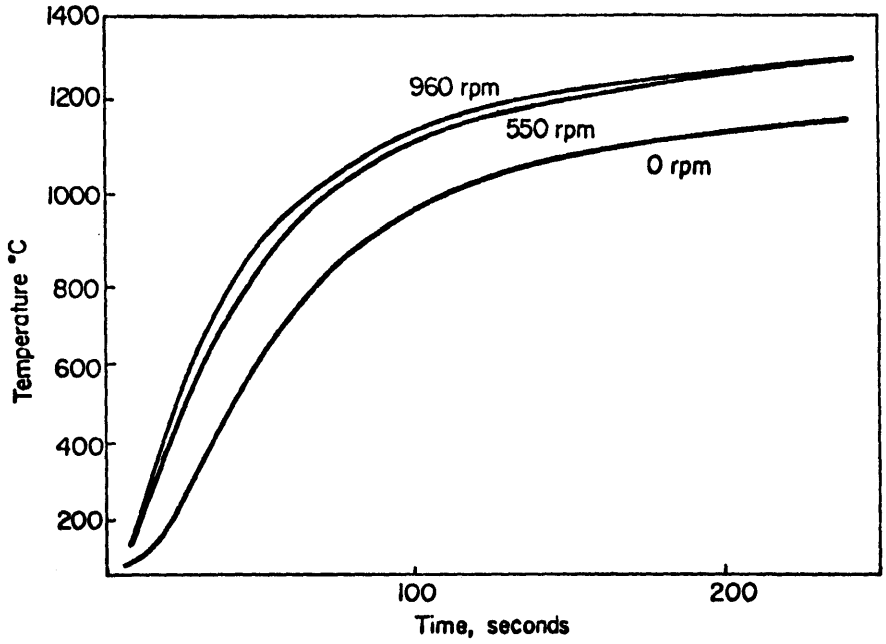

Figure IV-2 Comparison of heating curves of a sphere at various spinning rates. Conditions: 3 cm. nickel sphere; slag N-IR; and bath temperature 1320°C

Spinning rates of 960 rpm. and 550 rpm. are shown. Similarly, the effect of spinning is shown for a 1.83 cm. nickel sphere in slag N-FB. in Figure IV-3. An abrupt increase in the temperature is shown in the final stage of the heating curve. This increase indicates that the insulating slag shell is finally removed.

The effects of spinning are shown even more dramatically in Figure IV-4. In curve 1, the temperature of a 3.06 cm. nickel sphere spinning at 700 rpm. is shown. In curve 2 the sphere spins initially at 300 rpm. for 45 seconds. At that time the spinning is stopped and the sphere remains static; after 270 seconds it is spun again at 300 rpm. In curve 3 the sphere is initially static for 250 seconds, then it is spun at 300 rpm.

IV.A.2. Bubble Stirring

Observations were made of the bubbling apparatus in a clear glycerol 10% water solution. The similarities between the bubbling in the glycerol solution and in the liquid slag were the orifice diameter, the volumetric orifice flow rate (at the liquid temperature), and the viscosity of the liquid. Similarity criteria for the glycerol and slag systems are discussed briefly in Appendix G.

In the glycerol solution the gas bubbles leaving the orifices coalesced into large spherical cap bubbles of 1 to 3 cm. diameter. The mean bubble radii shown in Table IV-1 were estimated from photographs taken during the bubble stirring. At a gas flow rates less than 100 ml/sec., the bubbles rose preferentially to one side of the sphere.

Table IV-1. Approximate Bubble Sizes in Glycerin 10% Water

Flow rate (cm^3/sec)	Mean bubble diameter (cm)	Range of bubble diameter (cm)
50	0.2	0.1 - 3.0
100	0.4	0.01 - 3.0
200	0.5	0.01 - 4.0
300	0.5	0.01-4.0

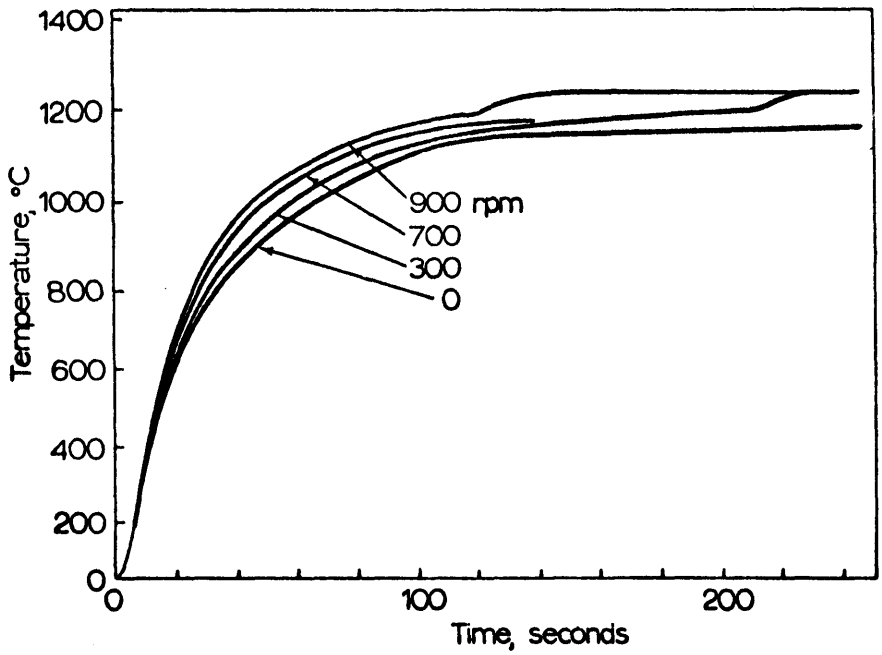

Figure IV-3 Comparison of heating curves of a small sphere at various spinning rates. Conditions: 1.8 cm. nickel sphere; slag N-FB; and bath temperature 1250°C

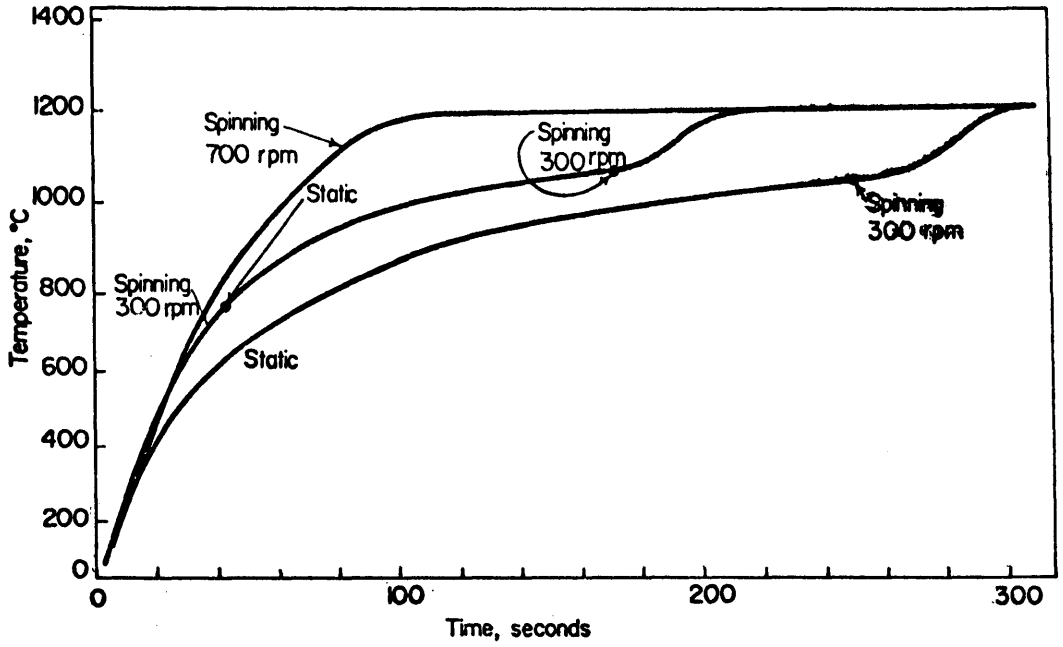

Figure IV-4 Comparison of heating curves of a sphere at various spinning and static conditions. Conditions: 3 cm. nickel sphere; slag N-1CU; and bath temperature 1200°C

The cross section of the bubble column at all flow rates was about 50 cm^2.

The effects of bubble mixing on the heating of the nickel sphere immersed in the liquid slag are shown in Figure IV-5 at various gas flow rates. Also the heating curves for the spinning sphere and the static sphere with no gas bubbling are shown. All of these heating curves were obtained with a 3 cm. nickel sphere in slag N-1CU at a bath temperature of 1200°C, and only the manner or degree of convection was different. With the gas flow rate of 40 ml/sec. the heating curve was not substantially different from the curve obtained with a static sphere and no bubbling. At a flow rate of 410 ml/sec. the heating curve was nearly identical to the curve obtained with the spinning sphere.

Samples of the solidified slag shell were obtained by removing the metal sphere after 50 seconds of immersion in the bubbling slag. When the gas flow rate exceeded 250 ml/sec., the pores in these samples constituted about 10 to 15 volume percent and ranged in diameter from a few microns to 1 mm. Along the bottom of the nickel sphere, the shell thickness was 50 to 70% thinner than on the sides of the sphere. At the lower gas flow rate the shell was dense and uniform in thickness.

IV.A.3. Variations in Slag Composition

Comparison of the heating curves for spinning nickel spheres in various liquid slag compositions is shown in Figures IV-6, IV-7, and IV-8. The shapes of these heating curves range from the smooth logarith-

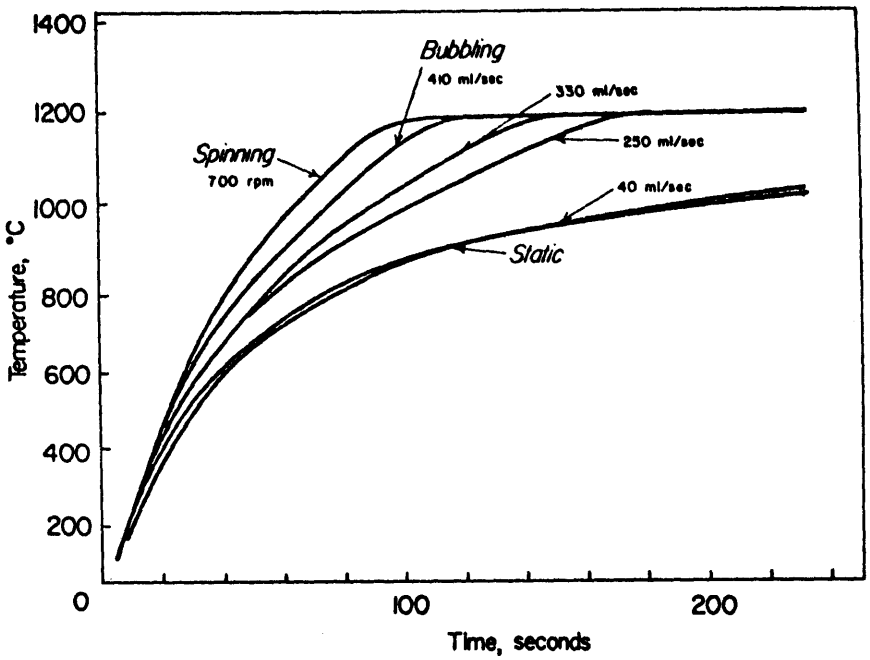

Figure IV-5 Comparison of heating curves of a sphere under various types of convection. Conditions: 3 cm. nickel sphere; slag N-1CU; and bath temperature 1200°C

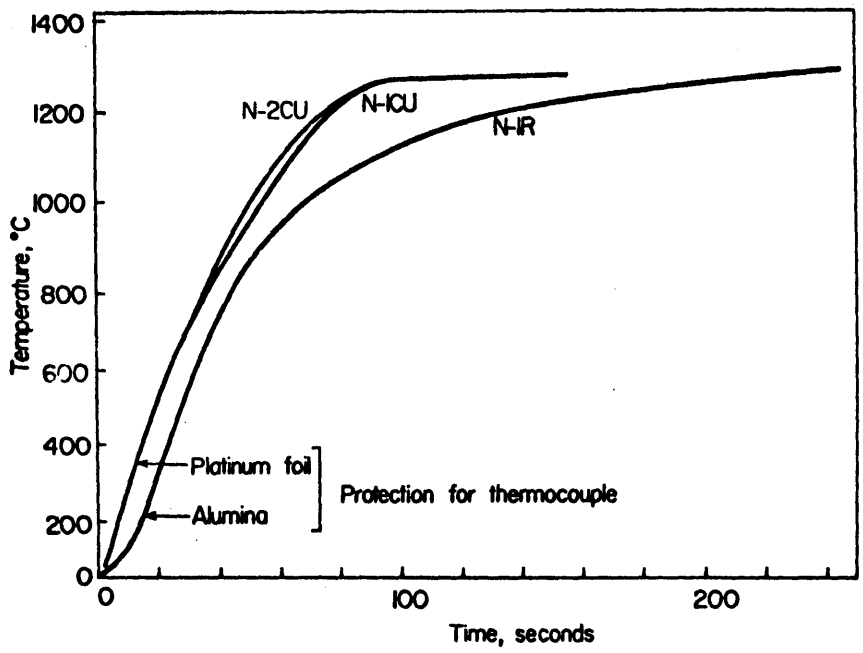

Figure IV-6 Comparison of heating curves of a sphere in slags N-IR, N-1CU and N-2CU. Conditions: 3 cm. nickel sphere; spinning at 700 rpm; and bath temperature 1300°C

mic heating curve, as in slag N-CA, to an irregular curve, as in slag N-FA. These irregularities in the heating curves give an indication of the growth and shrinkage of the solid slag shell on the sphere, which will be discussed in Chapter VI.

The heating curves for synthetic steelmaking and copper smelting slags are shown in Figure IV-6. The curves for both N-1CU and N-2CU are nearly identical. The difference between the initial portion of the heating curves for slags N-1CU and N-IR is caused by the difference in the protection of the thermocouple. In the experiments with slag N-1CU, platinum foil was used to protect the thermocouple from contamination and improve contact with the sphere. In experiments with slag N-IR a 1 mm. thick alumina protection tube was used to protect the thermocouple. The copper smelting slags are better heat transfer media than the steelmaking slag, because the heating of the 3 cm. nickel sphere was faster in the copper slags.

The effect of EeO in the liquid slag on the heating curves for a spinning nickel sphere is shown in Figure IV-7. As the concentration of FeO in the liquid slag increases, the heating time decreases. The compositions, descriptions, and thermal properties of these ferrous silicates are given in Table III-1, III-4 and III-5, respectively.

During the heat transfer experiments with these ferrous silicates, the surface of the solidified slag shell ranged from smooth and hard to rough and mushy. The surfaces of all the silicates except N-1W and N-FB are smooth and hard, as shown in Figure IV-9. For slags N-1W

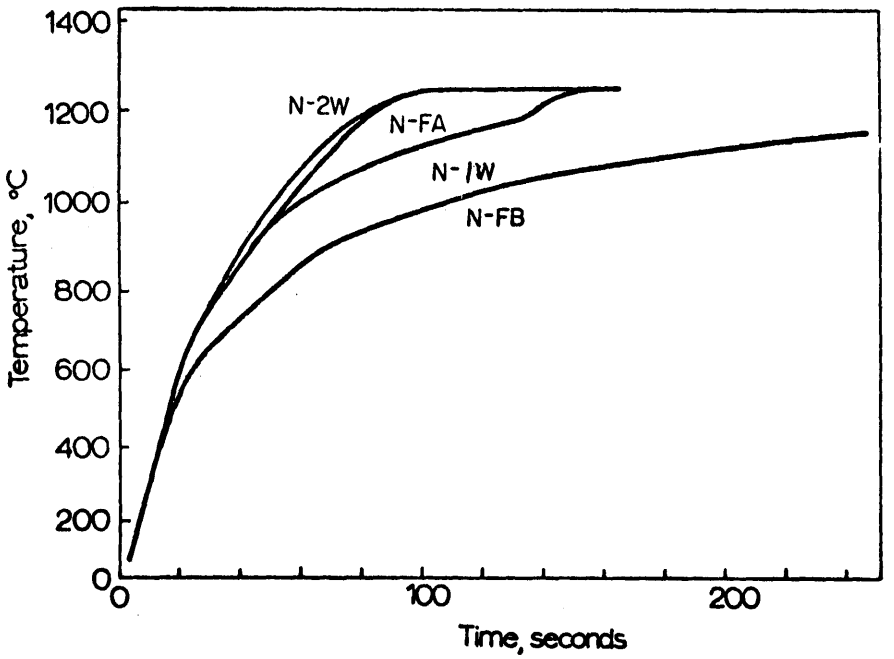

Figure IV-7 Comparison of heating curves of a sphere in slags N-2W, N-FA, N-1W, and N-FB. Conditions: 3 cm. nickel sphere; spinning at 700 rpm; and bath temperature 1250°C

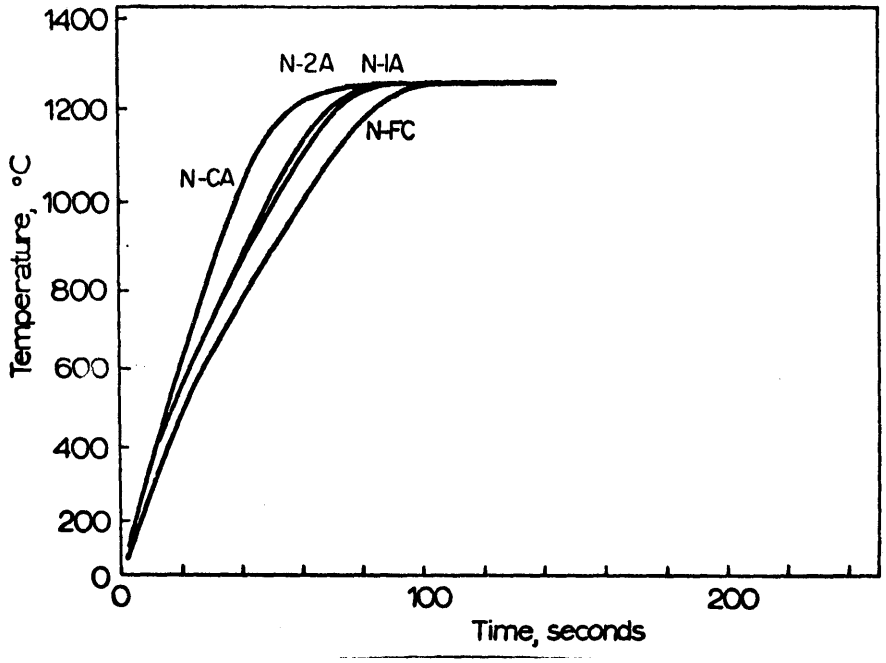

Figure IV-8 Comparison of the heating curves of a sphere in sphere in slags N-FC, N-1A, N-2A, and N-CA. Conditions: 3 cm. nickel sphere; spinning at 700 rpm; and bath temperature 1250°C

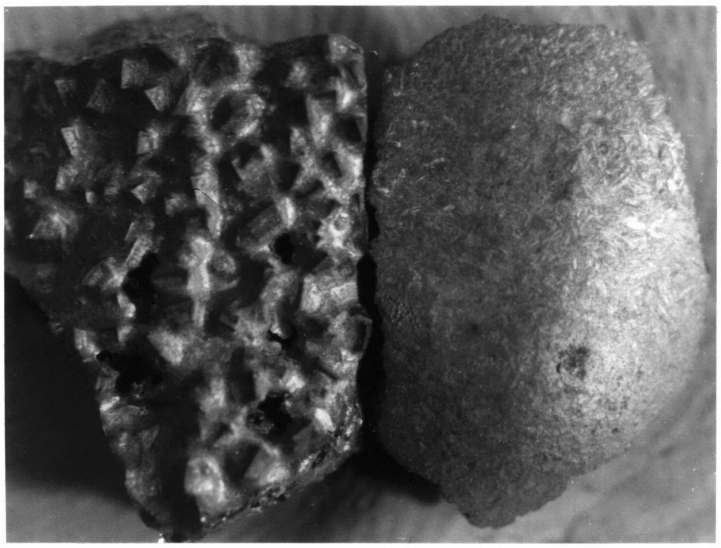

N-FB N-FA

Figure IV-9 Surface structure of slags N-FB and N-FA from the solid slag shell (5x)

and N-FB the slag shell is covered with large faceted crystals of fayalite, visibly protruding 0.7 mm. from the surface, as shown in Figure IV-9. The slag shell from slags N-1W and N-FB is also very soft or mushy upon immediate removal from the furnace.

The effect of additions of CaO and Al_2O_3 to slag N-FC is shown in Figure IV-8. In both cases, the oxide additions decrease the heating time for the spinning sphere. The microstructures of the solidified slag shell are substantially modified by these additions as shown in Figures IV-10 and IV-11. More solid phases are present and the crystals are better oriented in the direction of heat flow.

IV.A.4. Variations in Liquid Slag Temperatures

The comparisons of the heating curves obtained in several of the liquid slags are shown in Figures IV-12, 13, 14, 15,16 and 17. In all of these silicate slags, the slope of the heating curve increases with increasing temperature of the liquid. This increase in slope is minor in slag N-IR in Figures IV-12 and IV-13, but it is substantial in slag N-2A as shown in Figure IV-17.

IV.A.5. Variations in the Initial Temperature, Size, Shape, and Composition of the Metal Object

The effect of the initial temperature of the spinning nickel sphere on the temperature of the sphere immersed in various liquid slags is shown in Figures IV-18, IV-19, IV-20. In all cases, preheating the sphere decreased the heating time of the sphere in the slag, but it had little effect upon the slopes of the heating curves.

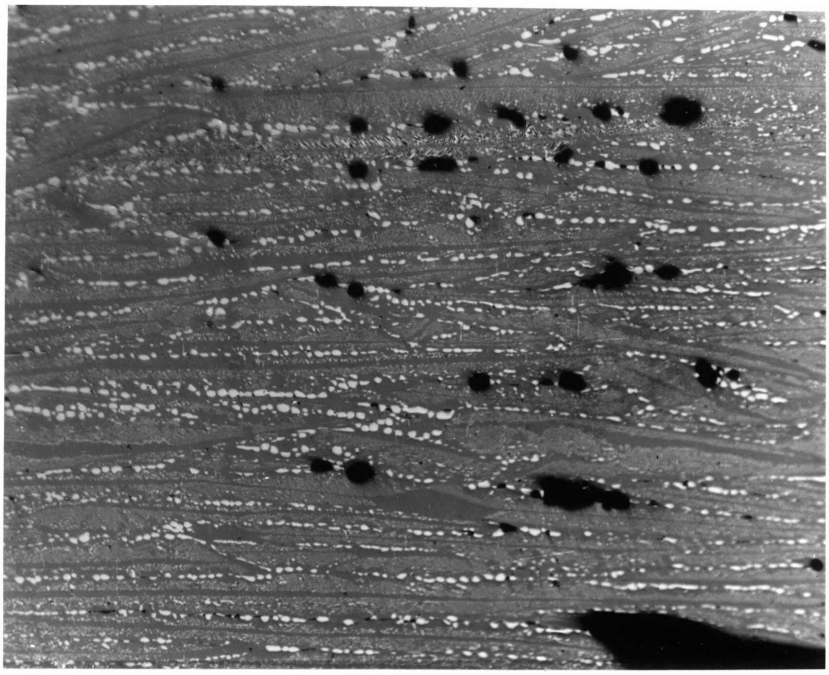

N-FA (Heat flow →)

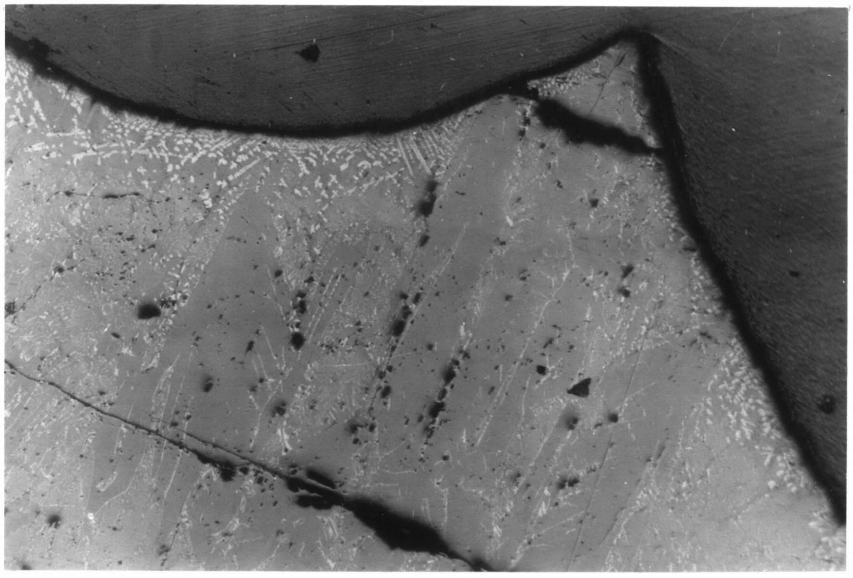

N-FB (Heat flow ↑)

Figure IV-10 Microstructure of slag shell for slags N-FA and N-FB (125x)

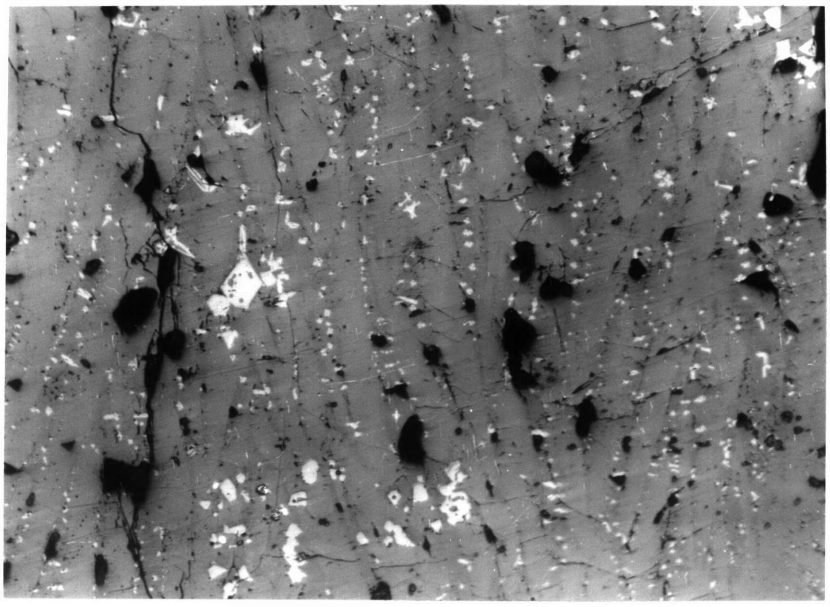

N-CA

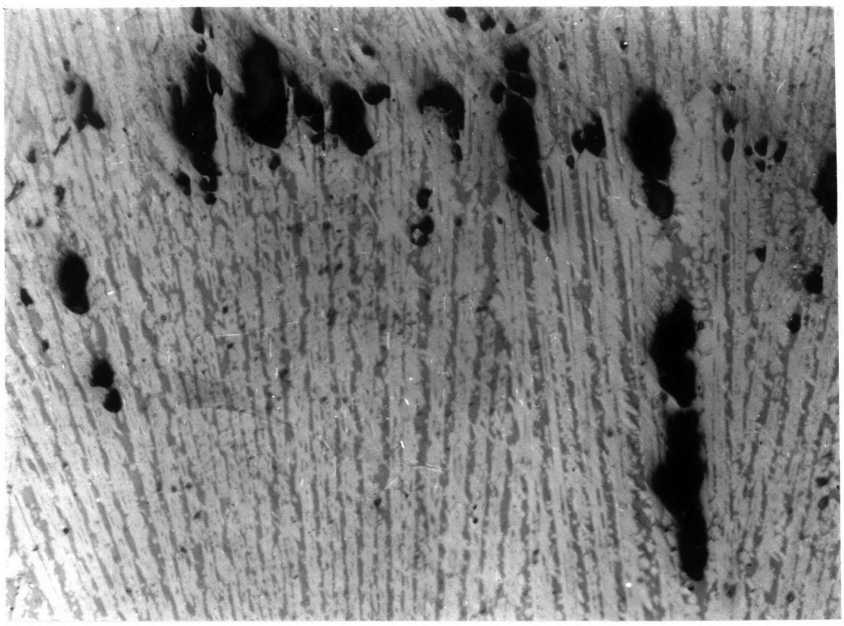

N-2A

Figure IV-11 Microstructure of slag shell for slags N-CA and N-2A (125x) Heat flow ↑

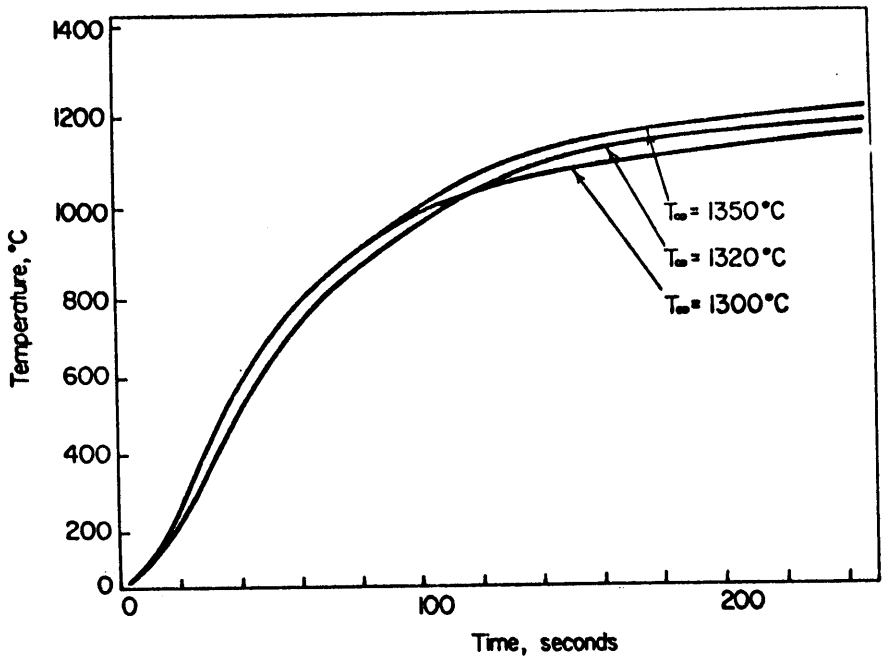

Figure IV-12 Comparison of the heating curves of a static sphere at various bath temperatures. Conditions: 3 cm. nickel sphere; and slag N-IR

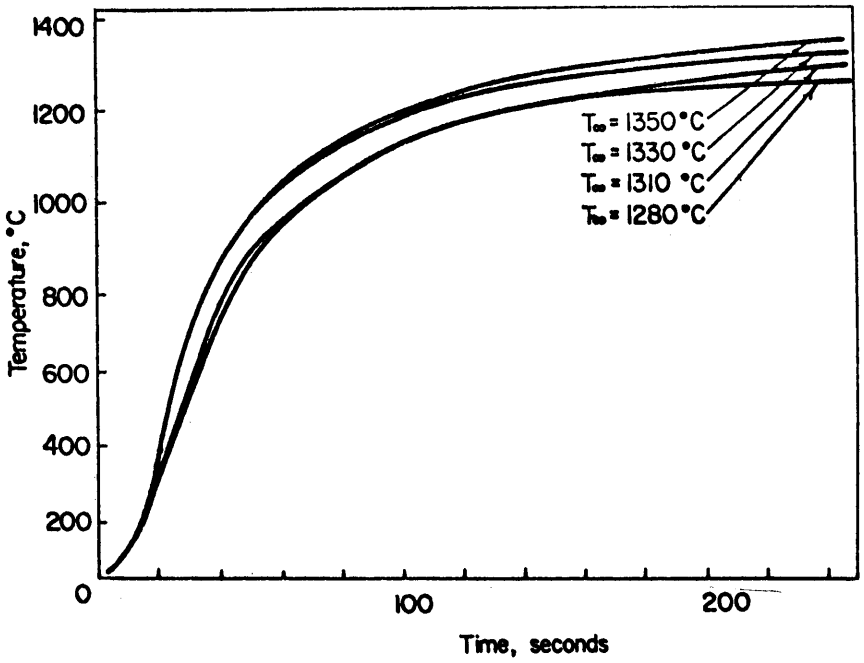

Figure IV-13 Comparison of the heating curves of a spinning sphere at various bath temperatures. Conditions: 3cm. nickel sphere; spinning at 700 rpm; and slag N-IR

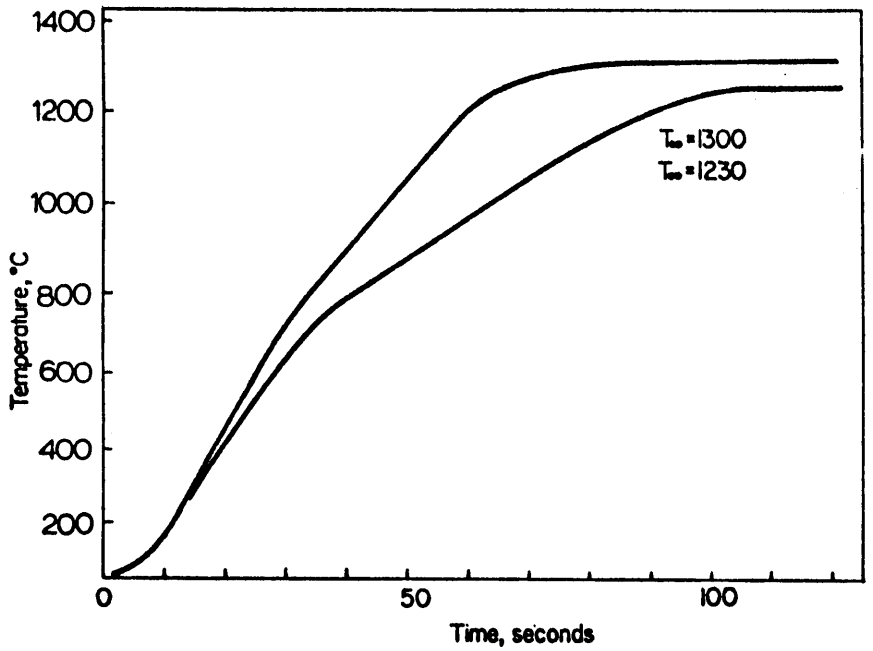

Figure IV-14 Comparison of the heating curves of a spinning sphere at various bath temperatures. Conditions: 3cm. nickel sphere; spinning at 700 rpm; and slag N-FA

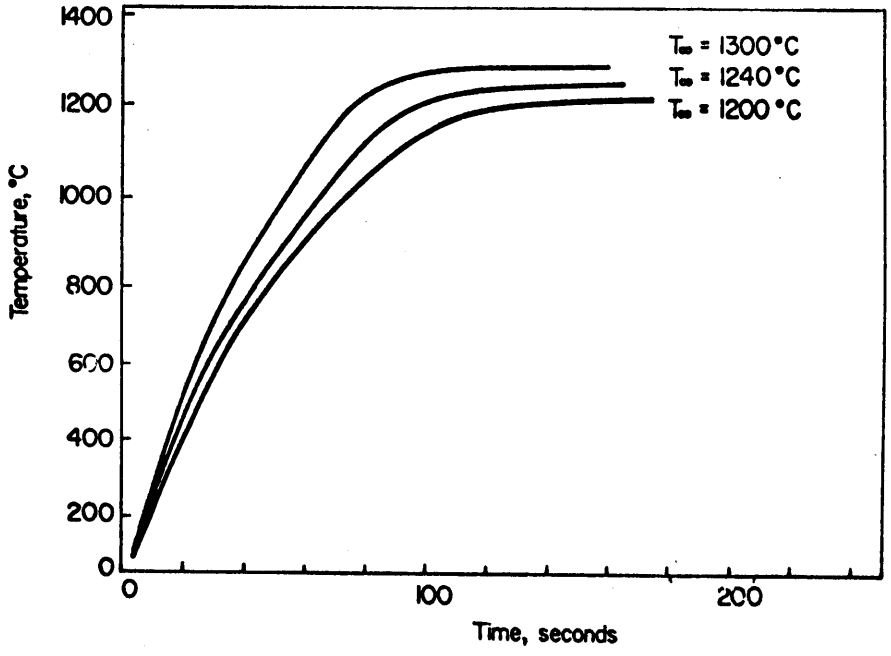

Figure IV-15 Comparison of the heating curves of a spinning sphere at various bath temperatures. Conditions: 3cm. nickel sphere; spinning at 700 rpm; and slag N-1CU

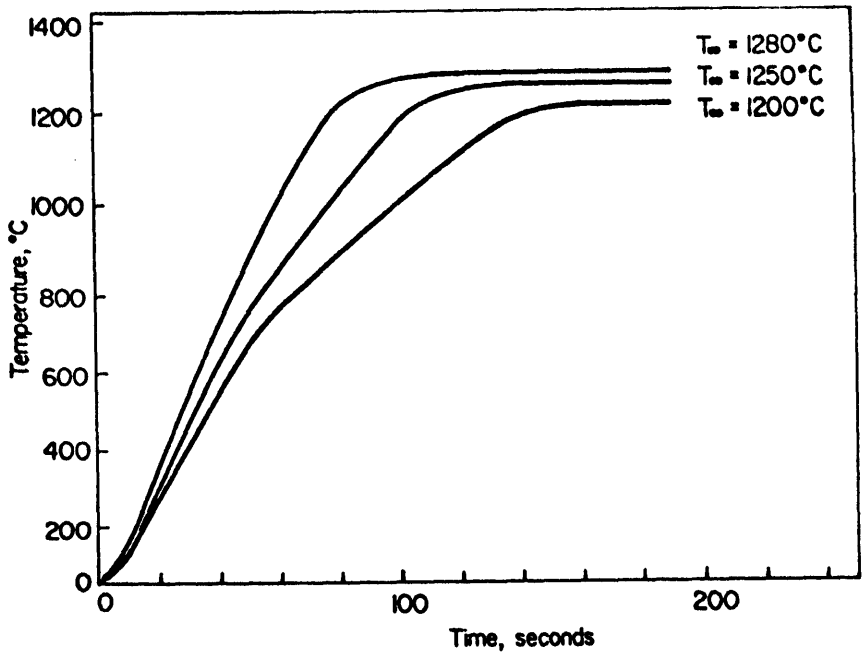

Figure IV-16 Comparison of the heating curves of a spinning sphere at various bath temperatures. Conditions: 3 cm. nickel sphere; spinning at 700 rpm; and slag N-FC

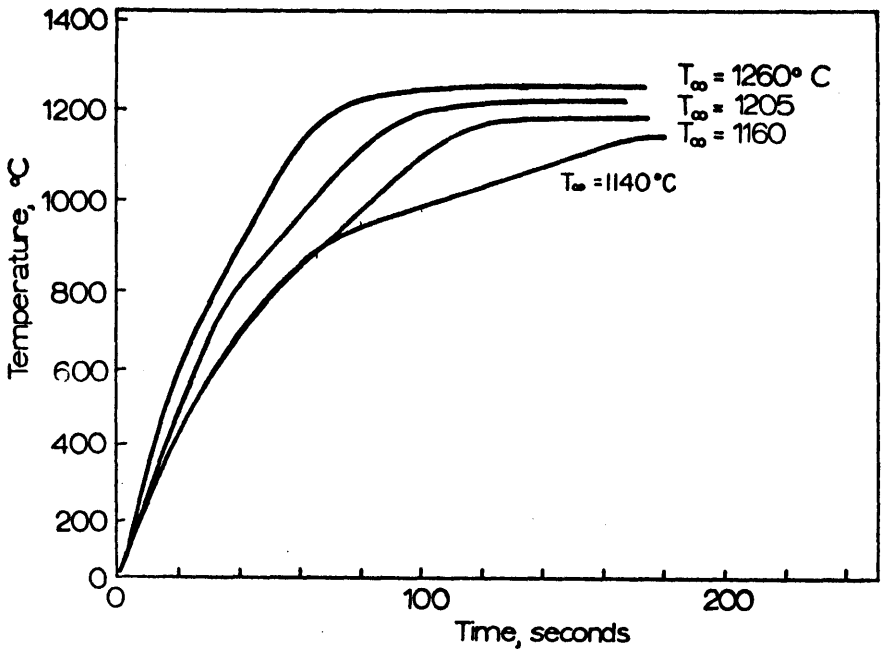

Figure IV-17 Comparison of the heating curves of a spinning sphere at various bath temperatures. Conditions: 3 cm. nickel sphere; spinning at 700 rpm; and slag N-2A

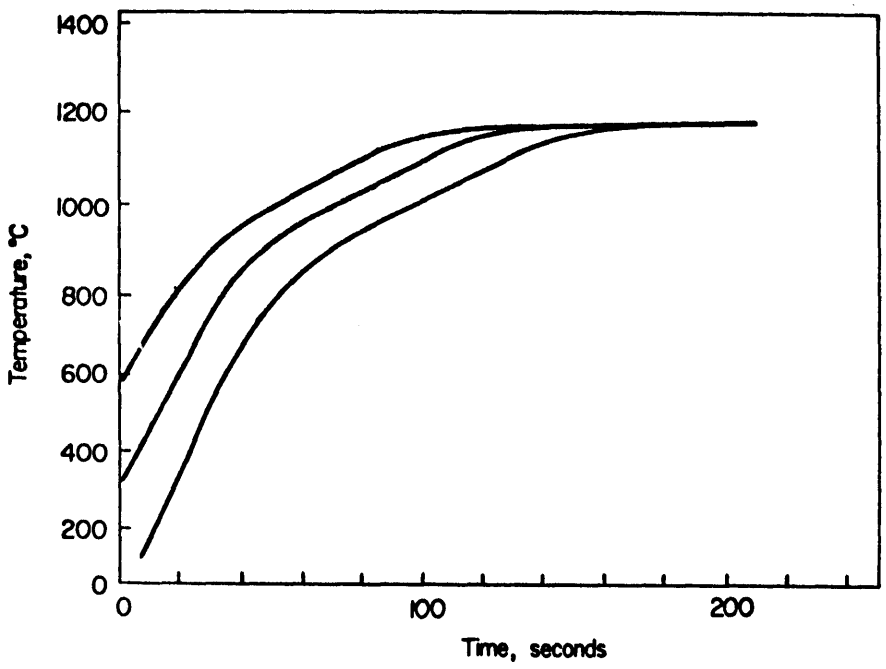

Figure IV-18 Comparison of the heating curfes of a sphere at various initial temperatures. Conditions: 3 cm. nickel sphere; spinning at 700 rpm; bath temperature 1180°C; and slag N-1CU.

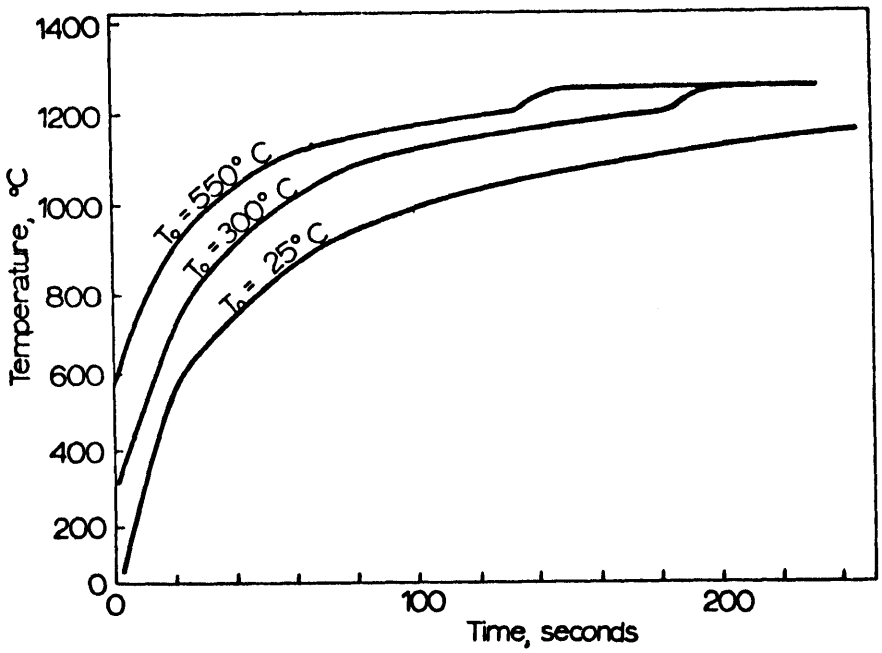

Figure IV-19 Comparison of the heating curves of a sphere at various initial temperatures. Conditions: 3 cm. nickel sphere; spinning at 700 rpm; bath temperature 1250°C; and slag N-FB

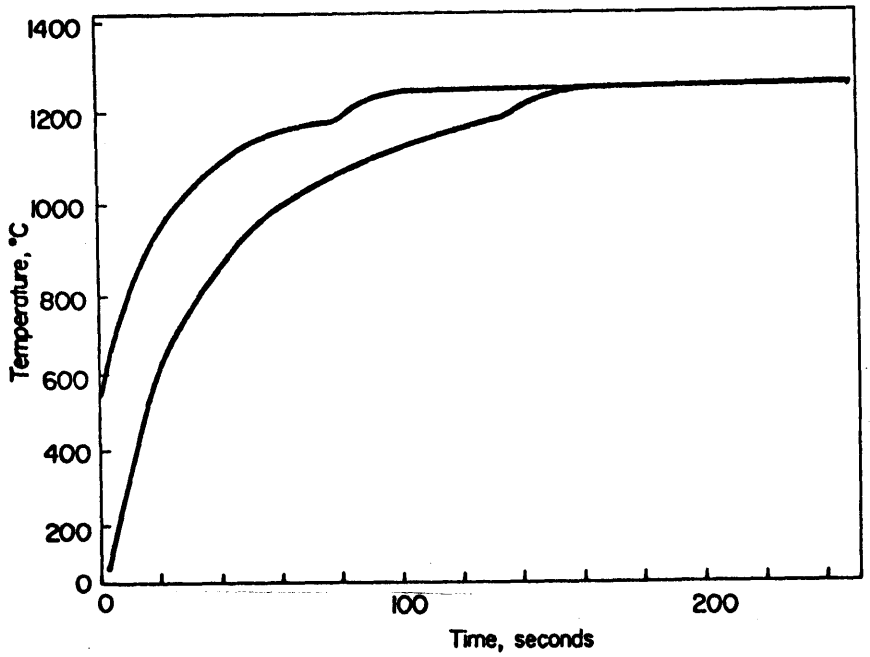

Figure IV-20 Comparison of the heating curves of a sphere at various initial temperatures. Conditions: 3 cm. nickel sphere; spinning at 700 rpm; bath temperature 1250°C, and slag N-1W

The temperature of both 1.8 cm. diameter nickel sphere and the 1.5 cm. diameter nickel cylinder increased more rapidly than that of the 3.0 cm. diameter nickel sphere, as shown in Figures IV-21 and IV-22.

Under identical slag conditions, the heating times for the 1.8 cm. diameter nickel sphere and the 1.5 cm. nickel cylinder were less than that for the 3.0 cm. nickel sphere, as shown in Figure IV-20 and IV-21.

The heating curves in Figure IV-23 for porous iron spheres differ markedly from that of the 3.0 cm. nickel sphere. The temperature at the center of the 50 mesh porous iron sphere increases at nearly the identical rate as that of the nickel sphere, but it is offset by about 10 to 20 seconds. However, the temperature of the 100 mesh porous iron sphere not only is offset considerably from that of the nickel sphere, but the temperature increases at a lower rate as well.

It was observed that, if the iron supporting tube was sealed, the porous spheres evolved a considerable amount of gas into the liquid slag.

The heating curves for copper spheres in Figure IV-24 show the heating and melting of the copper in the liquid slag. Since the melting point of copper is lower than the melting point of any of the silicate slags studied, the solid slag shell provided a means of support while the copper was melting. This means of support was maintained throughout the melting for the static copper sphere, but it was insufficient support for the spinning sphere, as shown in Figure IV-24.

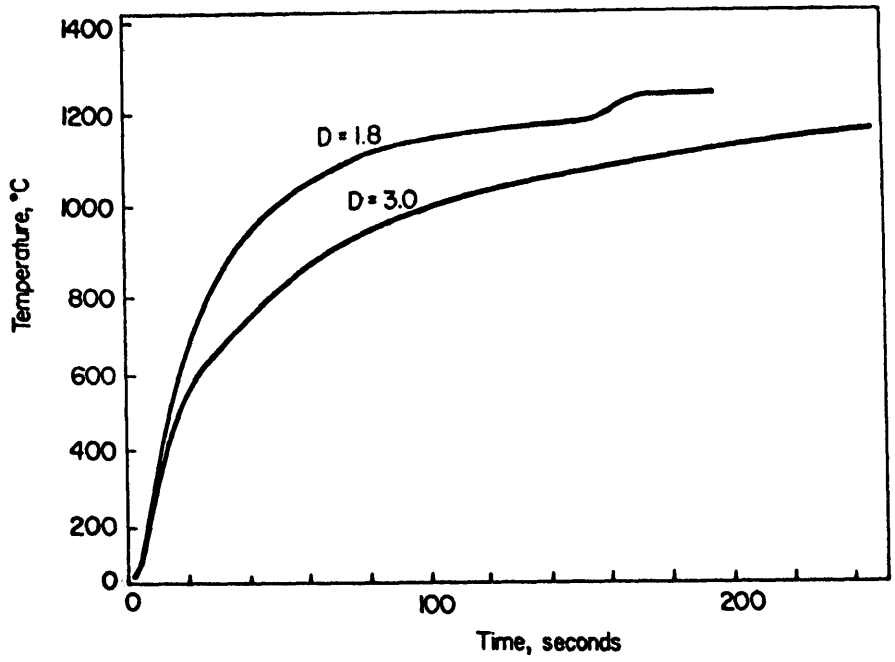

Figure IV-21 Comparison of the heating curves of a 3 cm sphere and a 1.8 cm. sphere. Conditions: spinning at 700 rpm; bath temperature 1250°C; and slag N-FB

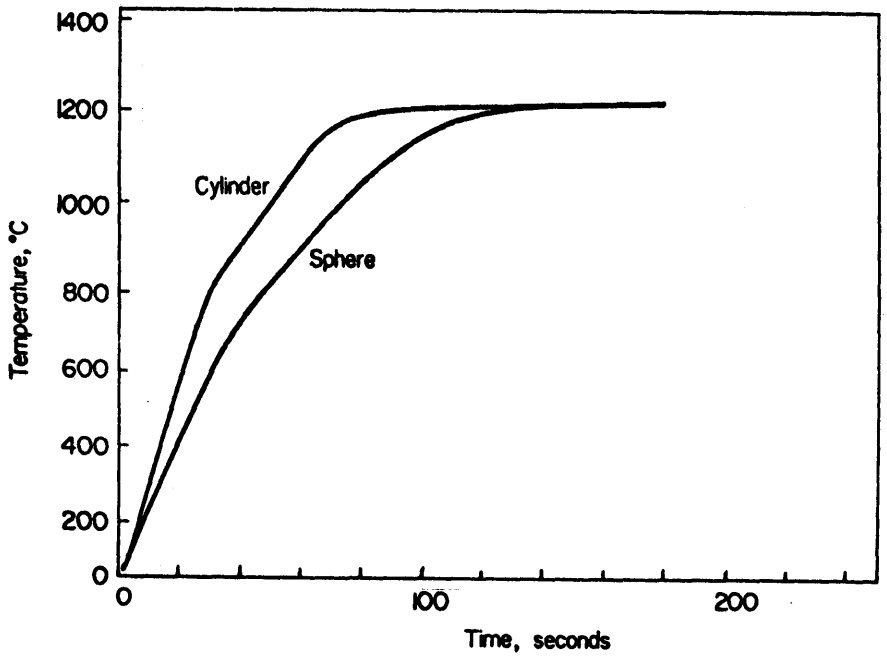

Figure IV-22 Comparison of the heating curves of a 3 cm. nickel sphere and a 1.5 cm. nickel cylinder with the same volume. Conditions: spinning at 700 rpm; bath temperature 1200°C; and slag N-1CU

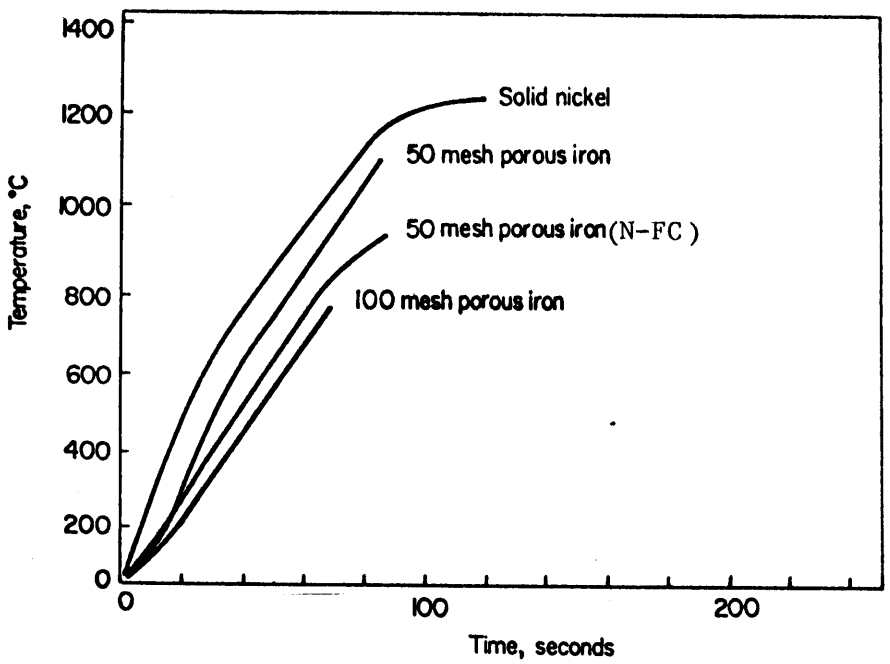

Figure IV-23 Comparison of the heating curves of a solid nickel sphere, a 50 mesh porous iron sphere, and a 100 mesh porous iron sphere. Conditions: 3 cm. sphere; spinning at 700 rpm; bath temperature 1200°C, and slag N-1CU (and N-FC)

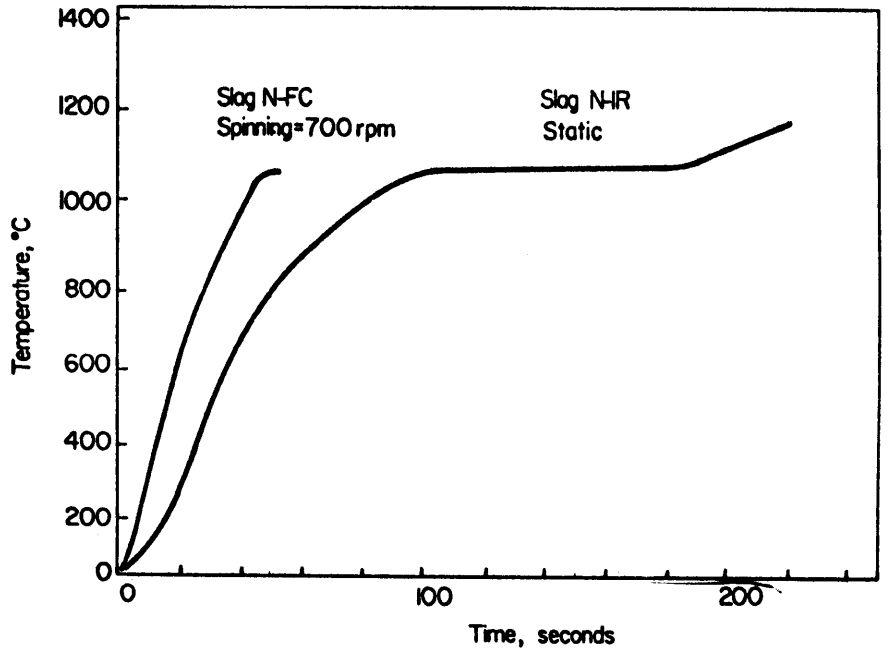

Figure IV-24 Comparison of the heating curves of a copper sphere spinning in slag N-FC at 1250°C and static in slag N-IR at 1330°C. Conditions: 3 cm. copper sphere; and spinning at 700 rpm.

IV.B. Differential Thermal Analysis

When the temperature of the iron crucible in the DTA furnace reached the solidus temperature of the slag, the powdered slag sample began to melt and absorb heat. The temperature of the powdered alumina reference continued to increase normally at 10° per minute. This created a positive temperature difference, ΔT, between the reference and the sample which was plotted against the recorded temperature of the slag sample, as shown in Figure IV-25. The solidus was the temperature at which the ΔT increased significantly from the base line in the figure. The liquidus was the temperature at which the ΔT returned to the base line. After the slag sample was completely liquid, the furnace was cooled at 10° per minute. The liquidus temperature was then observed when the ΔT began to decrease, as shown for slag N-FB in Figure IV-25. The solidus temperature was difficult to determine from the DTA curve upon cooling, because the sample did not solidify uniformly. Since there was cooling by the highly conducting thermocouple, there may have been unsolidified slag in the bottom of the crucible after the slag as the thermocouple was below the solidus temperature. This nonuniform solidification may have caused the slow decay of the ΔT during cooling.

DTA curves were obtained for KCl and the silicate slags for which the thermal diffusivity had been measured (3, 4), and the curves are shown in Figure IV-15. The solidus and liquidus temperatures are listed in Table IV-2.

The established melting point of KCl is 776°C. From the DTA curve

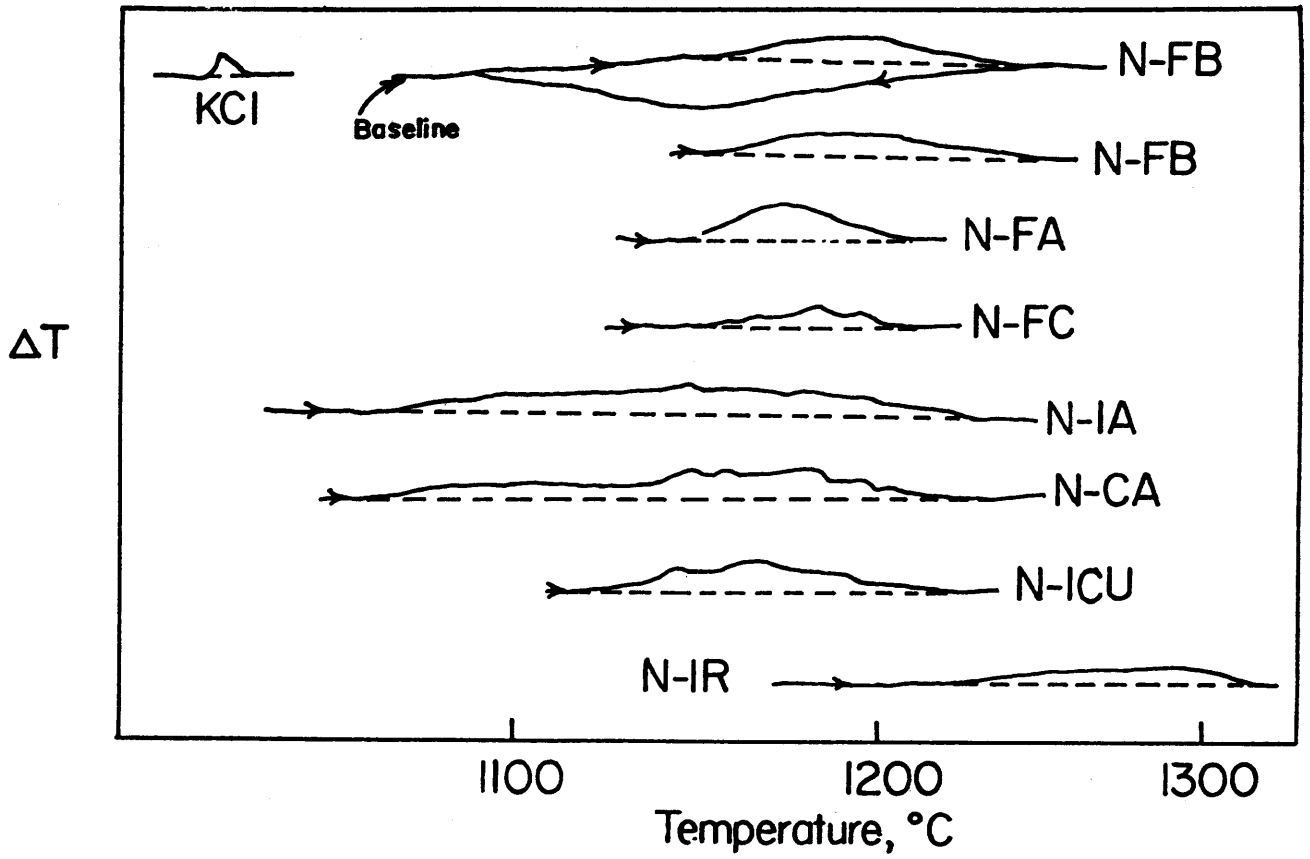

Figure IV-25 Differential thermal analysis curves for KCl and slags

for heating in Figure IV-25, the onset of melting occurred 2 to 3 degrees below the melting point. Also melting continued 4 to 7 degrees after the melting point of KCl. A similar error of about +2° and -5° would be expected for the solidus and liquidus temperature, respectively, using the present DTA apparatus. The +2° correction for the solidus was small enough to neglect, the but the 5° for the liquidus was subtracted from the temperature on the DTA curve.

For the simplest ferrous silicates N-FA, N-FB, and N-FC, an expected melting range is also listed in Table IV-2. This melting range is based on equilibrium solidification of the liquid in the $FeO-SiO_2-Fe_2O_3$ system shown in Figure III-7. The agreement is fairly good. The expected solidus temperature is somewhat lower than the measured solidus, due to the low sensitivity of the millivolt recorder in the ΔT axis.

Table IV-2. Solidus and Liquidus Temperatures

Slag	Solidus-Liquidus Temperatures	Expected* Melting Range
N-FB	1170-1240	1160-1240
N-FA	1150-1210	1140-1240
N-FC	1150-1215	1150-1240
N-1A	1070-1225	
N-CA	1060-1225	
N-1CU	1125-1220	
N-IR	1230-1310	

* Equilibrium solidification of slag. $FeO-SiO_2-Fe_2O_3$ system in Figure III-7.

V. MATHEMATICAL MODELS OF HEAT TRANSFER

A mathematical model is developed which simulates the heat transfer to a cold metal particle immersed in a high melting point liquid, such as in the present heat transfer experiments. The model uses the available data for the thermal properties of silicate slags and various boundary conditions for the solidification and melting of the slag on a metal particle. This model can be used to analyze the results in the present heat transfer experiments and can be applied directly to practical operations of feeding iron pellets into an electric furnace.

Since the principal purpose of this model is to aid in the analysis of the present experiments, the following calculations are necessary: 1) heat transfer in the liquid boundary layer, 2) movement of the solid-liquid slag interface, 3) temperature distribution within the slag shell, 4) temperature distribution in the metal sphere, and 5) response of the thermocouple at the center of the sphere. This chapter describes the formulation of the mathematics for a finite difference model of heat transfer to a cold metal particle immersed in a liquid slag.

V.A. Thermal Conduction by Finite Difference

Non-steady state heat conduction in a sphere can be calculated by finite difference equations (37). In these calculations the system is divided into spherical shell elements with a finite thickness Δr, as shown in Figure V.1. The heat flow into the spherical element i is the sum of the heat flow from the i+1 element and the i-1 element. Assuming a constant heat flow from these adjacent elements, the heat flow is

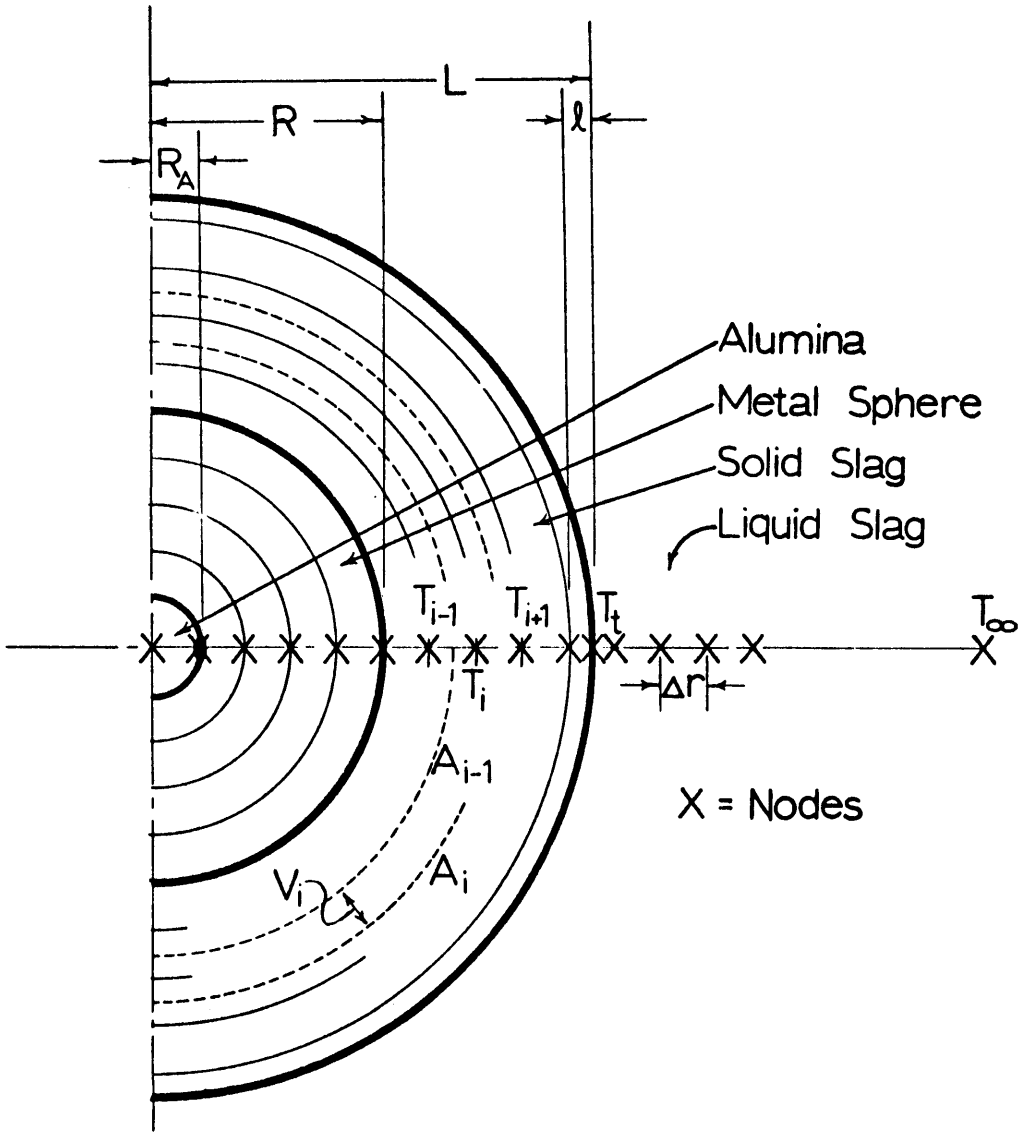

Figure V-1 Finite elements for conduction in the alumina, metal sphere, and the solid slag shell

written in finite difference form,

$$Q = KA_i \frac{(T_{i+1,j} - T_{i,j})}{\Delta r} + KA_{i-1} \frac{(T_{i-1,j} - T_{i,j})}{\Delta r} \qquad (1)$$

where K is the thermal conductivity of the material

A_i is the outside surface area of the element i

A_{i-1} is the inside surface area of the element i

$T_{i,j}$ is the temperature at the center of the element

$T_{i+1,j}$ is the temperature at the center of the outside adjacent element

$T_{i-1,j}$ is the temperature at the center of the inside adjacent element

At non-steady state the heat flow into the element i in equation (1) is used to increase the temperature of the element over a finite period of time t. This heating of the element may be written in a forward difference form

$$Q = \frac{V_i c\rho (T_{i,j+1} - T_{i,j})}{\Delta t} \qquad (2)$$

where V_i is the volume of the element i

$T_{i,j+1}$ is the temperature at the center of the element i after time t

c is the specific heat of the material

ρ is the density of the material

Combining Equations (1) and (2), the temperature at the center of the element i after a finite time can be written

$$T_{i,j+1} = T_{i,j} + \frac{\alpha \Delta t}{\Delta r V_i} [A_i (T_{i+1,j} - T_{i,j}) + A_{i-1} (T_{i-1,j} - T_{i,j})] \qquad (3)$$

Given the initial temperatures, the temperature of these elements may be calculated explicitly with Equation (3). This equation is used to calculate the temperature distribution in the solid metal sphere and the solid slag shell shown in Figure V-1 as functions of time. At the interface between the solid metal sphere and the solid slag shell, the forward difference equation for the element is

$$\frac{K_M A_M}{\Delta r}(T_{M,j}-T_{R,j}) + \frac{K_S A_S}{\Delta r}(T_{S,j}-T_{R,j}) = (V_M c_M \rho_M + V_S c_S \rho_S)(T_{R,j+1}-T_{R,j}) \quad (4)$$

where A_M is the inside surface area of the interface element in the metal

A_S is the outside surface area of the interface element in the slag

K_M is the thermal conductivity of the metal

K_S is the thermal conductivity of the solid slag

$T_{M,j}$ is the temperature of the adjacent metal element

$T_{S,j}$ is the temperature of the adjacent slag element

$T_{R,j}$ is the temperature of the interface element

$T_{R,j+1}$ is the temperature of the interface element after time Δt

V_M is the volume of the metal in the interface element

V_S is the volume of the slag in the interface element

c_M is the specific heat of the metal

c_S is the specific heat of the slag

ρ_M is the density of the metal

ρ_S is the density of the slag

When the solid slag melts away from the surface of the metal sphere the boundary condition at the metal-liquid slag interface is

$$\frac{K_M A_M}{\Delta r}(T_{M,j}-T_{R,j}) + h(T_\infty-T_{R,j}) = V_M c_M \rho_M (T_{R,j+1}-T_{R,j})$$

where h_L is the heat transfer coefficient in the liquid slag, and T_∞ is the temperature of the bulk slag.

The other boundary conditions in this system are discussed in detail in the subsequent sections in this chapter.

V.B. Thermocouple-Metal Interface

Heat transfer from the metal sphere to the thermocouple positioned at the center of the sphere determines the temperature recorded by the thermocouple. The thermocouple response measurements in Appendix A show that the material around the thermocouple is critical to this heat transfer. Inside the experimental sphere there were two thermocouple arrangements: a 1 mm. thick alumina refractory protection tube, and a 0.3 cm^2 piece of platinum foil.

When alumina insulated the thermocouple from the nickel wall in Figure IV.3, poor surface to surface contact and radiation heat transfer is assumed at the interface. The heat transfer by conduction is modelled by assuming a 5% alumina to metal contact. This 5% surface contact gives response which is consistent with the measurements of thermocouple response presented in Appendix A. The reduced area of contact is used in the boundary equation

$$0.05A_A K_A \frac{(T_{A,j}-T_{I,j})}{0.1} + 0.05A_M K_M \frac{(T_{M,j}-T_{I,j})}{\Delta r} = (V_M c_M \rho_M + V_A c_A \rho_A) \frac{(T_{I,j+1}-T_{I,j})}{\Delta r} \quad (5)$$

where $0.05A_A$ is the surface area of the outside of the alumina element

$0.05A_M$ is the surface area of the inside of the metal adjacent element

K_A is the thermal conductivity of the alumina

c_A is the specific heat of the alumina

ρ_A is the density of the alumina

$T_{A,j}$ is the temperature of the alumina (thermocouple temperature)

$T_{I,j}$ is the temperature at the interface element

$T_{M,j}$ is the temperature in the adjacent metal element

Heat is also transferred by radiation between the alumina and nickel surfaces. The radiation transport to the alumina Q_A is calculated by

$$Q_A = \tilde{T} A_I \sigma \, (T_{I,j}^4 - T_{A,j}^4) \quad (6)$$

$$\tilde{T} = \frac{1}{\frac{1}{\varepsilon_M} + \frac{1}{\varepsilon_A} - 1} \quad (7)$$

where A_I is the area separating the alumina and the metal

T_I is the temperature at the metal surface

ε_M is the total normal emissivity of the metal surface

σ is the Stephan-Boltzman constant

ε_A is the total normal emissivity of the alumina surface

In the case of the platinum foil packed around the thermocouple bead, 10% area of contact is assumed, and the conduction equation is

$$0.1A_P K_P \frac{(T_{P,j}-T_{I,j})}{0.1} + 0.1A_M K_M \frac{(T_{M,j}-T_{I,j})}{\Delta r} = (v_M c_M \rho_M + v_P c_P \rho_P)$$

$$(T_{I,j+1}-T_{I,j}) \qquad (8)$$

where $0.1A_P$ is the surface area of the platinum element

K_P is the thermal conductivity of the platinum

c_P is the specific heat of the platinum

v_P is the volume of the amount of platinum present in the bead and the foil

$T_{P,j}$ is the temperature of the platinum (thermocouple temperature)

The radiation transport to the platinum is given by

$$Q_P = \tilde{T} A_I \sigma \, (T_{I,j}^4 - T_{P,j}^4) \qquad (9)$$

$$\tilde{T} = \frac{1}{\frac{1}{\varepsilon_M} + \frac{1}{\varepsilon_P} - 1} \qquad (10)$$

where ε_P is the total normal emissivity of the platinum surface.

Only the spherical portion of the material surrounding the thermocouple bead is considered in the calculation. This is reasonable because the heat flow in the alumina insulator which reaches out of the sphere is small in comparison to the heat flow within the metal sphere.

V.C. Moving Solid-Liquid Slag Interface

The solid-liquid interface in the slag becomes a moving boundary during transient heat transfer in the slag. The interface may be smooth or rough and crystalline, while the enthalpy of fusion is absorbed or

emitted as the slag solidifies or melts, respectively. This section presents the general nature of the solidification and melting of the slag in terms of the temperatures and the heat balance at the interface.

V.C.1. Structure of the Solid-Liquid Slag Interface

The two general structures of the solid-liquid slag interface are 1) cellular with a "mushy" solid-liquid region and 2) planar with a smooth interface. The temperature at the interface depends on whether the interface is planar or mushy.

For the calculation of the temperature at the solid-liquid slag interface, a steady composition and temperature distribution in the liquid during solidification and melting is assumed. For example, as liquid slag N-FB cools iron precipitates from the liquid first as shown in the polythermal projection of the $FeO-SiO_2-Fe_2O_3$ system in Figure V-2. At 1205° fayalite begins to precipitate and the liquid boundary layer becomes depleted in Fe_2SiO_4 as shown in Figure V-3b. Eventually, the composition of the liquid adjacent to the solid reaches the composition at point P and a small amount of magnetite precipitates. When the composition of the adjacent liquid reaches point S, there is no further change in the liquid. The temperature at this point S is the solidus temperature of slag N-FB. If mass diffusion in the liquid boundary layer is limited the solidification of slag N-FB occurs with a steady composition distribution in the liquid, as shown in Figure V.3b. The solid has the same overall composition of the bulk liquid and the

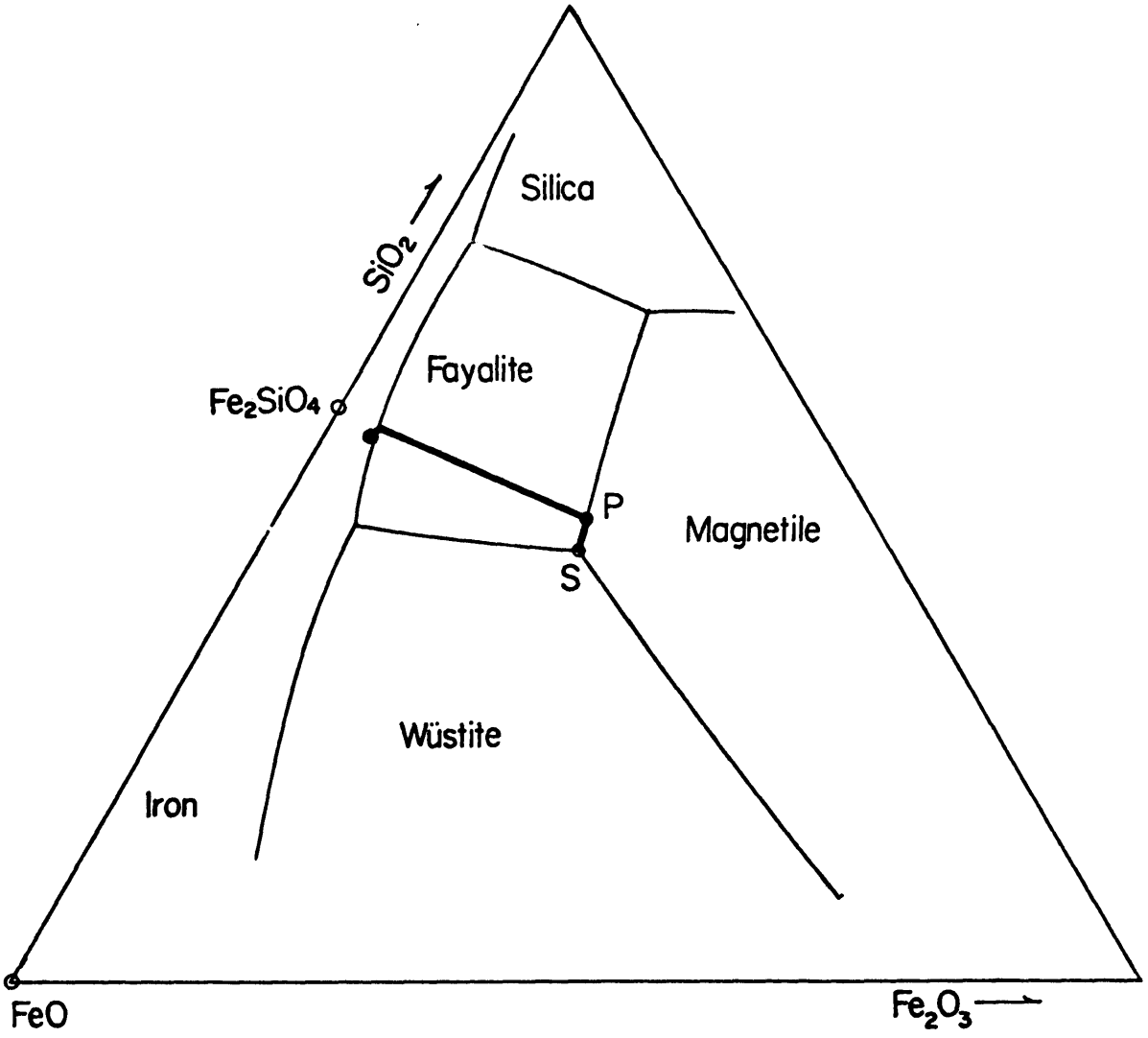

Figure V-2 Liquid compositions for the solidification of slag N-FB (72)

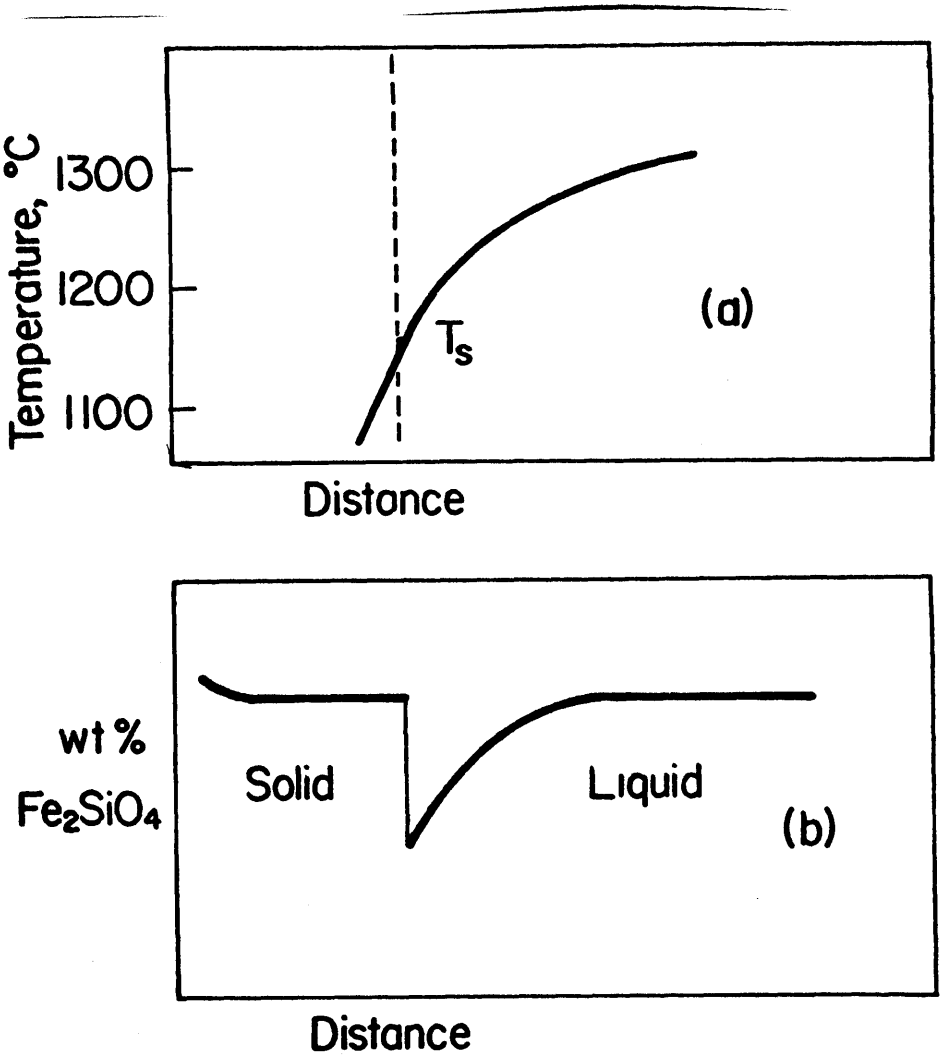

Figure V-3 Temperature and composition distributions during melting and solidification of slag N-FB with a planar interface

adjacent liquid has the composition given by point S. This solidification with a steady composition distribution has been observed for many metals and organic crystals (63). Equilibrium is assumed between the solid and the liquid present.

The interface during the solidification may be planar, under the proper conditions. A general criterion for the stability of a planar interface has been developed. This criterion has been successfully applied to the solidification of metals (63) and organic crystals (65). In its simplest form the criterion for stability of a planar interface is

$$\frac{G}{R} \geq \frac{|m\Delta C|}{D_m} \tag{11}$$

where G is the thermal gradient in the liquid, R is the rate of solidification, D_m is the mass diffusion of the controlling chemical species in the liquid, m is the slope of the liquidus surface in the direction of solidification; and ΔC is the composition over which the material melts. Assuming that the slope of the liquidus is constant, then

$$m \cong \frac{\Delta T}{\Delta C} \tag{12}$$

where ΔT is the melting range. Upon substitution of Equation (12) into Equation (11), the stability criterion is

$$GD_m \geq R\Delta T \tag{13}$$

The application of this stability criterion to the present heat transfer experiments is discussed in Section VI. In the present mathematical model both the planar and mushy interface boundary conditions are presented.

The temperature distribution for a planar interface is shown in Figure V-3a. The temperature at the interface is the solidus temperature during the steady state solidification and melting.

For the mushy interface the temperature distribution is shown in Figure V-4a. The temperature at the tips of the solid cells in the liquid is the liquidus temperature. The temperature at interface between the mushy region and the solid region is the solidus temperature. The composition of the liquid and solid phases for the mushy region is shown in Figure V-4b. The solid and liquid phases in the mushy zone are assumed to always be in equalibrium, and diffusion in the solid is neglected. In the composition curves shown in Figure V-4b, the composition of the solid is the mean composition of the solid present at the given distance and not the composition of the solid in contact with the liquid.

If a glass forms the interface between the liquid and the glass is not distinct and the temperature at this interface may be below the melting temperature of the slag. In the experiments described in Chapter IV, a glass did form immediately upon immersion of the cold metal sphere into the liquid slag. After about 2 to 15 seconds this glass devitrified to form a crystalline solid. Based on this observation the slag shell which solidified on the sphere is assumed to be crystalline for calculations.

In the general case some segregation would be expected in the solid unless the cooling rate is extreme or chemical diffusion in the liquid

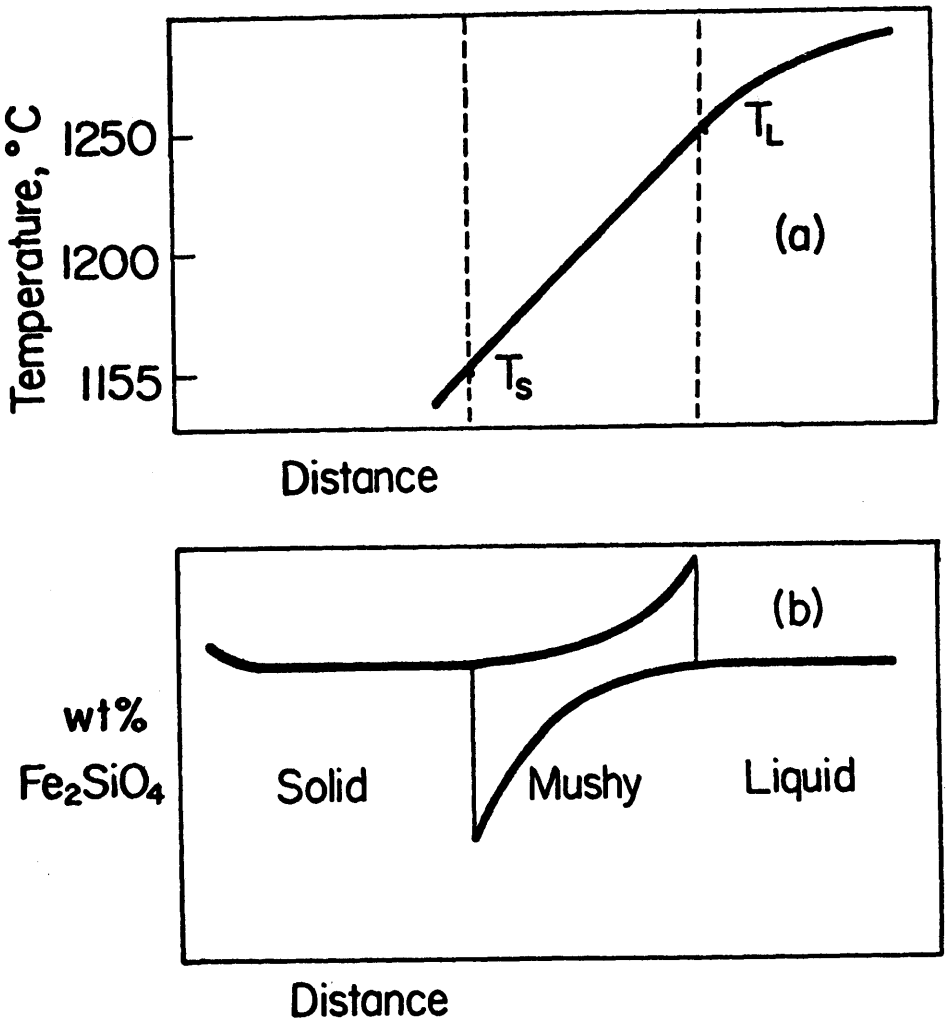

Figure V-4 Temperature and composition distributions during melting and solidification of slag N-FB with a mushy interface.

is limited. These conditions are discussed in Section VI.B.2. For the present calculations segregation is neglected.

V.C.2. Mathematical Boundary Conditions for Planar and Mushy Interfaces

For a planar boundary condition the temperature at the solid-liquid interface is constant.

$$T = T_S \; ; \; r = L_j$$

As suggested in Section V.C.1, this constant temperature is the solidus temperature of the slag.

The position of the solid-liquid interface is calculated by balancing the heat flow at the interface. This heat balance is written in finite difference form, for Figure V-1

$$h_L(T_\infty - T_s) + K_s \frac{(T_i - T_s)}{\ell_j} = \frac{\rho_s \Delta H}{\Delta t} \; (L_{j+1} - L_j) \qquad (14)$$

where T_∞ is the bulk temperature of the liquid slag

h_L is the heat transfer coefficient in the liquid

K_S is the thermal conductivity of the solid slag

ΔH is the heat of fusion of the slag

ρ_s is the density of the solid slag

ℓ_j is the distance from the center of the adjacent element in the solid slag to the solid-liquid interface

T_i is the temperature of the adjacent element in the slag

L_j is the distance from the center of the sphere to the solid liquid interface

L_{j+1} is the distance from the center of the sphere to the solid liquid interface after a finite time Δt.

Equation 14 is rearranged to calculate the position of the interface after the finite time Δt

$$L_{j+1} = L_j + \frac{h\Delta t}{\rho_s \Delta H \ell_j}(T_\infty - T_S) + \frac{K_s \Delta t}{\rho_s \Delta H}(T_i - T_S) \qquad (15)$$

For the mushy boundary condition the temperature distribution is shown in Figure V-5a. This temperature distribution depends on the amount of slag which solidifies in the various portions of the solid-liquid region, as schematically shown in Figure V-5b. For the purpose of calculation the structure of the mushy region is simplified to the rectangular cells shown in Figure V-5c. In this idealized structure a fraction of the slag solidifies at the solidus and the remaining slag solidifies at the liquidus.

The mathematical boundary condition for mushy solidification

$$T = T_S \; ; \; r = L_j$$

$$T = T_L \; ; \; r = L_j + X_j$$

where X_j is the thickness of the mushy region, and T_L is the liquidus of the slag. The position of the boundary at the solidus temperature is calculated from the heat balance

$$K_S \frac{(T_L - T_S)}{X_j} + K_S \frac{(T_i - T_S)}{\ell_j} = f_S \frac{\rho_S \Delta H}{\Delta t}(L_{j+1} - L_j) \qquad (16)$$

where L_j is the distance from the center of the sphere to the solidus boundary of the mushy region, and f_S is the fraction of slag which solidifies and melts at the solidus temperature. The position of the boundary at the liquidus temperature is calculated from a similar heat

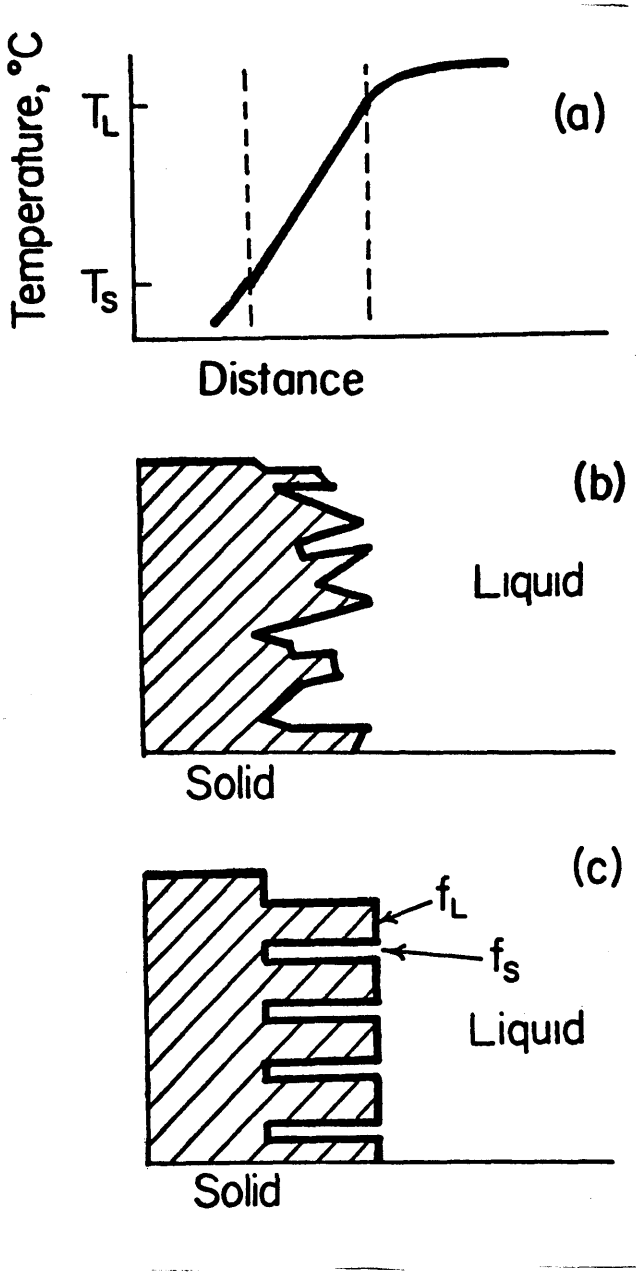

Figure V-5 Representations of a mushy front for solidification and melting

balance,

$$h(T_\infty - T_L) + K_S \frac{(T_L - T_S)}{X_j} = f_L \frac{\rho_S \Delta H}{\Delta t} (L_{L,j+1} - L_{L,j}) \qquad (17)$$

where f_L is the fraction of slag which solidifies and melts at the liquidus temperature, and $L_{L,j+1}$ is the distance from the center of the sphere to the liquidus boundary. The following relationships hold true throughout the calculation.

$$f_L + f_S = 1 \qquad (18)$$

$$L_j < L_{L,j}$$

If the rate of growth at the solidus temperature is approximately equal to the rate of growth at the liquidus temperature, Equations (16) and (17) may be added to give the simple boundary condition

$$h_L(T_\infty - T_L) + K_S \frac{(T_i - T_S)}{\ell_j} = \frac{\rho_s \Delta H}{\Delta t} (L_{j+1} - L_j) \qquad (19)$$

This boundary condition is similar to the boundary condition for the planar interface, as shown in Equation (14), except the solidus temperature T_S in Equation (14) is replaced by the liquidus temperature T_L.

A computer program was written which uses the finite difference equations for the moving interface and the temperatures in the metal, slag, and at the thermocouple. This program calculates the temperatures of the individual elements and the position of the moving interface for successive time increments Δt. The result is a temperature at the center of the sphere which should be comparable to the temperature recorded by the thermocouple at the center of the metal sphere immersed in liquid slag.

Such comparisons will be shown in Chapter VI. The details of the computer program are shown in Appendix D.

V.D. Heat Transfer Coefficients

This section and the remainder of this chapter presents the conditions and properties which are used in the mathematical model to simulate the experimental heating of the metal sphere in the slag.

V.D.1. Forced Convection by Spinning

The heat transfer coefficient for the surface of a spinning sphere is calculated from the empirical correlation developed by Krieth et al. (11)

$$\bar{N}_{Nu} = 0.43\ N_{Re_S}^{0.5}\ N_{Pr}^{0.4} \tag{20}$$

$$N_{Re_S} < 5 \times 10^5$$

$$0.7 < N_{Pr} < 215$$

$$N_{Gr} < 0.1\ N_{Re_o}^2$$

where $\bar{N}_{Nu} = \dfrac{\bar{h}_L D}{K_L}$ (21)

$$N_{Re_S} = \frac{wD^2 L}{\mu}$$

$$Np_r = \frac{\mu}{\rho_L \alpha_L}$$

$$N_{Gr} = \frac{\beta_g D^3 (T_\infty - T_S)^2}{\mu}$$

where D is the diameter of the sphere

K_L is the thermal conductivity of the liquid slag

$\bar{h}_L$ is the mean heat transfer coefficient

w is the spinning frequency

μ is the viscosity of the slag

ρ_L is the density of the liquid slag

α_L is the thermal diffusivity of the liquid slag

β is the linear coefficient of thermal expansion of the liquid slag

T_∞ is the bulk temperature of the slag

T_S is the temperature at the solid-liquid interface

With the properties of the liquid slag and the spinning velocity of the sphere, heat transfer coefficients are calculated for the experimental conditions.

The heat transfer coefficient for the spinning cylinder is calculated from an empirical correlation developed by Eisenberg et al. (50, 56)

$$\bar{N}_{Nu} = 0.079\ N_{Re_v}^{-03}\ N_{Pr}^{-0.644} \qquad 100 < N_{Re_v} \tag{22}$$

where

$$N_{Re_v} = \frac{\bar{V} D \rho_L}{\mu}$$

$$\bar{V} = \pi w D$$

V.D.2. Natural Convection

For the static sphere suspended in the slag, the heat transfer coefficient is calculated from the empirical correlation (66)

$$\bar{N}_{Nu} = 2.0 + 0.06\ N_{Gr}^{1/4}\ N_{Pr}^{1/3} \tag{23}$$

$$N_{Gr}^{1/4} \; N_{Pr}^{1/3} \; < 200$$

V.D.3. Forced Convection by Rising Bubbles

Two sets of heat transfer coefficients are calculated for the conditions of bubble stirring in the slag. 1) using the velocity of the fluid which is drawn upward by the bubbles, and 2) using the power dissipated by the rising bubbles.

The heat transfer coefficient for a sphere which is suspended in a laminar flow of fluid can be calculated by the Ranz-Marshell correlation (78)

$$\bar{N}_{Nu} = 2.0 + 0.6 \; N_{Rev}^{1/2} \; N_{Pr}^{1/3} \qquad (24)$$

where

$$N_{Re_v} = \frac{V_f D \; L}{\mu}$$

where V_f is the velocity of the rising fluid. Gal-Or et al. (58, 59) calculated the velocity of a fluid drawn upward by a swarm of rising bubbles

$$V_f = \frac{(\rho_L - \rho_b) \; r_b^2 g}{3 \; \mu} \left[\frac{\frac{2}{15} \phi^{4/3} - \phi^{1/3} - \frac{\phi}{3} - \frac{6\phi}{5}^{1/3}}{\left(\frac{1}{\phi^{1/3}}\right)^2 - 1} - \frac{2\phi}{15}^{1/3} + \phi - \frac{6\phi}{5}^{1/3} \right] \qquad (25)$$

where r_b and ρ_p are the mean radii and density of the rising bubbles, ϕ is the volume fraction of bubbles, and μ is the viscosity of the fluid.

The volume fraction of rising bubbles in the slag is related to the gas flow rate F, by the equation

$$\phi = \frac{F}{A_c V_b} \qquad (26)$$

where V_b is the velocity of the rising bubbles, and A_c is the cross-sectional area of the rising column of bubbles. Gal-Or et al. (59) also calculated the velocity of the rising bubbles as a function of the volume fraction.

$$V_b = \frac{(\rho_L-\rho_b)r_b^2 g}{3\mu}\left[\frac{\frac{2\phi}{15}^{4/3} - \phi^{1/2} - \frac{\phi}{3} - \frac{6\phi}{5}^{1/3}}{(\frac{1}{\phi_s})^2 - 1} - \frac{\phi+2}{3}\right] \qquad (27)$$

The relationship between the velocity of the fluid and the gas flow rate of bubbles is demonstrated in Figure V-6, based upon the calculations of Gal-Or, et al.

The heat transfer coefficient for the sphere suspended in the column of rising bubbles is calculated using the experimental gas flow rates, the properties of the liquid slag, and the bubble radius observed in the glycerol solution at the given gas flow rates.

The calculations made by Gal-Or et al. were based on several ideal assumptions that limit their application. The bubbles were assumed to be hard spheres enclosed in spherical cells of fluid. It was assumed that the surface of the fluid cells had no net heat flux. The flow of the fluid was laminar. In the present slag experiments, the bubbles are not perfect spheres and at the higher gas flow rates the fluid may not remain laminar. Although the ideal conditions used for the calculations do not exist in the present system, there are experimental results with gas bubbling columns (21, 60) which are similar to the present experiments and that agree with the results of Gal-Or et al. The limits to

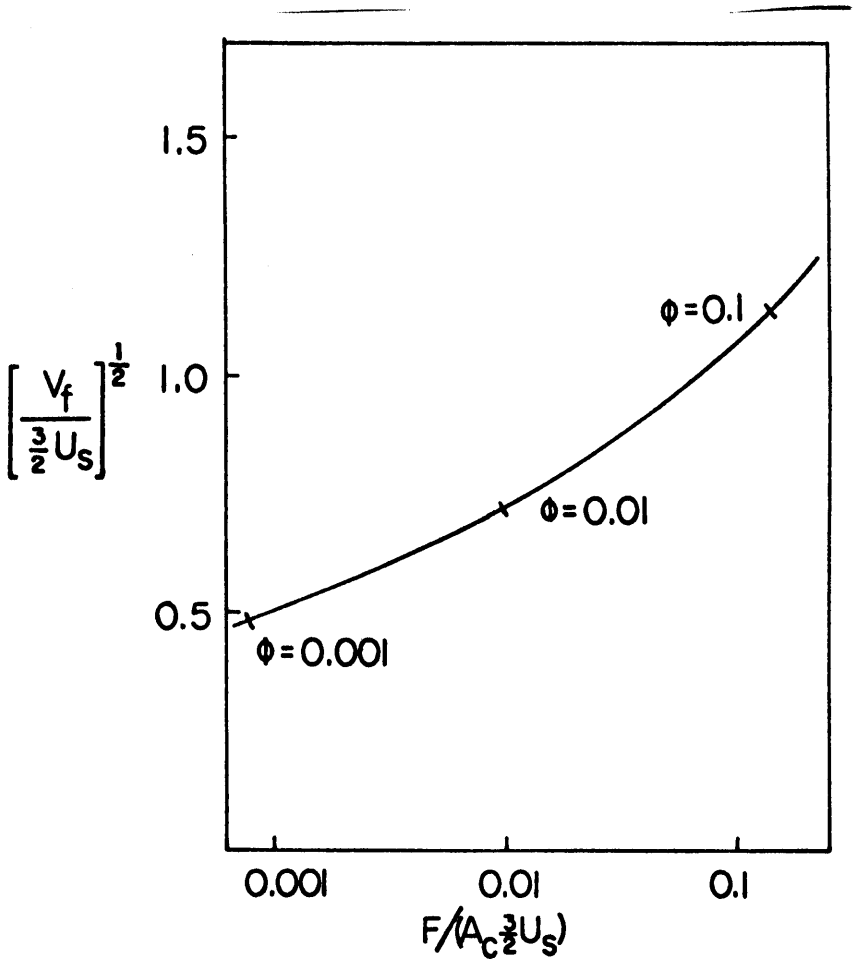

Figure V-6 Relationship between the volumetric gas flow rate of a column of bubbles and the velocity of the fluid drawn upward by the bubbles.

$$U_S = \frac{2}{3}\frac{(\rho_L - \rho_b)\ r_b^2 g}{\mu}$$

applying these calculations to the present experiments are further discussed in Section VI.D.2.

Another set of heat transfer coefficients are calculated for the conditions of bubble stirring in the slag, by calculating the power dissipated by the bubbles rising in the slag. Brian and Hales (16, 17) correlated the heat transfer coefficients for spheres suspended in a stirred tank. They found that the data correlated very well with the dimensionless power number, as shown in Figure V-7. The dashed line in this figure represent the correlation for the properties of the slag N-1CU.

To use the correlation in Figure V-7 the power dissipation per unit mass P/m is calculated from the work done by the buoyancy and expansion forces on the rising bubbles. The work per unit volume during the rise of a single bubble was calculated by Nakaniski et al. (62).

$$dW = V\rho_L g dy + PdV \qquad (28)$$

where V is the volume of a single bubble, y is the vertical distance from the submerged orifice, and P is the pressure of the gas in the bubble. Assuming that the nitrogen is an ideal gas, this equation is integrated over the height of the column of bubbles Y to give

$$W = 2nRT_\infty \left(1 + \frac{\rho_L g Y}{P_a}\right) \qquad (29)$$

where P_a is the atmospheric pressure, and T_∞ is the bath temperature. This work is then used to calculate the power dissipation per unit mass of slag at the volumetric gas flow rate F (ml/sec.)

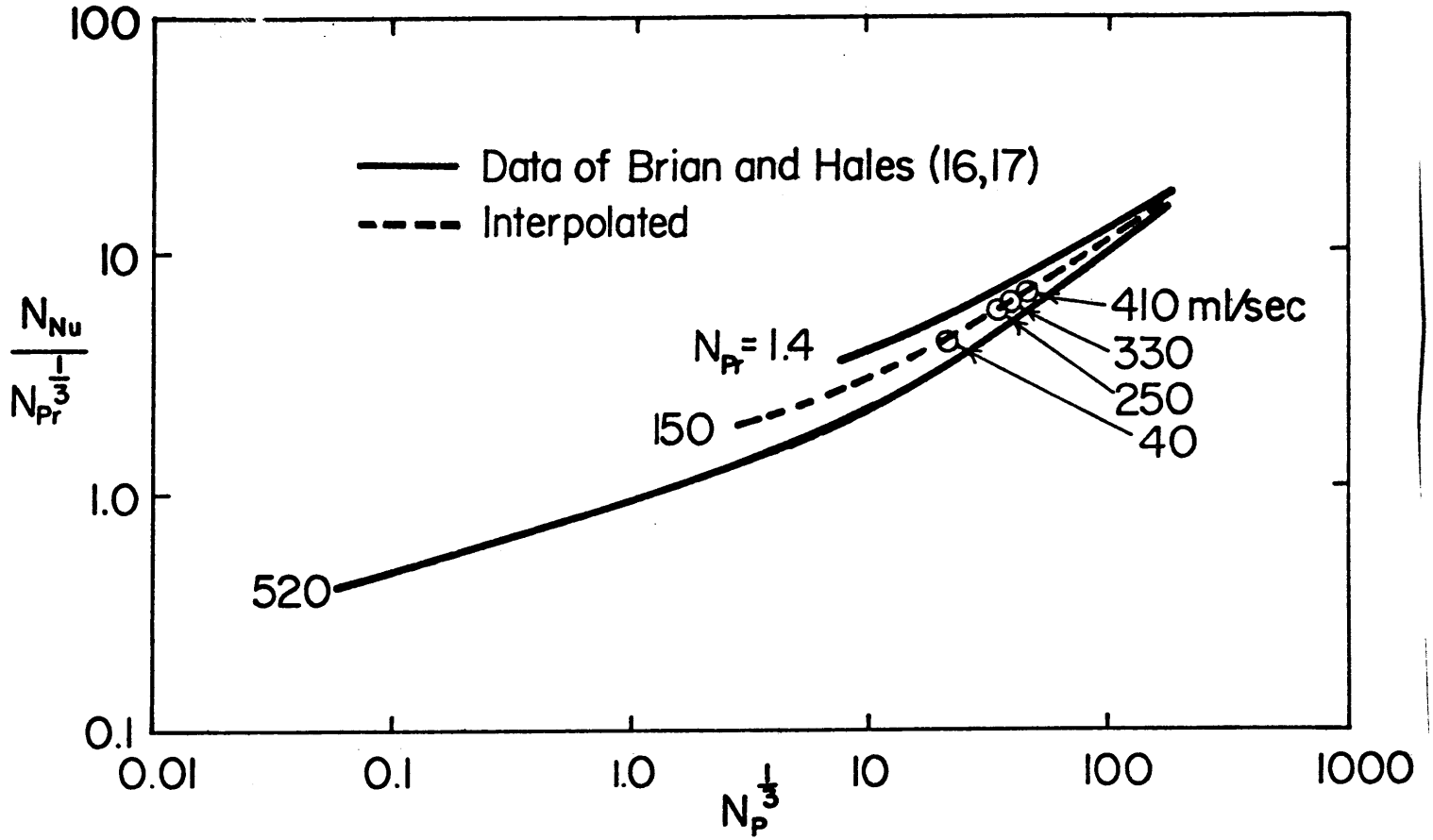

Figure V-7 Heat transfer coefficients correlated to a dimensionless power number N_P based on the experimental and theoretical work of Brian and Hales (16, 17). Dashed line represents the interpolated correlation for a slag with N_{Pr} = 150. Circles are the power numbers for the correlation that represent the experimental conditions using equation 31.

Table V.1. Experimental Fluid Flow Conditions for Figure IV-5.

	Flow Conditions	Bubble Radius, r_b (cm)	F/A$_c$ (cm/sec)	Rising slag N_{Nu} [2]	$N_p^{1/3}$ [3]	Power Dissipation N_{Nu} [4]
1	Spinning (700 rpm)			41.6		
2	Natural Convection			2.3		
3	Bubble 40 ml/sec[1]	0.2	0.8	28.3	20.4	22.0
4	250	0.4	5.0	64.9	37.2	30.0
5	330	0.5	6.6	78.5	40.9	31.5
6	410	0.5	8.2	82.0	43.9	34.0

[1] at the temperatureof the slag

[2] from Equation (24, Chapter V

[3] from Equation (31), Chapter V

[4] from Figure V-7.

$$P/m = \frac{1.09 \times 10^7}{\rho_L Y} \left(\frac{F}{A_c}\right) \ln \left(1 + \frac{\rho^Y}{103.3}\right) \left(\frac{\text{Watts}}{\text{gm}}\right) \qquad (30)$$

The volumetric flow rate is based on the temperature of the gas in the liquid slag.

For the experimental conditions listed in Table VI-1, the Nusselt number, $\frac{h_L D}{K_L}$, is calculated and listed in this table. The power number N_p is defined as

$$N_p = \frac{P/m \; D^4 \rho_L^3}{\mu^3} \qquad (31)$$

For the conditions of bubble mixing, the Nusselt numbers based on both the velocity of the rising bubbles and the power dissipation of the bubbles are shown.

V.E. Properties of Slag

In this section the properties of the slag which are used in the mathematical model are described.

V.E.1. Properties of Liquid Slags (Table III-4)

The thermal diffusivities of the slags listed in Table III-4 were measured previously in this laboratory (3, 4). The thermal diffusivity of the liquid for the model calculations was taken directly from this data.

The thermal conductivity of the liquid is calculated from the relationship

$$K_L = \alpha_L c_L \rho_L \qquad (32)$$

where c_L and ρ_L are the specific heat and density of the liquid slag.

The specific heat for all of the liquid slags except slag N-IR is the specific heat reported for Fe_2SiO_4 (39). For the specific heat of slag N-IR the specific heat of the individual oxides, FeO, SiO_2, CaO, MgO, and Al_2O_3, are averaged according to Kopp's law (9) at 1350°C.

The densities for all of the liquid slags except for slag N-IR are based on the measurements by Lee and Gaskell (8). The densities for slag N-FB and N-CA were measured by them, and this densities are used directly in the model. The densities of the other slags, except slag N-IR, are interpolated from the measurements and the effects of FeO and SiO_2 on the density reported by Lee and Gaskell. For slag N-IR the density of the solid slag is used for the density of the liquid.

The thermal coefficient of expansion of the liquid slag is the average value reported by Lee and Gaskell for slags N-CA and N-FB (8).

For slags N-FA, N-FB, and N-FC (in the FeO-SiO_2 system at iron saturation) the viscosity was compiled by Elliott et al. (38). These values of viscosity are directly used for these slags. The viscosity of slag N-FC is also used for slags N-CA, N-1A, N-2A, N-1CU, and N-2CU, because they had similar fluidity during the laboratory experiments. The viscosity of slag N-IR is estimated from the values for similar steelmaking slags listed by Elliott et al. (38).

V.E.2. Properties of the Solid Slag (Table III-5)

The thermal diffusivity of the solid slag for the model calculation is taken directly from the measurements made in this laboratory. The

thermal conductivity is calculated from the equation

$$K_S = \alpha_S c_S \rho_S \qquad (33)$$

where c_S and ρ_S are the specific heat and density of the solid slag.

The specific heat for all of the liquid slags except slag N-IR is the reported specific heat of Fe_2SiO_4 (9) at 1000°C. For slag N-IT the specific heat is the average of the specific heat of the simple oxides present at the 1000°C (39). The effect of temperature on specific heat is neglected because most of the solid slag remains above 1000° during an experiment with the immersed sphere.

The density of the solid slags was measured in this laboratory by weighing a sample of slag, dry, and then immersed in water. This measurement gave the density of the solid slag at ambient temperature. Since the density of the slag is less at the experimental temperature, this density at ambient temperature is corrected by assuming a 1% thermal expansion. The 1% thermal expansion is the average expansion for fayalite and silica from 25 to 1000°C (39). The density listed in Table V-3 is the corrected value which is used in the model calculations.

The solidus temperatures are taken directly from the differential thermal analysis which is presented in Section IV.B, Table IV-2.

The heat of fusion for slag N-FB is the reported heat of fusion for fayalite (10). The heat of fusion for slag N-IR is the heat of fusion for calcium silicate (10). For slags N-FA and N-FC the heat of fusion is the average of the heat of fusions reported for fayalite (10), silica (38) and wustite (38), using the proportions of these oxides present as

calculated from the compositions of the slags. The heat of fusion for N-CA, N-1A, N-2A, N-1CU, and N-2CU, because the compositions are similar and no better values are available.

V.F. Thermal Conductivity of the Porous Sphere

The thermal conductivity of the porous iron spheres which were used in some of the experiments is calculated by the geometric mean of the thermal conductivities (43)

$$K_M = K_I^{(1-\psi)} \; K_P^{\psi} \tag{34}$$

where K_M is the thermal conductivity of the porous metal, K_I and K_P are the thermal conductivity of the solid iron and gas in the pores, respectively. The ψ is the porosity or pore fraction by volume. The geometric mean of the thermal conductivities agrees reasonably well with the measured thermal conductivity of porous metals (48) and porous oxides (47) over a range of porosity from 0.03 to 0.5.

The thermal conductivity of the iron is calculated as a function of temperature from the reported measurements between 300°K and 1400°K (9)

$$K_I = \frac{42}{T} + 0.0519 \text{ (cal/cm-sec-°C)} \tag{35}$$

The thermal conductivity of the pores is calculated from the sum of the radiation K_R and conduction K_c contributions

$$K_p = K_R + K_c \tag{36}$$

From the reported data for the thermal conduction of air between 500° and 1500°K (9), the thermal conductivity of the pores is

$$K_c = 3.04 \times 10^{-4} \left[1-\exp\left(-7.65 \times 10^{-4} T\right)\right] \text{ (cal/cm-sec-°C)} \quad (37)$$

The radiative thermal conductivity in the pores is based upon the approximation suggested by Marino (44) and Loeb (76) for homogeneously distributed spherical pores

$$K_R \simeq 3\sigma T^3 d \quad (38)$$

where σ is the Stephan-Boltzman constant and d is the diameter of the pores.

The diameter of the pores in the sintered iron spheres used in the present experiments is mean pore diameter observed on a polished cross-section of the sphere. The porosity of the metal is calculated from the measured weight of the porous sphere m_M

$$\psi = \frac{3m_M}{4\pi R^3 \rho_I} \quad (39)$$

where ρ_I is the density of pure iron, and R is the radius of the sphere.

V.G. Melting Copper Spheres

The melting of the copper is calculated in the mathematical model for the experiments with solid copper spheres (described in Section III.D.5). When the surface temperature of the copper sphere in the model calculation reaches the melting temperature, 1356°K, the boundary condition at the copper-solid slag interface is

$$T = 1356°K; \quad r = R \quad (40)$$

The heat flow from the solid shell is then balanced at this interface

$$\rho_M \Delta H_M \frac{\Delta V}{\Delta t} = A_M K_S \frac{(T_i - 1356°K}{\Delta r} \quad (41)$$

where ΔV is the volume of copper which is melted in the time increment Δt. This boundary condition applies until the total volume of melted copper is equal to the total volume of copper present.

V.H. Dimensional Analysis

The differential equations which describe heat transfer in the metal sphere and the solid slag shell are written in dimensionless form

$$\frac{1}{(\frac{r}{D})} \frac{\partial}{\partial(\frac{r}{D})} \left(\frac{(\frac{r}{D})\,\partial(\frac{T-T_o}{T_\infty-T_o})}{\partial(\frac{r}{D})} \right) = \frac{\partial(\frac{T-T_o}{T_\infty-T_o})}{\partial(\frac{\alpha_M t}{D^2})} \qquad (42)$$

$$\frac{1}{(\frac{r}{D})} \frac{\partial}{\partial(\frac{r}{D})} \left(\frac{(\frac{r}{D})\,\partial(\frac{T-T_o}{T_\infty-T_o})}{\partial(\frac{r}{D})} \right) = \frac{\partial \frac{T-T_o}{T_\infty-T_o}}{\partial(\frac{\alpha_s t}{D})} \qquad (43)$$

where r is the radial distance from the center of the sphere

D is the diameter of the sphere

T is the temperature at the radial distance r

T_o is the initial temperature of the sphere

T_∞ is the bulk temperature of the slag

α_M is the thermal diffusivity of the metal

t is the time

α_S is the thermal diffusivity of the slag

The heat balance at the solid liquid slag interface is written in dimensionless form for a smooth or planar interface

$$\frac{d\,\frac{L}{D}}{d\left(\frac{\alpha_s t}{D^2}\right)} = \frac{(T_\infty - T_o)C_s}{\Delta H_S}\,\frac{d\left(\frac{T-T_o}{T_\infty - T_o}\right)}{d\,\left(\frac{r}{D}\right)} - \frac{c_s D h_L}{R_s \Delta H}\,(T_\infty - T_s)$$

where c_s is the specific heat of the solid slag

ΔH is the heat of fusion of the slag

K_S is the thermal conductivity of the solid slag

h_L is the heat transfer coefficient

T_S is the solidus temperature of the slag

The heat balance at the solid slag metal interface is written in dimensionless form

$$\frac{d\,\left(\frac{T-T_o}{T_\infty - T_o}\right)}{d\left(\frac{r}{D}\right)} = \left(\frac{K_s}{K_M}\right)\,\frac{d\left(\frac{T-T_o}{T_\infty - T_o}\right)}{d\left(\frac{r}{D}\right)}$$

where K_M is the thermal conductivity of the metal.

Since these equations determine the conditions for heat transfer in the system, there are eight independent dimensionless variables which are required to completely specify the heating of a metal sphere in the presence of a solid slag shell. These variables are rearranged and listed in more familiar forms below.

$$N_{Nu} = \frac{h_L D}{K_L}$$

$$\theta^* = \frac{T_s - T_o}{T_\infty - T_o}$$

$$\alpha^* = \frac{\alpha_M}{\alpha_S}$$

$$\theta = \frac{T-T_o}{T_\infty - T_o}$$

$$r^* = \frac{r}{D}$$

$$\tau = \frac{\alpha_s t}{D}$$

$$\frac{C_s(T_\infty - T_o)}{\Delta H}, \frac{L}{D}$$

The heat transfer coefficient h_L is described in terms of a Nusselt number, N_{Nu}. The solidus fraction * represents the fraction of the temperature range from T_o to T_∞ in which the slag is completely solid. This fraction also represents the difference between the temperature at the surface of the solid slag and the temperature in the bulk of the liquid slag. A^* represents the ratio of the thermal diffusivity of the metal to the thermal diffusivity of the solid slag. The θ, r/D, and $t\alpha_S/D^2$ are the dimensionless temperature, distance, and time for conduction in a sphere, respectively. The remaining dimensionless variables listed above have less direct meaning.

In the present study the most important variables are the temperature θ, the time $t\alpha_S/D^2$, the Nusselt number N_{Nu}, the solidus fraction θ^*, and the diffusivity fraction A^*. These variables will be discussed in detail in Chapter VI.

In the case of a mushy solid-liquid interface, an additional variable must be added to the list. This variable is θ^{**}

$$\theta^{**} = \frac{T_L - T_o}{T_\infty - T_o}$$

where T_L is the liquidus temperature of the slag.

In the case of the melting copper sphere, the solid slag-copper heat balance at the interface is

$$\frac{\rho_M \Delta H_M}{\rho_s c_s (T_M - T_o)} \frac{d\frac{V}{V_o}}{d\frac{\alpha_s t}{D^2}} = \frac{d\frac{T-T_o}{T_\infty - T_o}}{d(\frac{r}{D})}$$

where V is the volume of melted copper, V_o is the original volume of copper, T_M is the melting point of copper, and ρ_M is the density of copper. During the melting of copper, two additional dimensionless variables are

$$\frac{\rho_M \Delta H_M}{\rho_s c_s (T_M - T_o)}$$

$$\frac{V}{V_o}$$

V.I. Convergence and Stability

To test the stability and convergence of the numerical solution of the difference equations presented in this chapter, a dimensionless modulus is defined (37)

$$M = \frac{\Delta t \alpha_s}{\Delta r^2}$$

where Δt and Δr are the finite time increment and width of an element, respectively. This modulus determines the stability of the calculation for the temperature of a finite element by forward difference equations

(52). If the modulus is too large, the temperature change which is calculated for the time Δt is too great to be contained by the element, and the calculated solution is oscillatory or unstable. Fowler (52) determined that the finite difference solution using forward differences is stable and convergent when

$$M < 0.5$$

Convergence is achieved when the solution is reproducible at various values of Δt and Δr at a constant M.

In the present mathematical model, the solution is stable and convergent within 1% when

$$M \leq 0.14$$

This modulus is small because of the movement of the solid-liquid interface within the elements. The limiting distance is the minimum distance allowed between the interface and the center of an element ($0.1\Delta r$).

VI. DISCUSSION

In this chapter the effects of various properties and conditions on the heating of a sphere in a silicate slag are discussed. First an overall heat transfer coefficient is presented which illustrates the effects of the solidified slag shell. Then the separate effects of the moving boundary, conduction in the solid slag, and convection in the liquid are discussed through comparisons between the heating curves obtained from the experiments and calculated from the mathematical model.

VI.A. Overall Heat Transfer Coefficient

The Newtonian heating of the sphere in the liquid slag is given in terms of an overall heat transfer coefficient U,

$$UA_M (T_\infty - T_M) = c_M \rho_M V_M \frac{dT_M}{dt} \qquad (1)$$

where A_M is the area of the metal sphere

T_∞ is the bulk temperature of the liquid slag

T_M is the temperature of the metal sphere

c_M is the specific heat of the metal

ρ_M is the density of the metal

V_M is the volume of the sphere

t is the time

Newtonian heating as described by equation (1) is valid, if the temperature gradient within the sphere is small. This temperature gradient is related to the Biot number

$$N_{Bi} = \frac{UD}{K_M}$$

where D is the diameter of the sphere, K_M is the thermal conductivity of the metal. A low value of the Biot number reflects low resistance to heat flow within the sphere, D/K_M, relative to the resistance of the liquid slag, U^{-1}. In practice, when the Biot number is less than 0.1, the temperature is nearly uniform within the sphere (66). For a nickel sphere of 3 cm. diameter the temperature is uniform within the sphere when the overall heat transfer coefficient U is less than 0.0053 cal/cm^2-sec-$^\circ$C.

From equation (1) an overall heat transfer coefficient is defined

$$U = \frac{c_M \rho_M V_M}{A_M (T_\infty - T_M)} \quad \frac{dT_M}{dt} \qquad (2)$$

The overall heat transfer coefficient is calculated from the experimental heating curves for a nickel sphere immersed in the liquid slag. The temperature of the metal sphere is taken directly from the experimental heating curve, and the differential, dT/dt, is taken from the slope at a point on the curve. This calculated overall heat transfer coefficient varies during the time of immersion, as shown in Figure VI-1. The overall heat transfer coefficients shown in this figure are calculated from the experimental heating curves in Figure IV-5.

If the nickel sphere is heated according to Equation (1), the overall heat transfer coefficient, U, should reflect the growth of the insulating slag shell. The coefficient should decrease initially to a minimum, when the slag grows to a maximum thickness. As the solid shell melts away, the coefficient should increase rapidly to the liquid heat

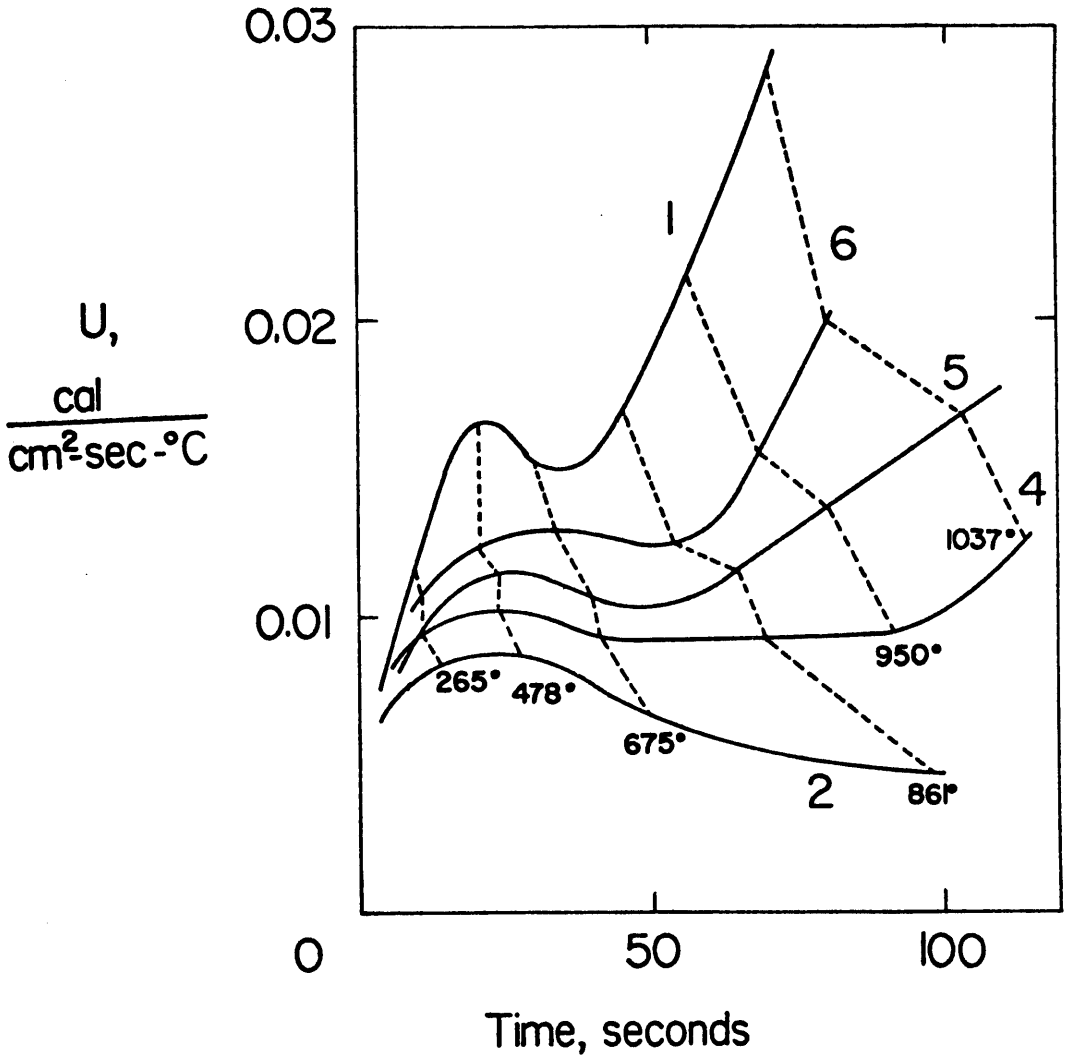

Figure VI-1 Overall heat transfer coefficients for experiments with forced convection by rising bubbles (curves 4,5, and 6), spinning (curve 1), and natural convection (curve 2). Experimental conditions are shown in Figure IV-5. The dashed lines connect the same temperature of the sphere under the various conditions

transfer coefficient, h_L which is described in Section V.D.

The overall heat transfer coefficient which is calculated from the experimental heating curves does reflect the growth of the slag shell. As shown in Figure VI-1, the overall heat transfer coefficient U decreases to a minimum, after an initial transient, and then increases toward the liquid heat transfer coefficient, h_L. The liquid heat transfer coefficient h_L for the spinning sphere in curve 1 is 0.07 cal/cm^2-sec-C°, as calculated from the correlation in Section V.D.1.

The overall heat transfer coefficient for the heating of the sphere by natural convection is somewhat unusual. As shown in curve 2 of Figure VI-1, the overall heat transfer coefficient rises initially and then steadily decreases in the remaining time. The liquid heat transfer coefficient h_L which is calculated from the correlation in Section V.D.2 for natural convection is 0.0045 cal/cm^2-sec-°C. This liquid heat transfer coefficient h_L is lower than the overall heat transfer coefficient which is calculated from the experimental heating curve. The larger overall heat transfer coefficient U is due to the heat which is initially available in the solid slag adjacent to the sphere. This heat from the adjacent slag supplements the heat from the liquid slag.

It should be noted that the calculated heat transfer coefficients U are usually above the maximum value which is allowable for Newtonian heating, 0.0053 cal/cm^2-sec-°C. Although Newtonian heating is not achieved during the heating of the nickel sphere in the slag, the overall heat transfer coefficient U does indicate the effect of the solid slag shell.

IV.B. Slag Solidification and Melting

From the overall heat transfer coefficients, it is clear that the solidification and melting of the slag influence the heating of the sphere. The stability and the effects of the moving solid-liquid interface are discussed in this section. Also, comparisons between the experimental heating curves for the sphere which is immersed in the slag and the calculated heating curves from the mathematical model (described in Chapter V) are presented.

VI.B.1. Calculated Effects of the Planar and Mushy Boundary Conditions

The mathematical model presented in Chapter V is used to calculate the heating curves for a metal sphere. Two different boundary conditions are proposed in Section V.C. for the moving solid-liquid slag interface planar and mushy. For the two boundary conditions, two different heating curves are calculated. The calculated heating curves for a 1.8 cm. spinning nickel sphere in slag N-FB at 1250°C are shown in Figure VI-2. The thickness of the slag shell is also shown in this figure. The melting range for this slag is 1170°C to 1240°C as listed in Table IV-2.

The calculated thickness of the slag shell and the temperature at the center of the sphere depend on the boundary condition which is used. The planar boundary condition produces a thinner slag shell and a higher temperature at the center of the sphere. This is reasonable because the planar boundary condition uses a lower temperature at the solid-liquid interface, the solidus temperature, and the resulting heat flux from the liquid, $h_L(T_\infty - T_S)$, is greater. The mushy boundary condition adds another

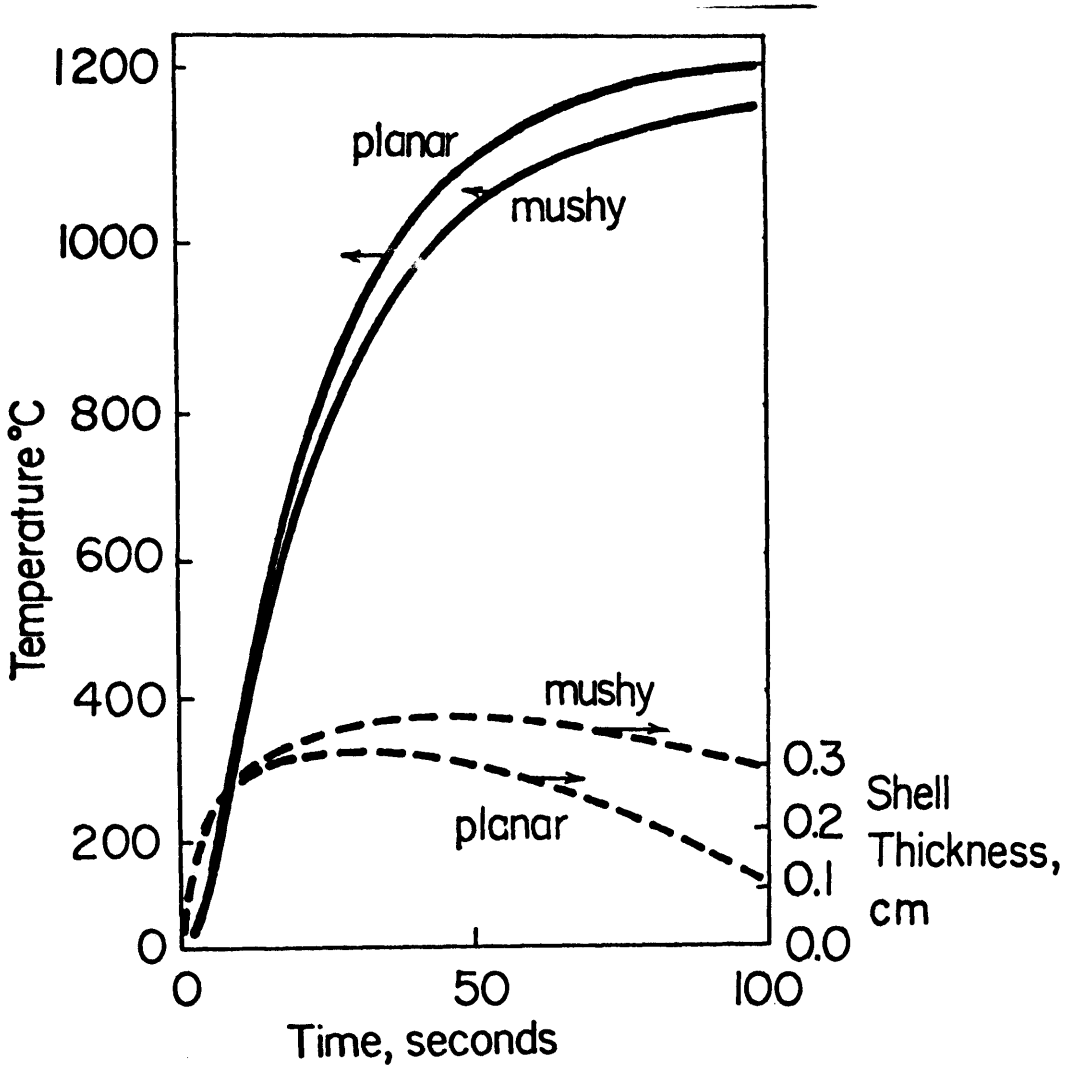

Figure VI-2 Comparison between the calculated heating curves using the model with the planar and mushy front boundary conditions

barrier to the flow of heat and uses the liquidus temperature to determine the heat flux from the liquid $h_L(T_\infty - T_L)$.

VI.B.2. Stability of a Planar Solid-Liquid Boundary

Using the criterion for a stable planar front solidification and melting, as developed in Section V.C.1.

$$GD_m \geq R_t \, \Delta T \qquad (3)$$

the likely conditions of the interface can be estimated. The numerical values of the terms which make up this criterion are shown below for the conditions given in Figure VI-2.

$$G = N_{Nu} \frac{(T_\infty - T_S)}{D} = 1000°C/cm.$$

$$D_m = 10^{-6} \ cm^2/sec$$

$$\Delta T = 62°C$$

$$R_t = 0.042 \ cm/sec$$

The thermal gradient G in the liquid is calculated from the Nusselt number N_{Nu} for a spinning sphere, the diameter of the sphere D, and the temperature difference between the bulk slag and the surface of the sphere. The mass diffusivity D_m is taken from the data compiled for the diffusion of oxygen in liquid silicates (38). The melting range ΔT is taken from the range listed in Table IV-2. The rate of growth R is estimated from the calculated thickness of the slag shell shown in Figure VI-2 for the growth in the initial 5 seconds. Using these values the product of $G \cdot D_m$ is far less than the product of $\Delta T \cdot R$. This inequality indicates that the planar front solidification is not stable.

The growth of the solid slag slows as the sphere heats. At 10 to 15 seconds after immersion, the rate of growth is 0.009 cm/sec. This is still not low enough to give a stable planar interface according to Equation (3). Only when the rate of growth approaches zero and begins to reverse does the criterion indicate a stable planar boundary. If this criterion is accurate, a planar boundary is unlikely in the present slag system.

VI.B.3. Comparisons of the Experimental and Calculated Heating Curves for Various Slag Compositions

The heating curves from the experiments using liquid slag N-FA and N-FB at 1250°C are shown in Figure VI-3. A 3 cm. spinning nickel sphere was used in both experiments. Also the heating curves which are calculated from the mathematical model with a planar boundary condition are shown. The mathematics and the properties of the materials used for these calculated curves are described in Chapter V. The agreement between the experimental heating curve for slag N-FA and the calculated heating curve is good. The calculated curve deviates from the experimental curve only in the final state of heating. In the case of slag N-FB, the agreement is not so good.

Since slag N-FB is almost entirely composed of Fe_2SiO_4, it is possible that the slag solidifies at 1205°C, the melting temperature of iron saturated Fe_2SiO_4. The comparison between the experimental heating curves and the calculated heating curves using 1205° as the solidus instead of 1170° is shown in Figure VI-4. The two experimental heating curves are for a 1.8 and a 3.0 cm. spinning nickel sphere in slag N-FB at 1250°C.

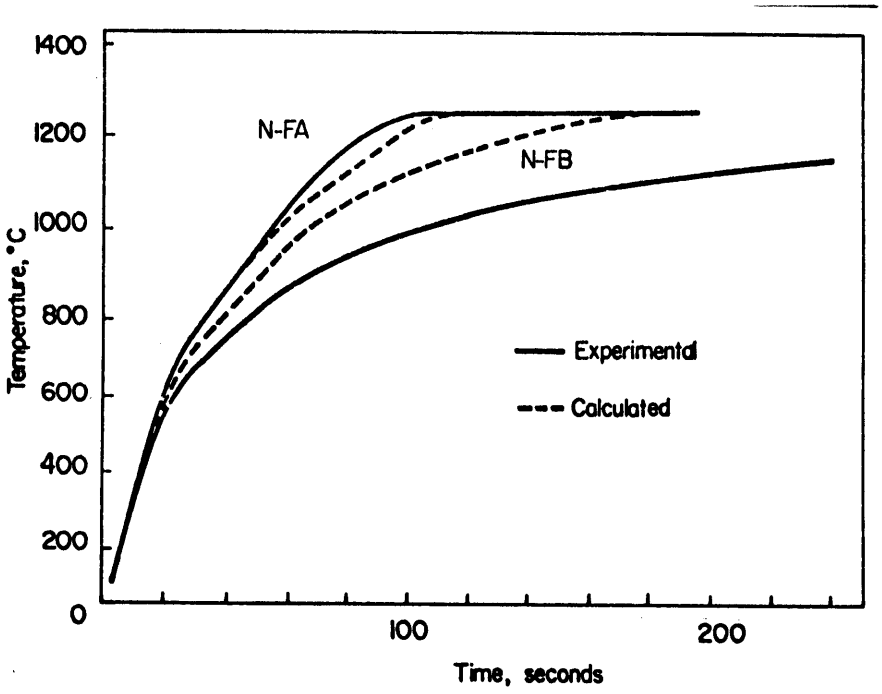

Figure VI-3 Comparison between the experimental and calculated heating curves using a planar boundary condition. Experimental conditions in Figure IV-7.

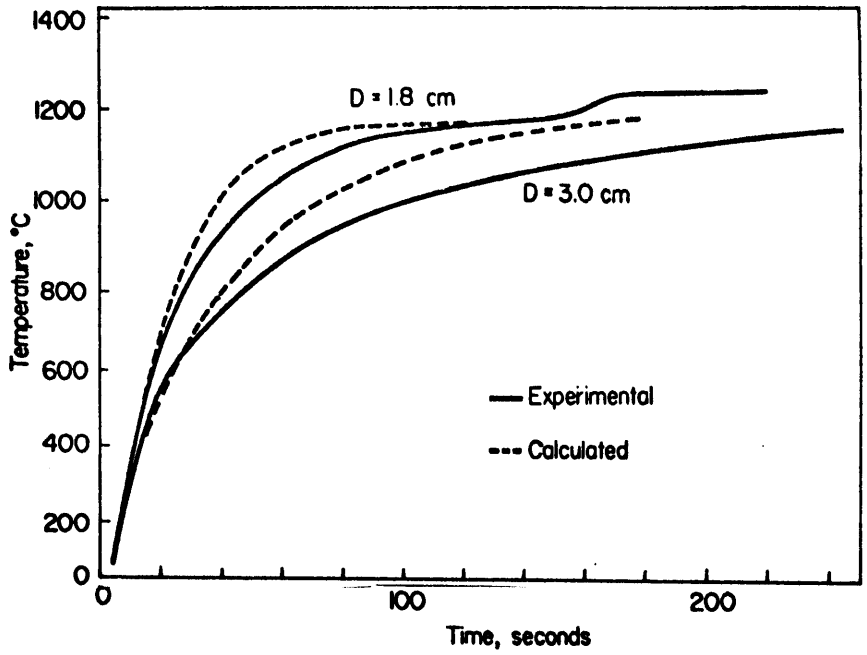

Figure VI-4 Comparison between the experimental and calculated heating curves using a planar boundary condition at the melting point of fayalite 1205°C. Experimental conditions in Figure IV-21

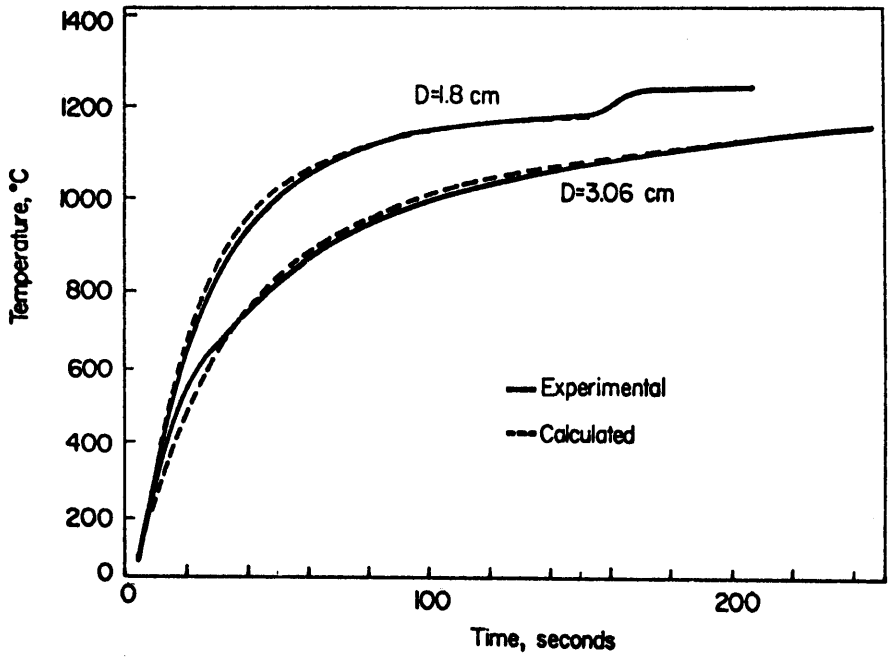

Figure VI-5 Comparison between the experimental and calculated heating curves using a mushy boundary condition with a melting range 1170-1240°C. Experimental conditions in Figure IV-21

The agreement between the calculated and the experimental curves is still poor. Apparently, the planar boundary condition does not describe the heating of a sphere in this slag or the thermal properties for this slag (Section V.E.) are in error.

Using the mushy boundary condition as described in Section V.C.2 and a melting range of 1170° to 1240°C, the heating curves for the conditions in Figure VI-4 are calculated. The agreement between the calculated and experimental curves in this case is very good, as shown in Figure VI-5. The mushy boundary condition does agree with the heating of a sphere in this particular slag. Further evidence for a mushy or cellular boundary for slag N-FB was presented in Chapter IV. The surface of the solid shell for slag N-FB was covered with large protruding crystals as shown in Figure IV-10. The surface of most of the other slags was smooth. Also the slag shell for slag N-FB was softer than for the other slags when the sphere was removed from the liquid slag.

The comparisons between the experimental and calculated heating curves for the remaining slags under similar experimental conditions are shown in Figures VI-6 and VI-7. All of the calculated curves in these figures are based upon the properties of material given in Chapters IV and V, and the planar boundary condition. The agreement for the slags N-FC, N-1CU, N-2CU, and N-IR is reasonably good. For slags N-CA, N-1A, and N-2A, the calculated heating curves are considerably below the experimental curves. Since a mushy boundary condition would further lower the heating curves, there must be another explanation for these disagreements. Either the thermal conductivity of the solid shell

is greater than expected, or the temperature at the solid-liquid interface is lower. These explanations will be discussed in Sections VI.B.3. and VI.C.

From the comparisons of the experimental and the calculated heating curves, it appears that there is a planar solid-liquid interface during the heating of the cold metal sphere in all but slag N-FB. This planar interface is in direct contradiction to the stability criterion discussed in Section VI.B.2. The planar interface may form when the mushy region is sheared away by the motion of the liquid slag, because the only fact that distinguishes slag N-FB from the other slags is that it is composed of over 97% Fe_2SiO_4. Almost pure fayalite precipitates during the solidification of this slag. This single phase solidification suggests that the strength of the large fayalite crystals in the mushy zone may explain the existence of the mushy region. If the shear produced by the spinning sphere is sufficient, the mushy region may be sheared away. The large fayalite crystals which constitute the mushy region of slag N-FB in Figures IV-8 and 10 may survive the shear while the smaller crystals in the other slags do not.

VI.B.4. The Calculated Effects of the Solidus Fraction

If the solidification and melting of the slag proceeds with a planar interface, then the temperature at this interface is a critical variable for the heating of the sphere. The comparisons between the experimental and calculated heating curves indicate that this temperature is usually the solidus temperature of the slag, T_S. The calculated effect of the solidus

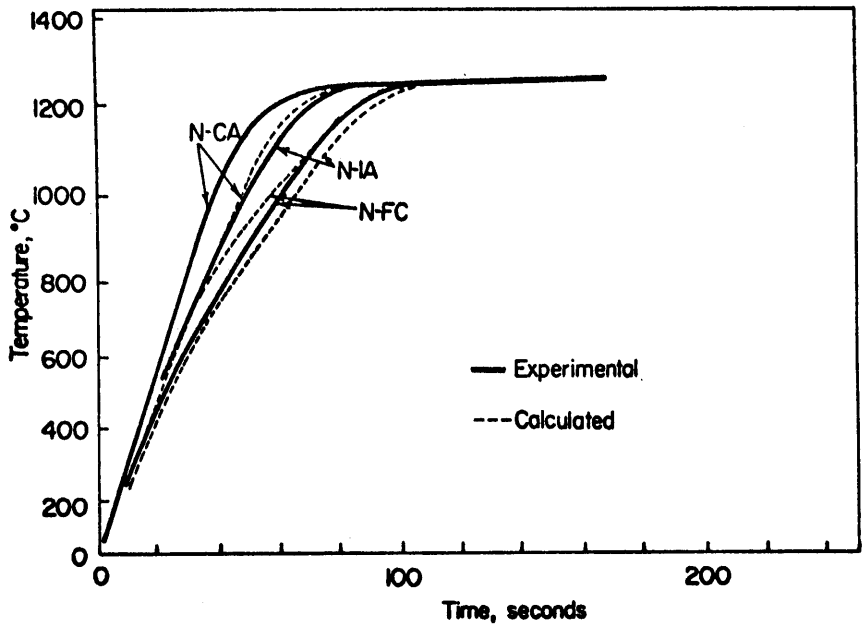

Figure VI-6 Comparison between the experimental and calculated heating curves using a planar boundary condition for slags N-FC, N-CA, and N-1A. Experimental conditions in Figure IV-8

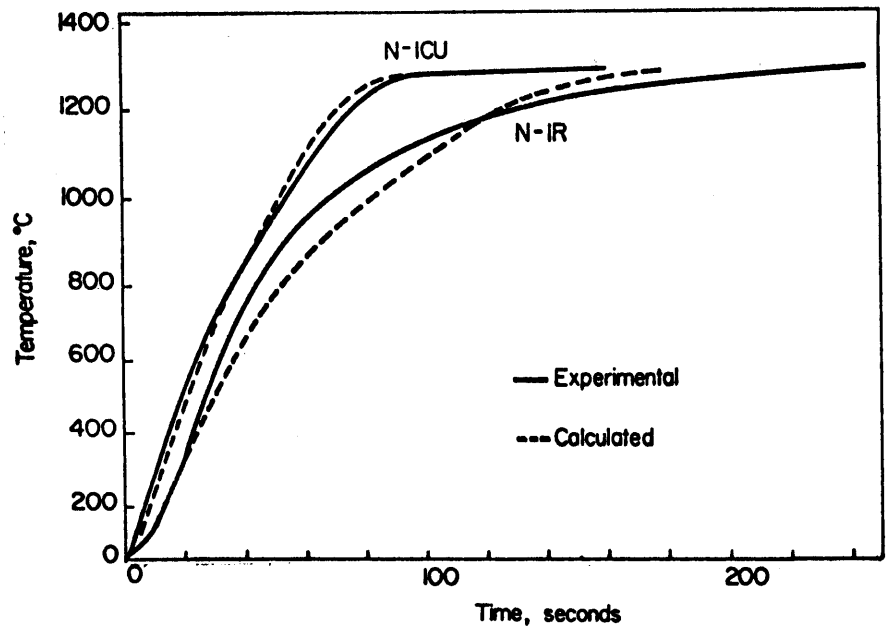

Figure VI-7 Comparison between the experimental and calculated heating curves using a planar boundary conditions for slags N-1CU and N-1R. Experimental conditions in Figure IV-6

fraction $\frac{T_S-T_O}{T_\infty-T_O}$ on the heating curve is shown in Figure VI-8. In this figure the calculated heating curves for the surface of a sphere immersed in a slag are plotted using the dimensionless variable described in Section V.G. The dimensionless temperature at the surface of the sphere, $\frac{T-T_O}{T_\infty-T_O}$ is shown as a function of the dimensionless time $\frac{\alpha_s t}{D^2}$ at various solidus fractions.

The effect of the solidus fraction on the calculated heating curve is shown by the relative positions of the curves in Figure VI-8. The effect is especially great in the range of solidus fraction from 0.7 to 0.95. In the present study the solidus fraction ranges from 0.8 to 0.95 as calculated from the solidus temperatures which are listed in Table IV-2 and the experimental conditions which are listed in Table III-2.

The solidus fraction is decreased either by lowering the solidus temperature of the slag or by increasing the temperature of the liquid slag. When either alumina or lime is added to slag N-FC, the solidus temperature is decreased. This decrease is indicated by the melting ranges measured by the DTA. The addition of either alumina (slags N-1A and N-2A) or lime (slag N-CA)to slag raises the experimental heating curve as shown in Figure VI-6. The effect of increasing the liquid slag temperature is shown in the heating curves presented in Figures VI-12 through 17. As the liquid temperature increases, the solidus fraction decreases and the shape of the heating curves changes according to the shapes shown in the calculated heating curves in Figure VI-8.

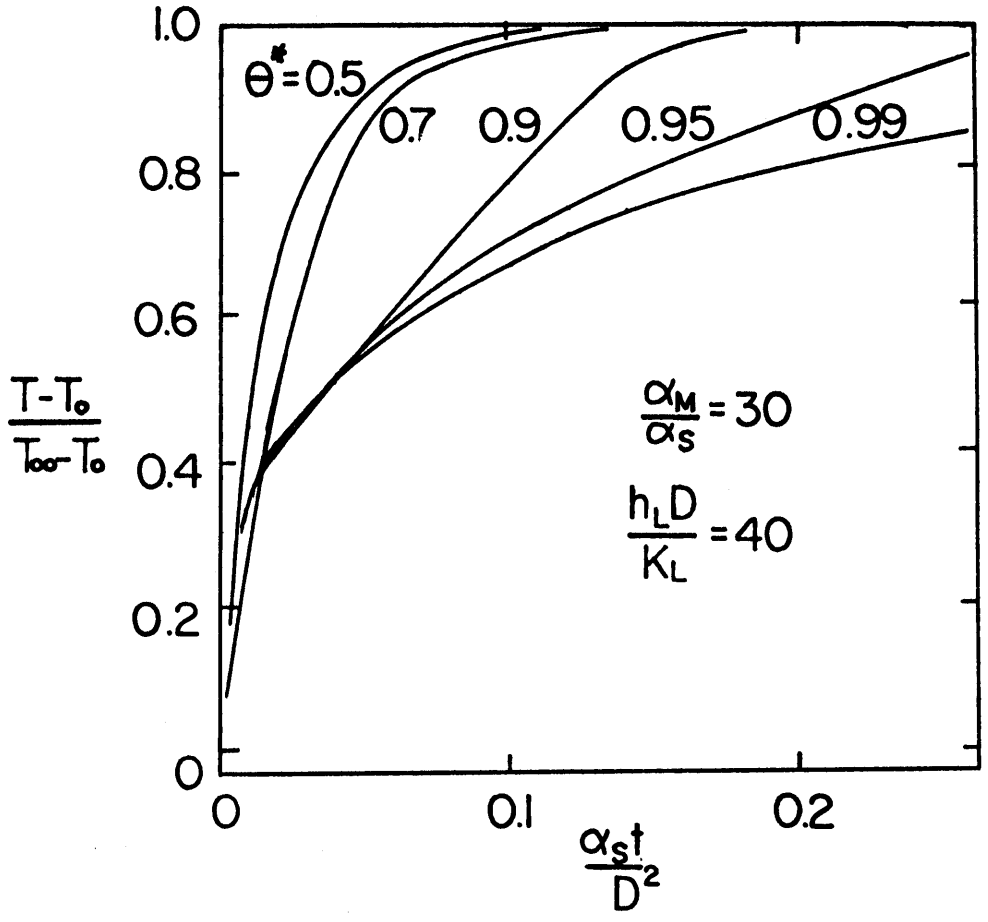

Figure VI-8 Calculated effect of solidus fraction θ^* on the heating of the surface of a metal sphere

The sensitivity of the heating curve to the solidus fraction may explain some of the disagreement between the experimental and the calculated curves for slags N-1A, N-2A, and N-CA, in Figure VI-6. If the solidus temperature which is used in the mathematical model is incorrect, neither the shape nor the position of the calculated heating curve will agree with the experimental curve. The positions and shapes of several experimental and calculated heating curves for slag N-1A are compared in Figure VI-9. The shapes of the experimental and calculated curves agree at 1260° and 1205°, but the positions do not. At 1160° neither the shape nor the position of the heating curves agree. The shape of the calculated curve at 1160° is more like that of the experimental curve at 1140°. According to the shape of the calculated dimensionless heating curves in Figure VI-8, the solidus fraction of the experimental heating curve at 1160° is about 0.9. The solidus temperature for the calculated curve at 1160° is 0.93, based on the solidus temperature 1070 which was determined by DTA. If the solidus temperature of this slag is reduced by 30° in the mathematical model, the solidus fraction would be 0.9. The lower solidus would bring the shape of the calculated curve into agreement with the experimental curve at 1160° and would improve the agreement in the position of the curves at all temperatures.

Since the melting range is measured by DTA, it is difficult to justify the lower solidus temperature. There may be some error in the determination of the solidus when the melting range is so great, but not 30°. It is also possible that there was substantial undercooling at the interface, but undercooling during both solidification and melting

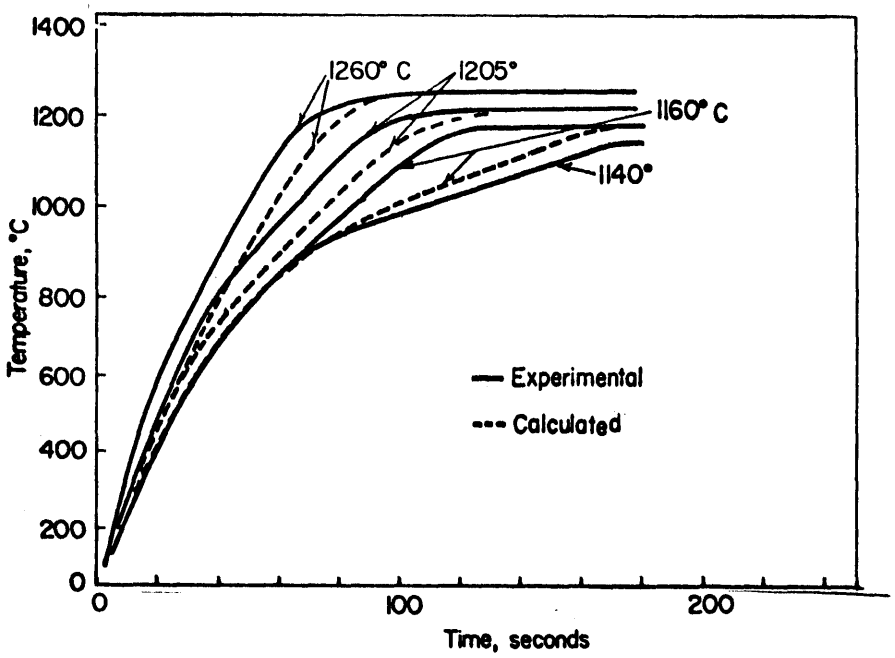

Figure VI-9 Comparison between the experimental and calculated heating curves for slag N-2A at liquid at various liquid bath temperatures. Experimental conditions in Figure IV-17

is unrealistic. Still, there is a good indication that part of the disagreement between the experimental and calculated curves for this slag is due to a lower solidus temperature. There are also good indications that part of the disagreement is due to the increased thermal conductivity of the solid slag shell. This explanation is discussed in the following section.

VI.C. Heat Transfer in the Solid Slag

Heat flow through the solid slag shell is critical in the present experimental arrangement. This solid shell forms an insulating layer which affects the heat flow to the metal sphere. The effect of the thermal diffusivity of this solid slag shell on the heating curves was shown earlier in Figure VI-8. In this figure the calculated temperature at the surface of the sphere was plotted as a function of the dimensionless time, $\frac{\alpha_s t}{D^2}$, where α_s is the thermal diffusivity of the solid slag. Doubling the thermal diffusivity of the solid slag would halve the time needed for the sphere to reach a particular temperature. The structure of the solidified shell and the properties of this shell are important in explaining the occurrence of a planar solid-liquid interface and the higher than expected heating curves for slags N-1A, N-2A, and N-CA.

The structure of the solidified silicate slag depends on mass diffusion, nucleation, radius of the curvature, crystallography, and the temperature distribution. Some of the possible structures for the solid-liquid interface of a ferrous silicate N-FA are shown in Figure VI-10. The structure in Figure VI-10a occurs with a nearly planar interface of

wustite and fayalite in region I. The structure is oriented in the direction of the heat flow. This structure requires limited convection in the liquid, a slow rate of growth, and a steep temperature gradient in the liquid (see Section V.C.).

Under less ideal conditions the structure for slag N-FA is shown in Figure VI-10b. There is a large mushy zone in region I, which is composed of wustite and fayalite crystals surrounded by a liquid which is depleted in FeO and Fe_2SiO_4. This structure eventually solidifies completely in region II. In Figure VI-10_c the mixing of the liquid shears many of the unsupported crystals in the mushy region I. These solid fragments of slag may either form new nucleation sites for further growth or be carried away into the bulk of the liquid slag. All three solidified structures shown are oriented in the direction of the heat flow, as were the slags in the present study (Figures IV-10, and 11).

The shearing of the mushy region in Figure V-10c suggests that a planar interface is possible even if the mushy interface is favored according to the criterion discussed in Section VI-B. This may explain why the heating curves which were calculated by the model using a planar boundary condition agreed so well with all the experimental curves except those with slag N-FB. The large crystals of fayalite with slag N-FB may not have been sheared when the sphere was spinning, and the mushy region remained. The smaller crystals in the mushy zone of the other slags may have been sheared away, and the interface was planar.

VI.C.1. The Effects of Orientation

In Figure VI-10 the crystals of the solidified slag shell are oriented

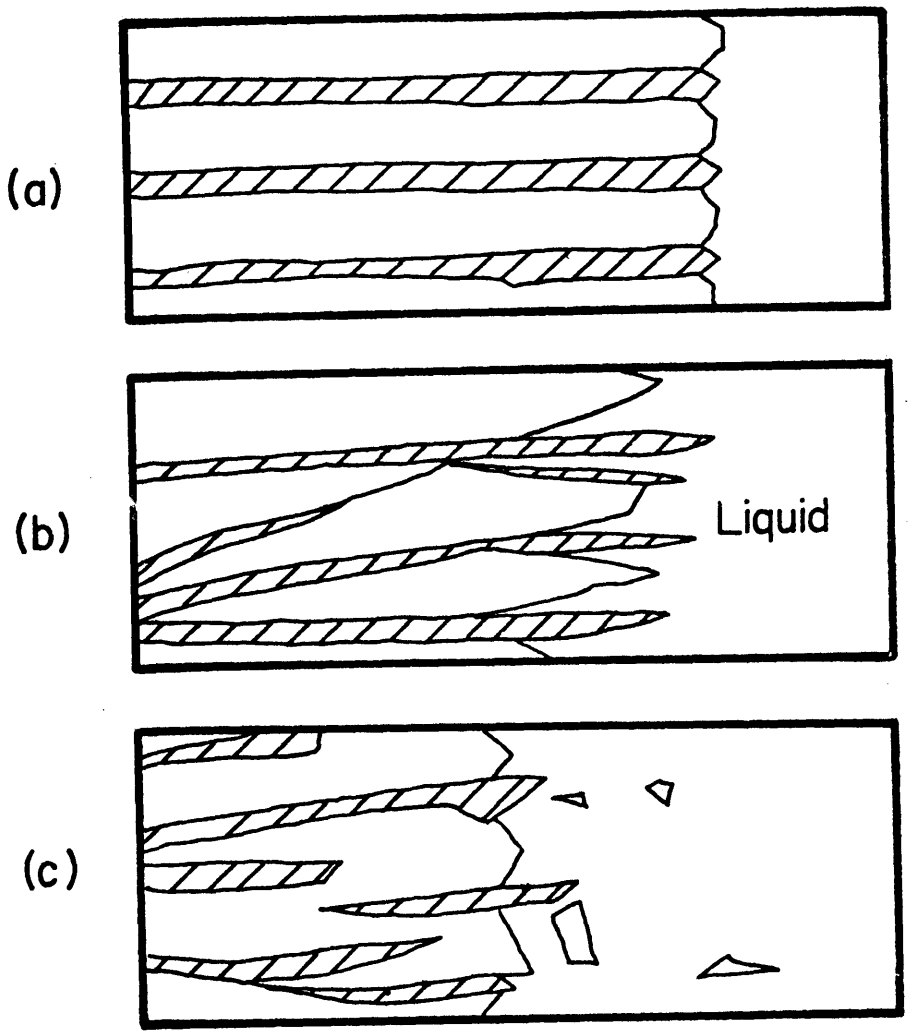

Figure VI-10 Solid-liquid interface structures

in the direction of heat flow. This orientation is predominantly observed in slags N-CA, N-1A, N-2A, and N-FA, and to some degree in all of the other slags, as shown in the micrographs, in Figures IV-10 and 11.

The thermal conductivity of a multiphase solid depends to some degree on the orientation of the crystals. Some simple two-phase solid structures are shown in Figure VI-11. The cellular structure in Figure VI-11a may conduct heat in a direction parallel or perpendicular to the cells. At a steady state heat flow perpendicular to the cells, the thermal conductivity is represented by the equation for conductivity of layers (67).

$$K_s = \frac{K_1 K_2}{\phi_1 K_2 + \phi_2 K_1} \qquad (4)$$

where K_1 and K_2 are the thermal conductivity of the two phases present, and ϕ_1 and ϕ_2 are their volume fractions. The thermal conductivity which is calculated from this equation is demonstrated as a function of volume fraction in the lowest curve in Figure VI-12. If the heat flow is parallel to the cells in Figure VI-11a, the thermal conductivity is represented by Equation (5) (67).

$$K_s = \phi_1 K_1 + \phi_2 K_2 \qquad (5)$$

as demonstrated by the upper curve in Figure VI-12. The orientation of the cells in the direction of the heat flow may greatly increase the thermal conductivity of the solid, if there is a large difference between the thermal conductivity of the separate phases.

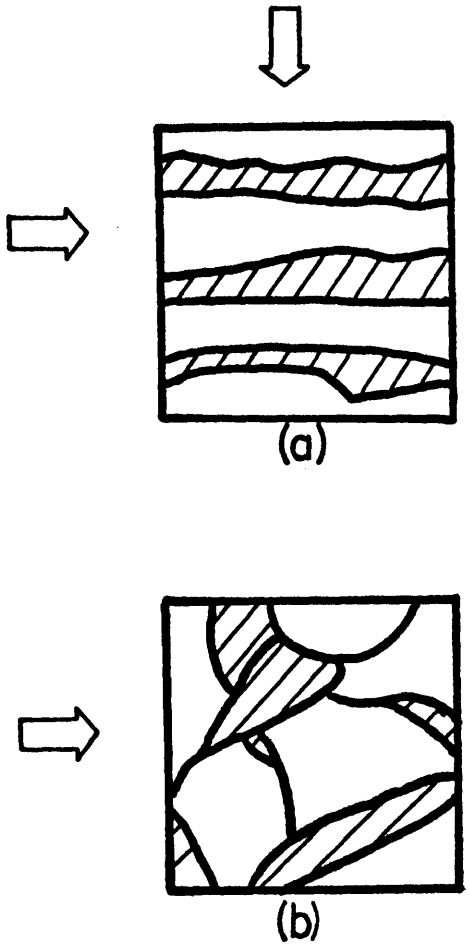

Figure VI-11 Heat flow in cellular and mixed structures

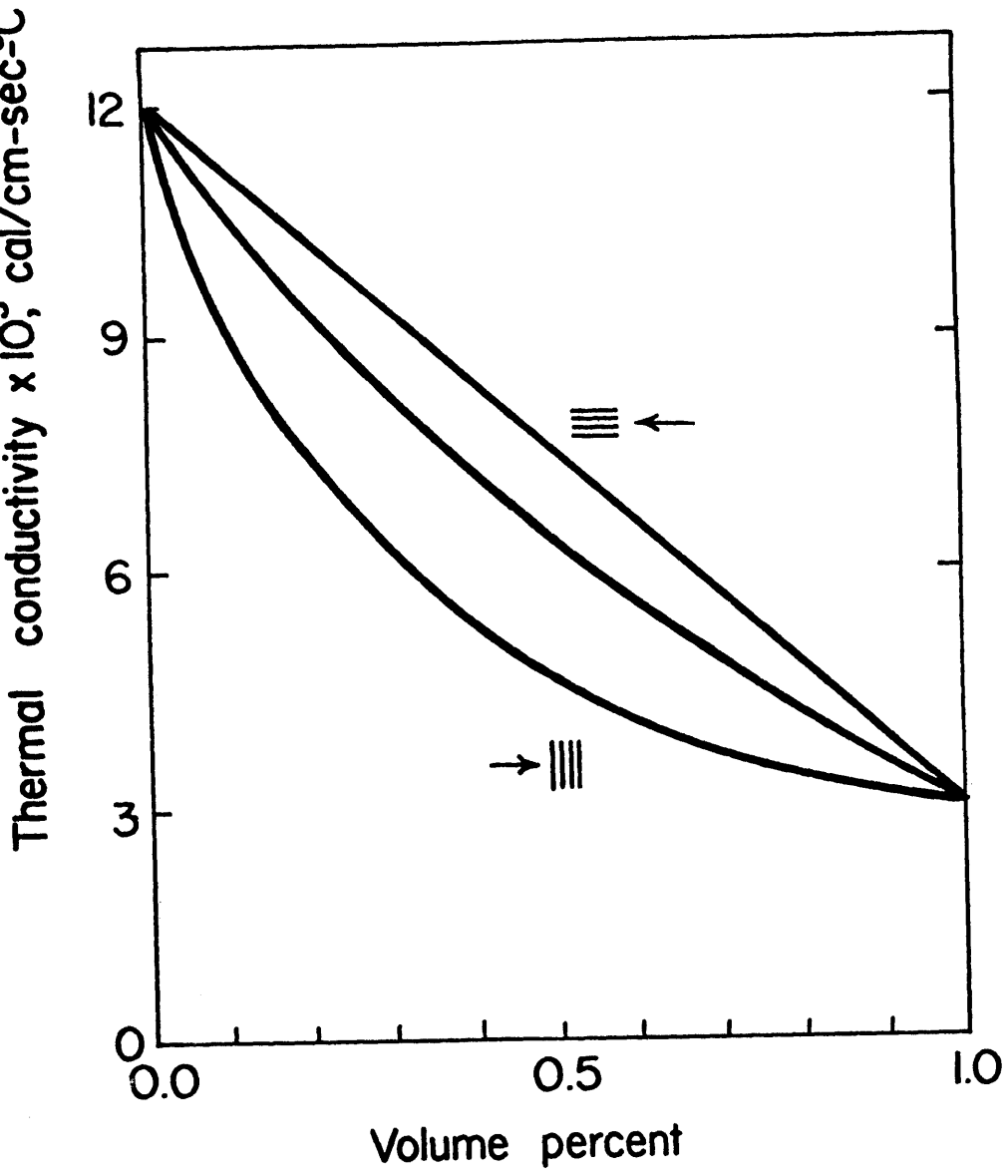

Figure VI-12 Calculated thermal conductivity as a function of volume fraction

For mixed structures such as shown in Figure VI-11b, the value of thermal conductivity is intermediate between the thermal conductivity of oriented structures as shown in Figure VI-12. For a homogeneous multiple phase solid the thermal conductivity can be estimated by the geometric mean (43)

$$K_s = K_1^{\phi_1} K_2^{\phi_2} \qquad (6)$$

The thermal conductivity of the solid slag can be increased substantially when the crystals are oriented in the direction of the heat flow, such as in the present solidified slag shell. This increased thermal conductivity may partially explain the higher than expected heating curves for slags N-CA, N-1A, and N-2A, as shown in Figure VI-6. All these slags formed highly oriented solid structures.

VI.C.2. The Effects of Porosity on the Thermal Conductivity

All the slag shells formed in the present study have some degree of porosity. For the experiments conducted with bubble stirring, the porosity is 0.12 to 0.15, while for the other conditions the porosity is less than 3%. The effect of such porosity on the thermal conductivity of the solid slag is calculated in this section.

Porosity can increase or decrease the conductivity of a material. In the case of small homogeneous prosity, the geometric mean of the conductivities can be used to approximate the thermal conductivity

$$K_s = K_p^{\psi} K^{(1-\psi)} \qquad (7)$$

where ψ is the pore fraction, K and K_p are the thermal conductivities of

the non porous solid and the gas pores, respectively. This equation has been successfully used to calculate the thermal conductivity of porous metals and oxides (47, 48). The thermal conductivity of the pores which are filled with air is represented by equation (8) which combines the conduction and the radiation contributions (see Section V.F.).

$$K_p = 3.04 \times 10^{-4} [1-\exp(-7.65 \times 10^{-4}T)] + 3\sigma T^3 d \text{ (cal/cm sec°K)} \quad (8)$$

where T is the temperature of the pore, σ is the Stephan-Boltzman constant, and d is the diameter of the pore.

The effects of porosity, pore size and temperature on the thermal conductivity of a porous slag are calculated and shown in Figure VI-13. In this figure the thermal conductivity of the slag is plotted as a function of temperature at various pore fractions and pore diameters, as calculated from Equations (7) and (8). The hypothetical thermal conductivity of the non-porous slag is represented by the uppermost curve in this figure. The thermal conductivity of this solid slag with 0.03 and 0.15 pore fraction at various pore sizes is shown beneath this curve. Porosity lowers the thermal conductivity in all the cases shown. Only extremely large pores at a low porosity could increase the thermal conductivity of a slag.

Based on the calculated effects of porosity on the slag, the thermal conductivity of the solid slag during gas bubble stirring should be substantially lower. This lower conductivity lowers the heating curve of the metal sphere as will be discussed in Section VI.D.2.

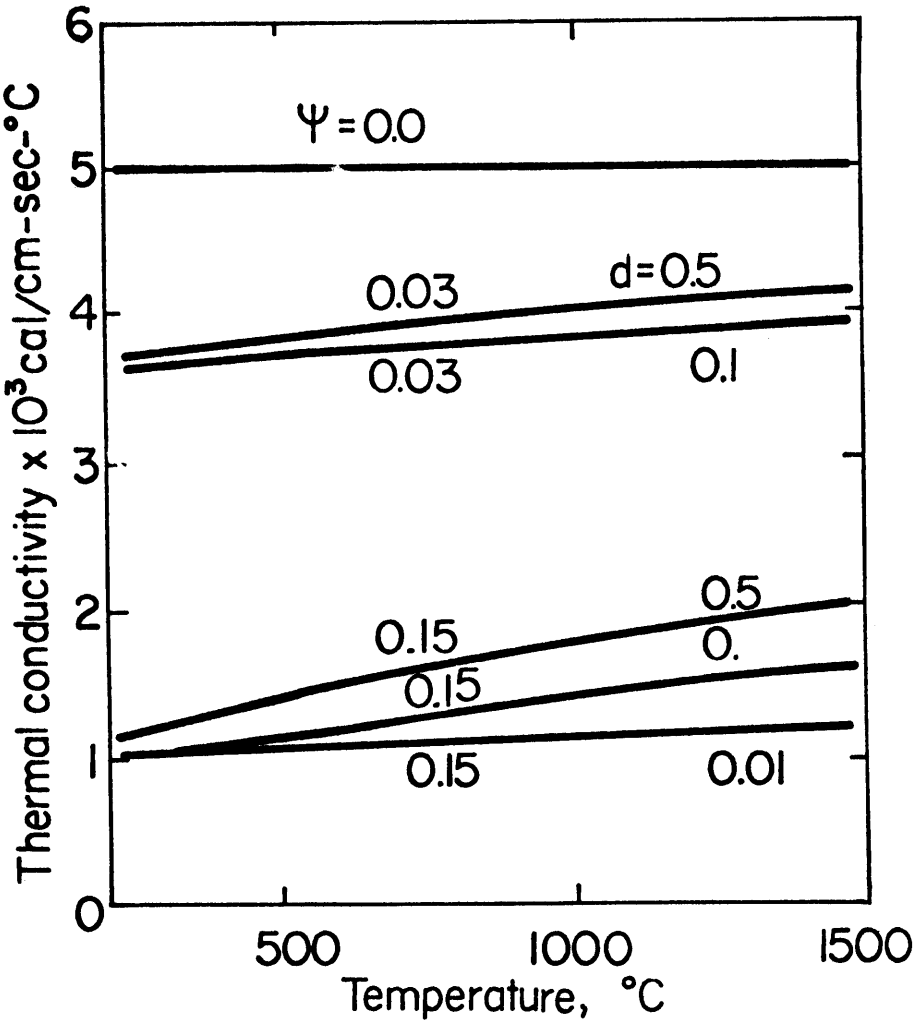

Figure VI-13 Calculated thermal conductivity of porous slag at various values of porosity ψ and pore size d

VI.D. Convective Heat Transfer in the Liquid Slag

Aside from the transfer of heat in the solid slag shell, the transfer of heat in the liquid boundary layer in the slag is very critical for the heating of the metal sphere. In this section the effects of the heat transfer coefficient for the liquid boundary layer are presented and calculated and experimental heating curves for the various conditions of fluid flow are compared. The effects of radiation and the non-steady temperature distribution in the liquid are also discussed.

VI.D.1. The Calculated Effects of the Heat Transfer Coefficient

The liquid heat transfer coefficient h_L is related to the Nusselt number, N_{Nu} by the definition

$$N_{Nu} = \frac{h_L D}{K_L} \tag{9}$$

where D is the diameter of the sphere, and K_L is the thermal conductivity of the liquid slag. The calculated Nusselt number for the present experimental conditions range from 2 in the case of natural convection to 70 in the case of rapid gas bubbling.

The calculated effects of the heat transfer coefficient in terms of the Nusselt number on the temperature at the surface of an immersed sphere is shown in Figures VI-14 and VI-15. These dimensionless heating curves are calculated from the mathematical model described in Chapter V which uses the planar boundary condition for solidification and melting. In Figure VI-14 the solidus fraction $\frac{T_s - T_o}{T_\infty - T_o}$ is 0.8 for the calculations, while in Figure VI-15 the solidus fraction is 0.95.

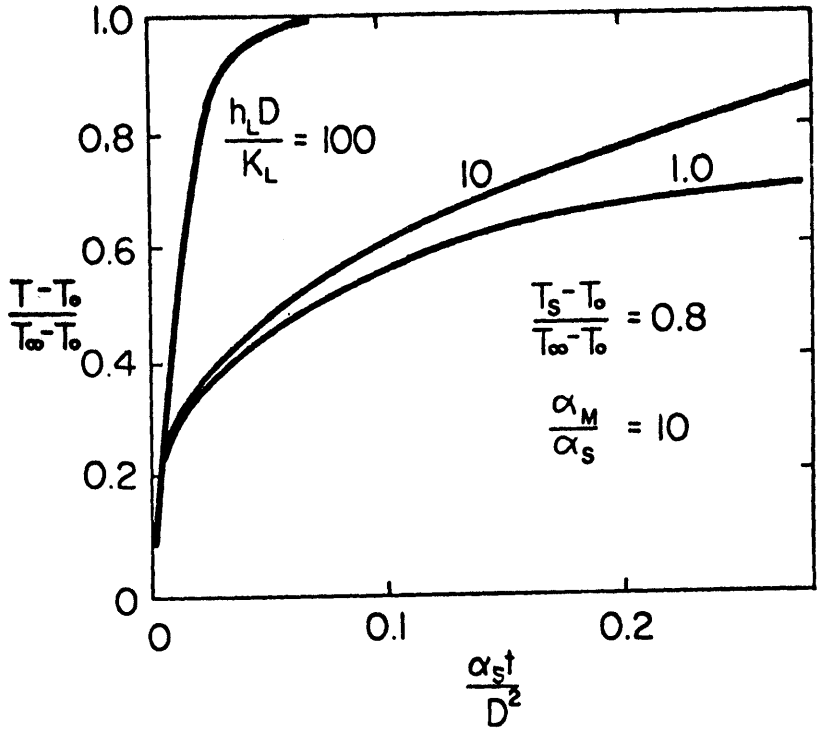

Figure VI-14 Calculated effects of the heat transfer coefficient or Nusselt number on the heating of the metal sphere. Solidus fraction 0.8

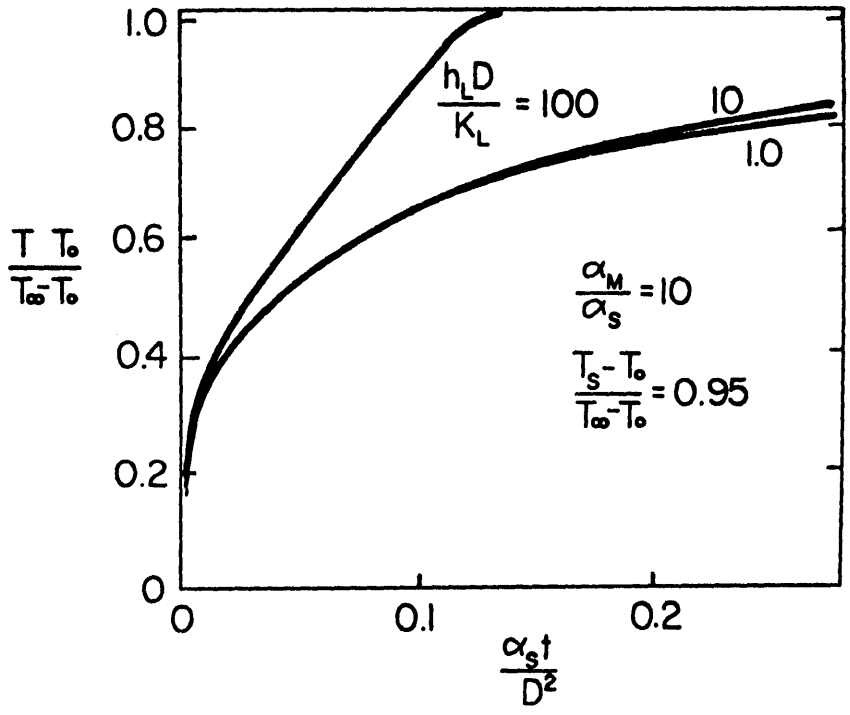

Figure VI-15 Calculated effects of the heat transfer coefficient or Nusselt number on the heating of the metal sphere. Solidus fraction 0.95

If the solidus fraction is 0.8, then the heat transfer coefficient h_L in terms of the Nusselt number has a tremendous effect upon the heating curve of a sphere. As shown in Figure VI.14 an increase in the Nusselt number from 10 to 100 reduces the time required for the surface of the sphere to reach a particular temperature by more than 80%.

For a solidus fraction of 0.95 the effect of the heat transfer coefficient is greatly reduced, as shown by a comparison of Figures VI-14 and VI-15. The calculated time for the surface of a sphere to reach a particular temperature is reduced by only about 50% if the Nusselt number is increased from 10 to 100. An increase of the Nusselt number from 1 to 10 has almost no effect.

The effect of the solidus fraction on the heating curves in these two figures can be simply explained. The heat transfer coefficient h_L represents the conductance of the boundary layer in the liquid, while the driving force is the difference of the temperature in the bulk liquid and at the solid-liquid interface. When the solidus fraction becomes larger this temperature difference becomes smaller. Thus, the heat flux in the boundary layer is a function of the heat transfer coefficient and the solidus fraction, which can be written

$$Q^*_{BL} = \frac{h_L D}{K_L} [1-\theta^*] \qquad (10)$$

The magnitude of each of these variables modifies the effect of the other variable on the flux of heat in the boundary layer.

The interdependence of the heat transfer coefficient and the solidus

fraction explains why some some experimental heating curves are so sensitive to spinning of the sphere. For the experimental heating curves shown in Figure IV-2 with slag N-IR the solidus fraction is calculated from the solidus measured by the DTA to be 0.93. The difference between the heating curve of the static sphere and the spinning sphere is only moderate in this figure. For the same slag in Figure IV-1 the solidus fraction is 0.90 and the resulting difference between the heating curves of the static sphere and the spinning sphere is slightly greater. Slight changes in the solidus fraction modify the effects of the convection heat transfer in the liquid.

VI.D.2. Comparison of Experimental and Calculated Heating Curves for Spinning and Bubble Stirring

A comparison between the experimental and calculated heating curves for a spinning nickel sphere and a spinning nickel cylinder is shown in Figure VI-16. The calculated heating curves are based on the planar boundary condition and the Nusselt number described in Section V.D. The agreement between the calculated and experimental heating curves is very good. This comparison demonstrates that the Nusselt numbers described in Section V.D. for a spinning sphere and a spinning cylinder are appropriate. The comparison also indicates that the effect of increasing the surface area of the metal object on the heating of the object through a change in shape is predicted by the model.

A comparison between the experimental and calculated heating curves for a variety of fluid flow conditions is shown in Figure VI-17 and VI-18. The Nusselt numbers for the various spinning, bubbling, and static con-

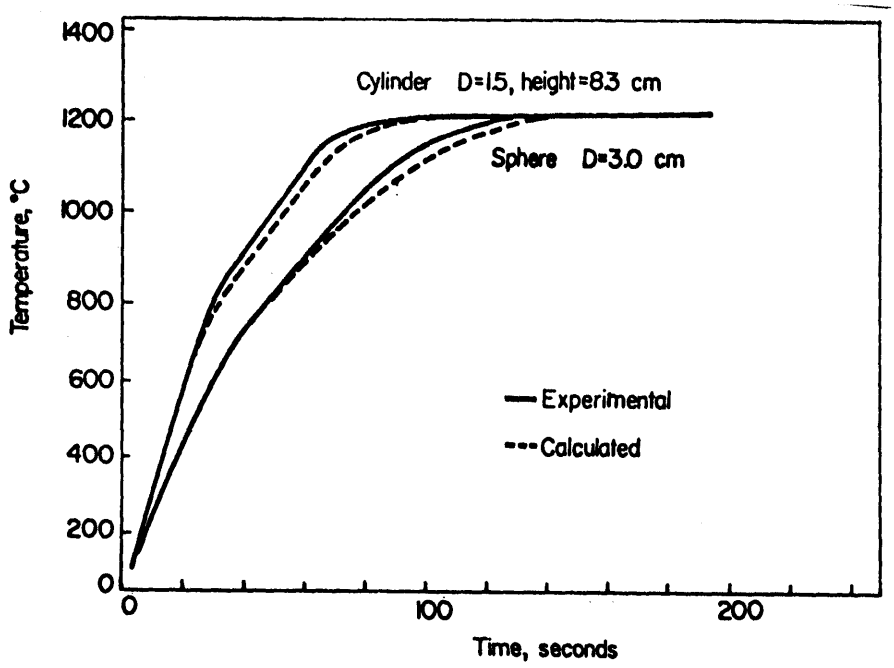

Figure VI-16 Comparison between the experimental and calculated heating curves for a nickel cylinder and a nickel sphere. Experimental conditions in Figure IV-22

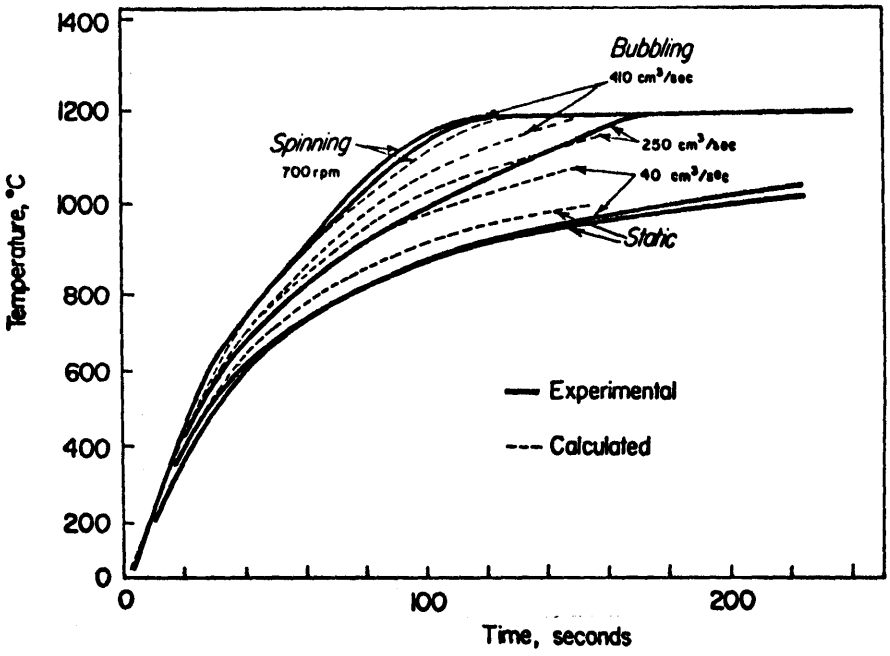

Figure VI-17 Comparison between the experimental and calculated heating curves at various thpes of convection. Calculated heating curves for bubbling are based on power dissipation by the rising bubbles (see Section V.D.3). Experimental conditions in Figure IV-5

ditions are discussed in Section V.D. The values of these Nusselt numbers are listed in Table V-1.

For a static sphere the agreement between the experimental and calculated heating curve is reasonably good. The mathematical model for this heating curve uses a planar boundary condition, but in this case of poor convection, a mushy boundary condition may be more appropriate. If the heating curve for the static nickel sphere is recalculated using the mushy boundary condition, the same calculated curve results. The moving boundary has little or no effect on the calculated heating of the sphere which is held static in the slag.

For forced convection by rising bubbles, there are two sets of calculated heating curves shown is Figures VI-17 and VI-18 for the two sets of Nusselt Numbers shown in Table V-1. The calculated heating curves in Figure VI-17 are based on power dissipation by the rising bubbles. The agreement between the experimental and calculated curves is only fair. The calculated curves in Figure IV-18 are based on the velocity of the rising liquid slag which is drawn upward by the rising bubbles. The agreement between the experimental and calculated heating curves is not good. Of the two sets of calculated heating curves the set based on power dissipation fits better with the experimental curves.

At a gas flow rate of 40 ml/sec both of the calculated heating curves are far above the experimental curve, but the curve based on power dissipation is the closer. The solid-liquid interface in this case may not be smooth or planar as suggested by the comparison of curves for the spinning sphere. If a mushy boundary condition is used in the mathematical

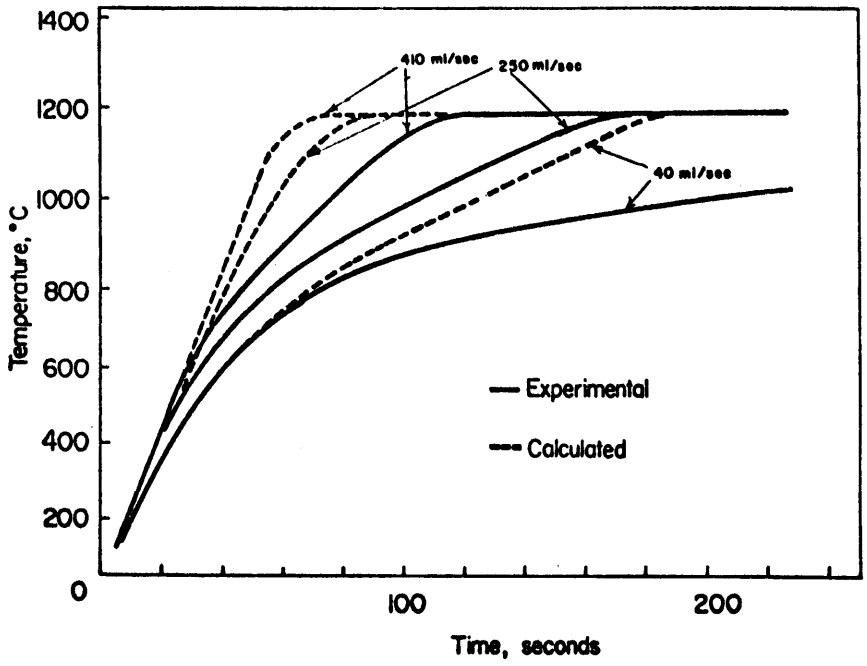

Figure VI-18 Comparison between the experimental and calculated heating curves at various gas bubbling rates. Calculated heating curves are based on the velocity of the rising slag (see Section V.D.3). Experimental conditions in Figure IV-5

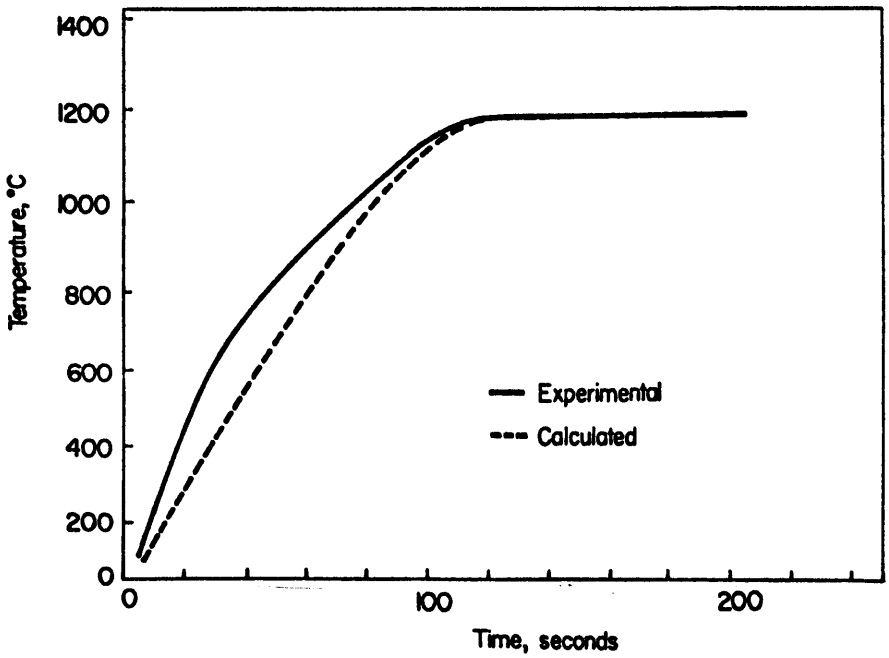

Figure VI-19 Comparison between the experimental and calculated heating curves for a gas bubbling rate of 410 ml/sec. Calculated heating curve for bubbling is based on the velocity of the rising slag and a porosity in the solid and liquid slag of 0.15

model, the calculated heating curves for both Nusselt numbers are lowered and the agreement is greatly improved. At this rate of bubble mixing a planar interface may not be formed, and a mushy interface may control the heat flux from the liquid slag.

At the intermediate gas flow rate of 250 ml/sec, the effects of porosity of the solid and liquid slag should be considered in the comparisons. The pore fraction observed in the experiments at this gas flow rate was about 0.12. According to the calculations in section VI.C.3. this pore fraction should reduce the thermal conductivity of the slag from 0.0045 cal/cm^2-sec-$^\circ$C to about 0.003 cal/cm^2-sec-$^\circ$C. This thermal conductivity gives a thermal diffusivity for the porous slag of about 0.004 cm^2/sec. As shown in Figure VI-8, a decrease in the thermal diffusivity should displace the calculated heating curve proportionately to the right. This displacement of the calculated curve based on power dissipation (Figure VI-17) places the calculated curve below the experimental curve, but the agreement between the two curves is slightly improved. A similar displacement of the calculated curve based on the velocity of the rising slag improves the agreement between the curves in Figure VI-18, but not significantly.

At the highest gas flow rate of 410 ml/sec, the pore fraction was about 0.15 and the calculated thermal diffusivity from Section VI.C.3 is about 0.003 cm^2/sec. This reduced thermal diffusivity displaces the calculated heating curved based on power dissipation far away from the experimental curve. A similar displacement of the calculated heating curve based on the velocity of the rising slag brings the calculated

heating curve much closer to the experimental curve, as shown in Figure VI-19. Although the agreement between the calculated and experimental curves after 70 seconds of immersion is improved by this consideration of porosity, the agreement is poor during the initial times. The effects of porosity on the thermal conductivity are not apparent during the initial heating of the sphere. A close look at the photograph in Figure VI-20, does show that the porosity of the initial slag formed on the sphere is less than the porosity of the later slag.

Neither set of calculated Nusselt numbers fits all the experimental heating curves for bubble mixing. At the higher gas flow rates the porosity of the slag must be considered and the Nusselt number based on the rising slag gives the more reasonable heating curves. At the lower gas flow rates the Nusselt numbers based on power dissipation are slightly preferred.

VI.D.3. The Effect of a Non-Steady State Boundary Layer

For a liquid boundary layer to reach a steady state temperature distribution, the velocity distribution must be steady and some heat must be extracted from the liquid slag adjacent to the sphere. The velocity distribution is consistent around a spinning sphere. The time required for the spinning boundary layer to reach a steady state is short, but for natural convection or bubble stirring the time may be considerable. An effective Nusselt number may be substituted for the steady state Nusselt number when the boundary layer is in a non-steady state.

The effective Nusselt number for a non-steady state boundary layer is

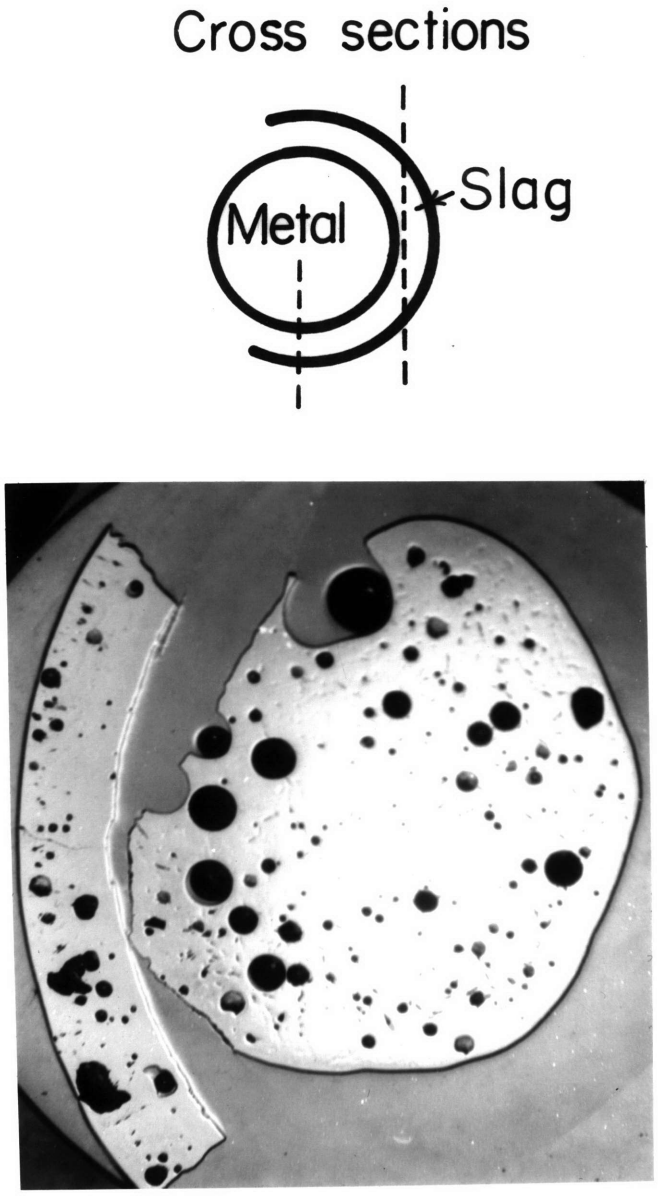

Figure VI-20 Pores in a slag shell sample after 50 seconds of immersion. Cross sections through the thickness and across the shell (4x)

calculated by solving the heat conduction equation in the boundary layer of the liquid. For a thin boundary layer the conduction equation is

$$\frac{\partial\left(\frac{T-T_s}{T_\infty-T_s}\right)}{\partial\left(\frac{t\alpha_L}{\delta}\right)} = \frac{\partial^2\left(\frac{T-T_s}{T_\infty-T_s}\right)}{\partial\left(\frac{x^2}{2}\right)} \qquad (11)$$

where T_s is the temperature at the solid surface

T_∞ is the temperature of the bulk liquid

α_L is the thermal diffusivity of the liquid

t is the time

x is the distance from the solid surface

δ is the thickness of the boundary layer in the liquid

This equation is solved for the boundary conditions in the boundary layer

$$T = T_o;\ x = 0$$

$$T = T_\infty;\ x = \delta$$

The boundary layer thickness is represented by the steady state Nusselt number N_{Nu} and the diameter of the sphere D (36)

$$\delta = \frac{D}{N_{Nu}} \qquad (12)$$

The initial conditions of the boundary layer are

$$T = T_\infty\ ;\quad x \geq 0$$

$$T = T_s\ ;\quad x = 0$$

The non-steady state Nusselt number, N_{Nu}^{eff} is defined as

$$N_{Nu}^{eff} = \left. \frac{d\left(\frac{T-T_s}{T_\infty - T_s}\right)}{d\left(\frac{x}{\delta}\right)} \right|_{x=0} \qquad (13)$$

Using finite difference equations, similar to those described in Section VI.A, the conduction equation is solved with the given boundary conditions. The solution gives the effective Nusselt number as a function of the time.

The effective Nusselt number is shown in Figure VI-21 as a function of the dimensionless time. The dimensionless time required for the effective Nusselt number to reach 10% of the steady state Nusselt number is about 6.0. For the spinning sphere at 700 rpm, this time is 4.5 seconds. The effective Nusselt number for natural convection in the present experiments should be about three or four times greater than the steady state value. This increase in the Nusselt number has little effect on the calculated heating curve for natural convection because the heat transfer from the solidified slag shell dominates the heating of the sphere. As discussed in Section VI.D.2, when the solid slag shell is present, the effects at the solid-liquid interface may be neglected for natural convection.

The effective Nusselt numbers for the boundary layers in bubble stirring are further complicated by the fluctuations in velocities in the boundary layer. These fluctuations in the velocity will extend the time necessary for the temperature distribution in the boundary layer to reach a steady state. Using a higher effective Nusselt number or heat

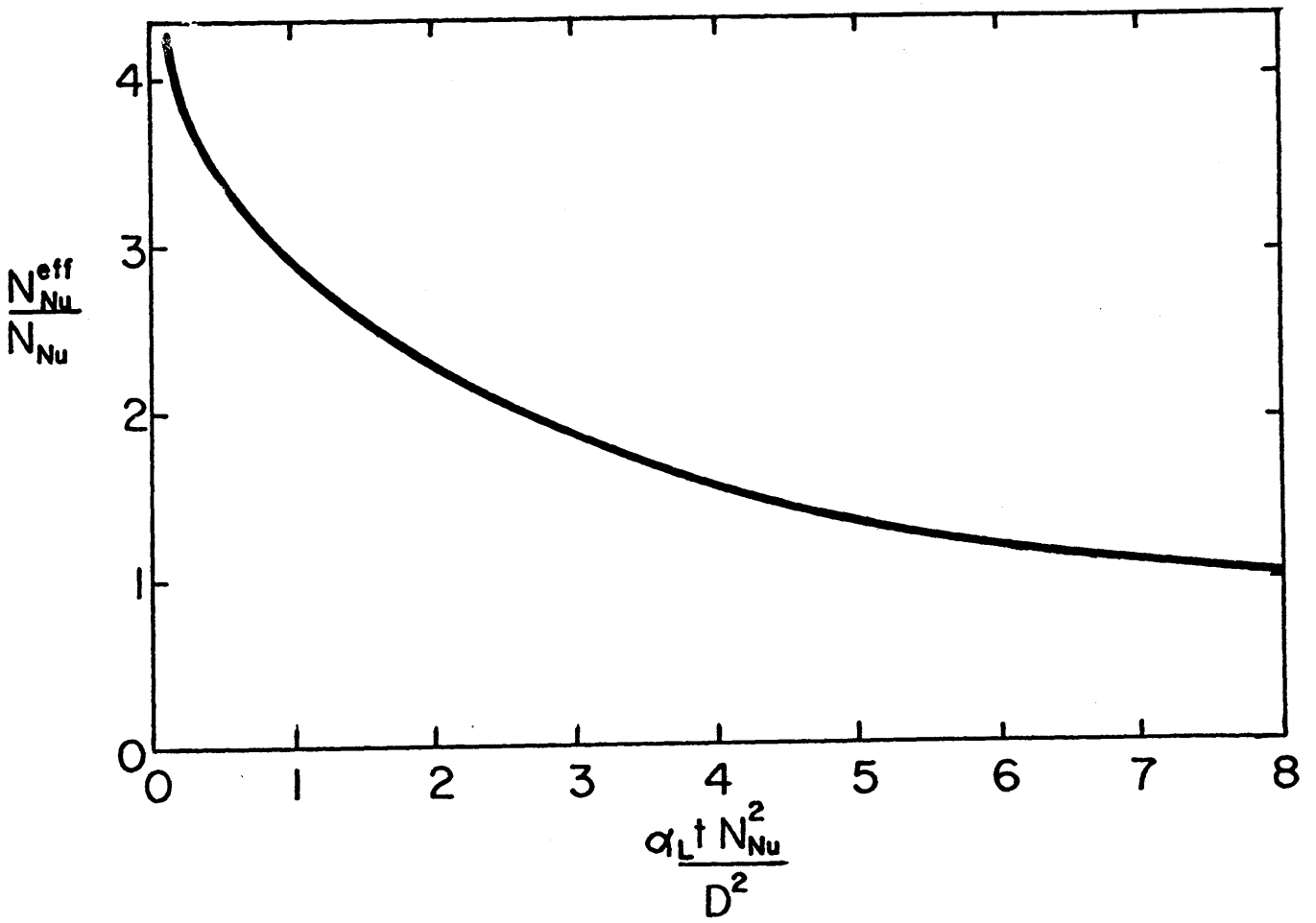

Figure VI-21 Effective Nusselt number for a non-steady state temperature distribution in the boundary layer

transfer coefficient for the calculated heating curves for bubble stirring improves the agreement of the calculated curves based on power dissipation with the experimental curves. The effective heat transfer coefficient only at the lower gas flow rates because, at the higher flow rates, the boundary layer is small.

VI.D.4. Radiation in the Boundary Layer

Radiation heat transfer through the boundary layer may contribute significantly to the heat transfer from the liquid. Fine, Enge and Elliott (3) suggested that the radiation contribution in the bulk liquid slag may be equal in magnitude to the conduction contribution for slags of less than 15% FeO. A detailed calculation of the radiation contribution to the heat flux in the boundary layer is discussed in Appendix E. This calculation gives the fraction of heat flux through the boundary layer by radiation, f_{rad}

$$f_{rad} = \frac{1}{1 + \frac{\lambda K_L}{2\sigma}\left(\frac{T_\infty - T_S}{T_\infty - T_S}\right)} \qquad (14)$$

where σ is the Stephan Boltzman constant

T_S is the temperature at the surface of the solid

T_∞ is the temperature of the bulk slag

λ is the bulk coefficient of absorption in the liquid

K_L is the thermal conductivity of the liquid slag

The radiation fraction f_{rad} is a function of the wavelength of the radiation emmitted and absorbed in the slag because the bulk coefficient

of absorption is a function of wavelength. For several concentrations of FeO this radiation fraction is calculated from Equation (14) and listed in Table VI-2. The bulk absorption coefficient for the low FeO slags is taken directly from the room temperature measurements of glasses by Fine, Enge, and Elliott (3) for a wavelength of 2.5 microns. At this wavelength the emissive power from Plank's radiation law for a black body is at a maximum for 1400°K (71). The bulk absorption coefficient for a 60% FeO ferrous silicate is extrapolated from the values at much lower FeO concentrations. The thermal conductivity of the liquid slag is assumed to be 0.003 cal/cm-sec-°C. The temperatures for the ferrous silicate are typical for the present experiments, while the temperatures for the low FeO slags are typical for steelmaking processes. For the present ferrous silicates the radiation contribution is very small, while for the low FeO slags this contribution may be quite significant.

VI.E. Heat Conduction in the Metal Sphere

VI.E.1. The Initial Temperature of the Sphere

A comparison between the experimental heating curves and the calculated heating curves for a nickel sphere immersed in slag N-1CU as three different initial temperatures of the sphere is shown in Figure VI-22. The agreement is good. A similar agreement between calculated and experimental curves is obtained in the other experiments in which the initial temperature of the sphere was varied. As observed in the experimental and calculated heating curves, the time required for the sphere to reach a particular temperature is greatly reduced by preheating the sphere. The effect of the initial temperature on the calculated

Table VI-2. Fraction of Radiation Heat Flux in a Boundary Layer

Slag	$\lambda(cm^{-1})$	T_∞ (°K)	T_o (°K)	f_{rad}
Ferrous-silicate	400	1500	1400	0.025
Low FeO (14.7%)	100	1873	1773	0.18
Very low FeO (7.1%)	60	1873	1773	0.29

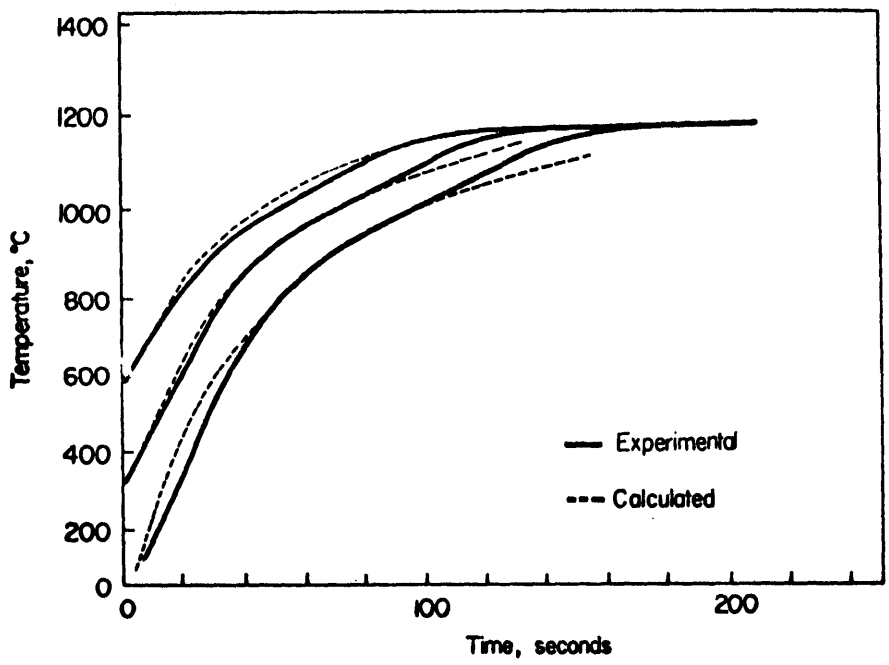

Figure VI-22 Comparison between the experimental and calculated heating curves for a nickel sphere of various initial temperatures. Experimental conditions in Figure IV-18

heating curves in Figure VI-8, 14, and 15 is included by the use of the initial temperature of the sphere T_o in the solidus fraction and the dimensionless temperature.

VI.E.2. The calculated effects of thermal diffusivity of the Sphere

The model with a planar boundary condition is used to calculate the heating of a metal sphere with various thermal diffusivities α_M. The calculated temperatures at the surface and the center of the metal sphere are shown in Figure VI-23, based on this model. The Nusselt number is 40 and the solidus fraction is 0.9 for this calculation. The thermal diffusivity ratio $\frac{\alpha_M}{\alpha_S}$ represent the transient conduction in the sphere relative to the conduction in the solid slag. The higher diffusivity ratio corresponds to a high thermal conducting metal like copper, while the low ratio corresponds to a very porous sphere, like the porous iron spheres used in some of the present experiments.

A decrease in the metal diffusivity increases the rate of heating at the surface of the metal sphere as shown in Figure VI-23. The temperature at the center of the sphere is reduced by a decrease in the thermal diffusivity of the metal, because the decreased thermal diffusivity decreases the heat flow into the center of the sphere and allows the temperature to build up at the surface of the sphere.

VI.E.3. Comparison of the Experimental and Calculated Heating Curves

As described in Section V.F., the thermal conductivity of the porous iron spheres is calculated in the mathematical model using the geometric mean of the conductivities of the iron and gas that are present. A com-

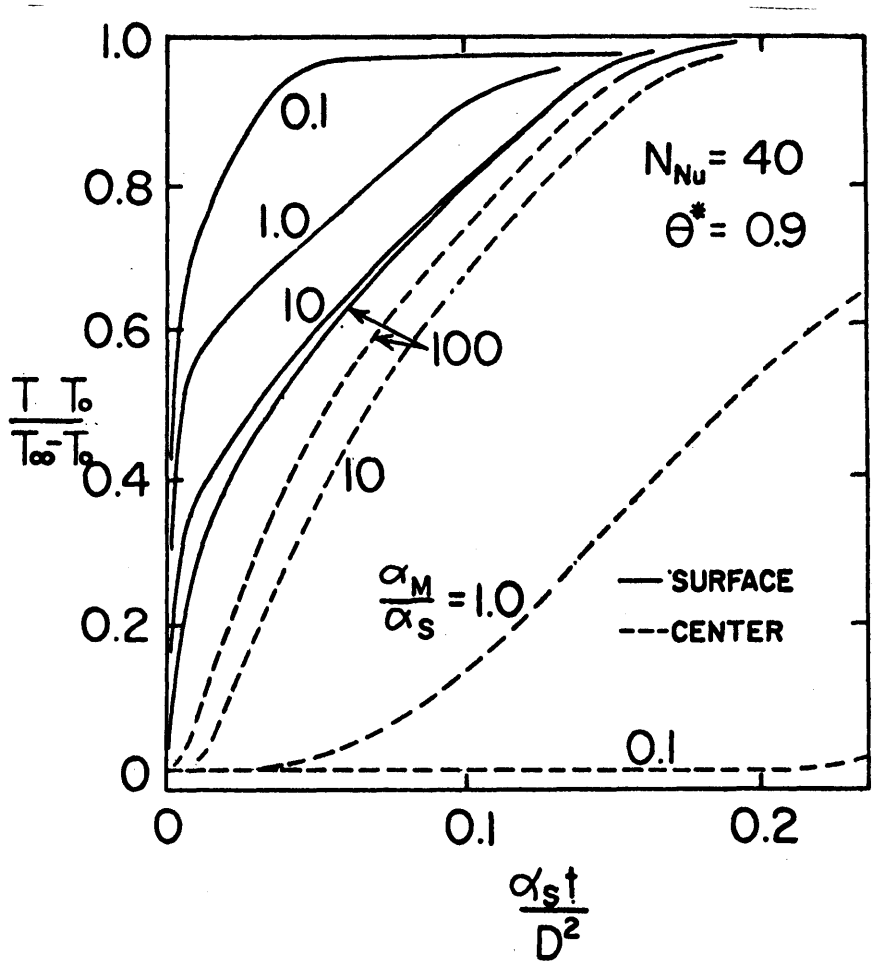

Figure VI-23 Calculated temperatures at the surface and the center of a metal sphere with various thermal diffusivity fractions α_M/α_S

parison between the experimental and calculated heating curves for the porous sphere is shown in Figure VI-24. The calculated heating curve for the 100 mesh iron sphere uses the properties listed in Table III-2 and the calculated thermal conductivity from Section V.F which depends on the temperature of the sphere. The agreement between the experimental heating curve and the calculated heating curve is not close during the initial stages of heating. The agreement improves with the time of immersion.

The effects which are excluded from the mathematical model curve are the moment of gas in pores of the sphere; and the temperature dependence of the specific heat of the metal sphere. A considerable amount of expanding gas evolves from the porous sphere. When the iron tube which is used to support the sphere is not sealed, the expanding gas flows past the thermocouple and up through the tube. The convection in the pores of the sphere which is caused by this gas flow contributes to the conduction in the gas pores, and accounts for much of the discrepancy between the calculated and experimental heating curves. Some of this discrepancy may also be due to the initially lower specific heat of the porous sphere. The temperature dependence of the specific heat of iron is neglected in the calculations with the model. If the specific heat of the iron at a lower temperature is used in the calculations, then the thermal diffusivity of the sphere is higher and the heating curve would more closely agree with the experimental curve.

For the 50 mesh iron sphere, experimental heating curve is above the curve for the 100 mesh sphere in Figure VI-24. This 50 mesh iron sphere has a greater porosity and a greater pore size, so the calculated thermal

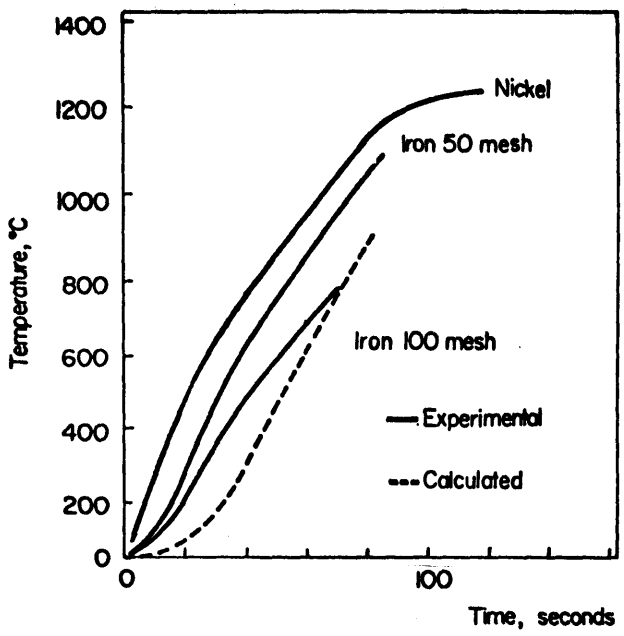

Figure VI-24 Comparison between the experimental and calculated heating curves for porous iron spheres. Experimental conditions in Figure IV-23.

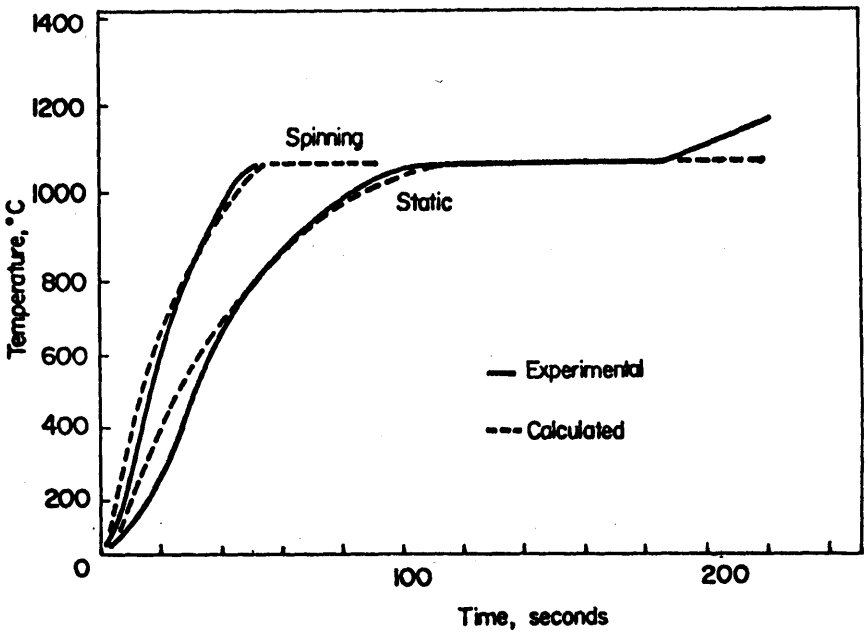

Figure VI-25 Comparison between the experimental and calculated heating curves for copper spheres. Experimental conditions in Figure IV-24

conductivity is less than that of the 100 mesh sphere. The calculated heating curve for this sphere should be even lower than the curve for the 100 mesh sphere instead of the higher curve which is shown in Figure VI-24. Apparently, the effects of the convective heat transfer in the pores is even greater in this sphere. The pores are larger and better connected, so the gas may flow more freely in the pores of the 50 mesh iron sphere.

VI.E. Copper Spheres

A comparison between the experimental and calculated curves for the heating and melting of a copper sphere is shown in Figure VI-25. The agreement of the curves for the spinning copper sphere in slag N-1CU is good. For the static sphere in slag N-1R, the calculated curve is similar to the experimental curve during heating, but it indicates that the melting time is slightly longer than that observed in the experiment. It is possible that the heat from the non-steady state boundary layer may have shortened the actual melting time of the sphere. As is discussed in Section VI.D.4, the heat flux from a non-steady state boundary layer during natural convection may be three or four times greater than the calculated steady state heat flux. The additional heat flux may have shortened the melting time of the sphere.

VI.G. Summary

1. The mathematical model with a planar solid-liquid interface accurately simulates the heating of a cold metal sphere in most liquid slags.

2. The solid-liquid interface is planar during solidification and

melting of the slag, apparently because the mushy solid-liquid region is sheared away from the sphere.

3. The temperature at the solid-liquid interface in the slag is the solidus temperature of the slag.

4. The thermal conductivity of the slag shell which is solidified on the sphere may be increased by the orientation of the crystals in the direction of heat flow.

5. The most important properties of the slag which control the heating of the sphere in the presence of the slag shell are the solidus temperature and the thermal conductivity of the solid slag. After the shell is melted away the thermal conductivity of the liquid is the most important property.

6. The convection in the liquid slag greatly affects the heating of the sphere, if the solidus fraction $\frac{T_S-T_o}{T_\infty-T_o}$ is below 0.95 and the Nusselt number $\frac{h_L D}{K_L}$ is above 10.

7. The heat transfer coefficient during the bubble stirring at a low or intermediate gas flow rate is more closely estimated by the power dissipation by the rising bubbles.

8. At a higher gas flow rate, the heat transfer coefficient for bubble stirring should be based on the velocity of the liquid slag and the porosity of the solid and liquid slag.

9. An increase in the surface area of the metal object at a constant volume decreases the heating time proportionally as shown by the comparison between the heating of the nickel cylinder and sphere of equal

volume.

10. The thermal conductivity of the porous iron sphere may be greatly affected by the convective heat transfer in the gas pores.

VII. APPLICATION OF THE MATHEMATICAL MODEL TO THE FEEDING OF IRON PELLETS

Iron pellets in an electric furnace are heated and melted in the liquid slag layer. The mathematical model and the results of the experimetal measurements which were presented in Chapters V and VI allow the calculation of the time required to melt a single iron pellet in the slag. In this chapter this melting time of a single pellet is calculated under idealized furnace conditions. The effects of thermal interaction among the pellets on the melting time of a pellet is briefly developed.

VII.A. Feeding Operations

The feeding of porous iron pellets into an electric furnace is illustrated in Figure VII-1, where the pellets are shown in various stages of heating and melting in the slag. When a pellet falls into the liquid slag, it either floats or descends, depending on its density relative to the density of the liquid slag. Initially, the pellet is covered by a frozen shell of slag, which melts away as the pellet heats. In the usual case the temperature of the liquid slag is greater than the melting temperature of the iron, and the surface of the pellet heats to its melting temperature and begins to melt. The pellet may reside on the surface of the liquid slag, within the slag layer, or at the interface between the liquid slag and the liquid iron in the furnace.

The heat which flows to the pellets in the furnace is the sum of the heat flow to each of the N number of pellets which are present at any time.

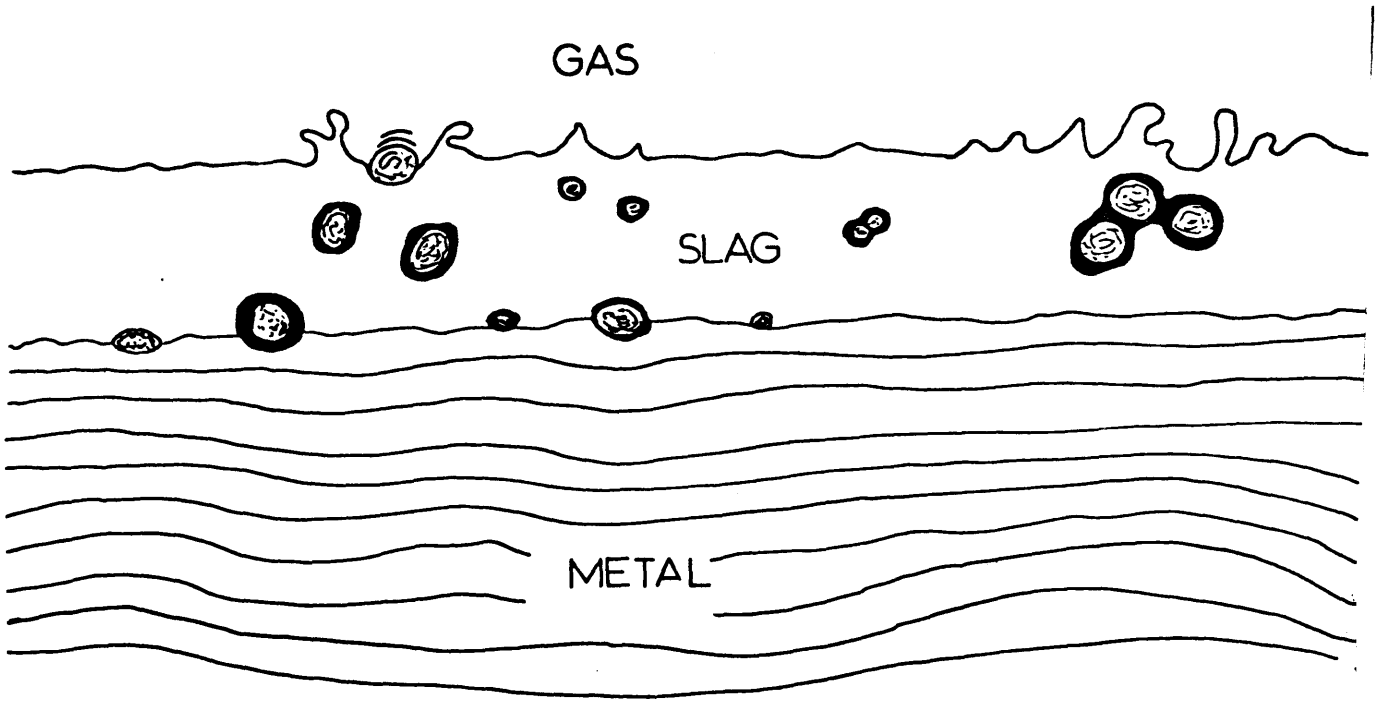

Figure VII-1 Iron pellets at various stages of heating and melting in an electric furnace steelmaking slag

$$Q_p = \sum_{n=1}^{N} A_n h_n (T_\infty - T_n) \qquad (1)$$

where T_∞ is the bulk temperature in the furnace

A_n is the surface area of pellet n

h_n is the heat transfer coefficient for pellet n

T_n is the temperature of the surface of pellet n

For a collection of pellet there are three conditions for heat flow which are summed in Equation (1). First some pellets are covered by a slag shell, and the area A_n is the surface area of this shell exposed to the liquid slag. The temperature at this surface T_n is the solidus temperature of the slag. In a later condition, the shell has melted away and some of the pellets are directly heated by the liquid slag. The area of these pellets is their original surface area, and the temperature at the surface T_n ranges from the solidus temperature of the slag to the melting temperature of the pellet. Finally, some of the pellets are melting, and their surface area A_n ranges from the original surface area to zero. The temperature at the surface of these pellets is the melting temperature of the pellet.

During the continuous feeding of the porous iron pellets, a heat balance is established in the furnace

$$Q_e + Q_c = Q_L + Q_p \qquad (2)$$

where Q_e and Q_c are the heat inputs from the arcs and combustion reactions in the furnace, respectively. The Q_L is the heat loss through the roof and the walls of the furnace. The heat flow to the pellets can also be expressed as the product of the mass feeding rate, M, and the enthalpy

for heating and melting of the pellet material, ΔH_p per mass

$$Q_p = M \cdot \Delta H_p \qquad (3)$$

At a steady state the heat from the arcs and combustion are balance by the heat losses and the heat flow to the pellets, as shown by Equation (2). The feeding rate M is fixed by this heat balance. The only way to increase the steady state feeding rate is to increase the heat from the arcs and combustion reactions or decrease the heat losses. The melting time of a pellet in the slag has no effect upon the steady state feeding rate.

During any transient in the operation of the furnace, the melting time of a pellet is one of the most critical factors. These transients occur during the start up of the furnace, the shut down, or as a result of any change in the feeding practice during operation. During start up of the feeding operation, a constant feeding rate M may begin at the same time as the power goes to the arcs. The number of pellets which is present in the furnace N increases at a constant rate as shown in Figure VII-2b. When the feeding operation reaches a steady state the rate at which the pellets melt is equal to the rate at which they are fed into the furnace, M. The total number of pellets present in the furnace at this steady state is

$$N = \frac{3Mt_m}{4\pi\rho_p r_p^3} \qquad (4)$$

where ρ_p is the density of the porous iron pellets, t_m is the time required to melt a single pellet, and r_p is the initial radius of the pellet,

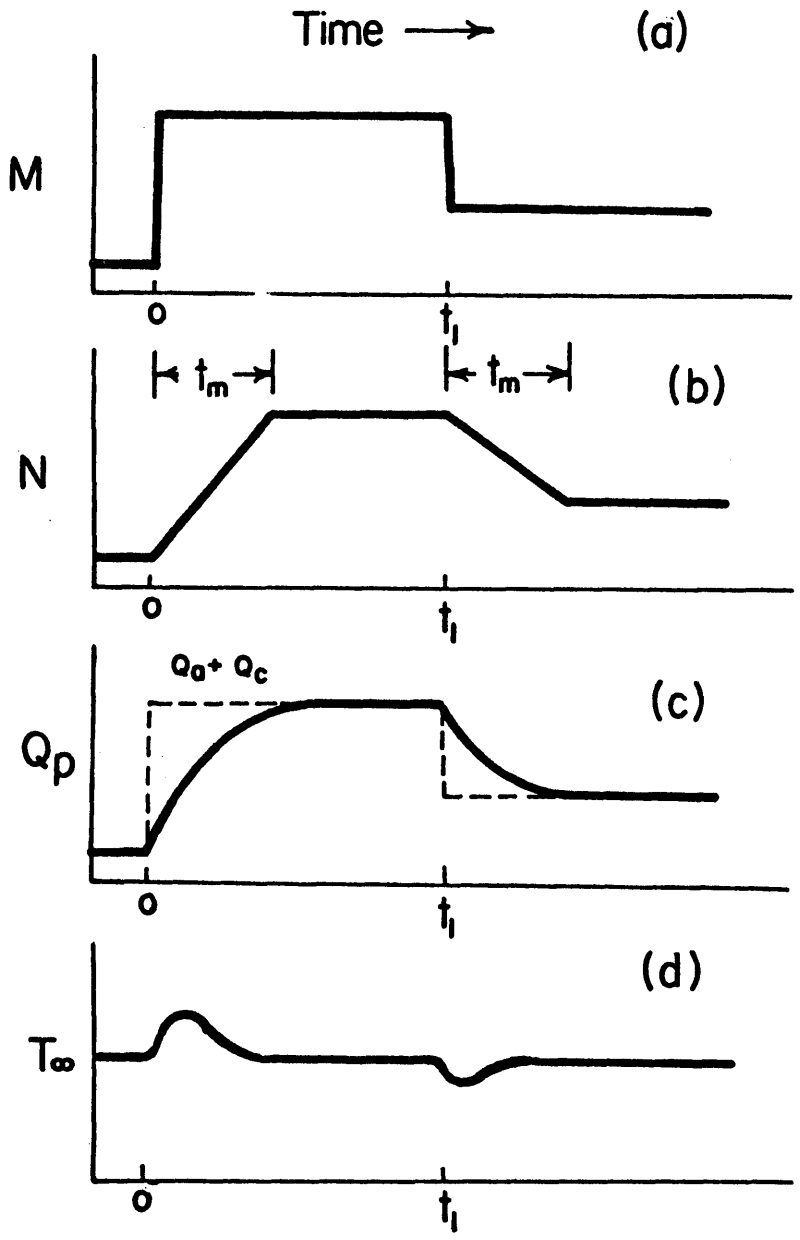

Figure VII-2 Effects of two transients in the feeding rate M on the number of pellets in the furnace N, the heat flow to the pellets Q_p, and the temperature of the bath T_∞

assuming the pellets are spheres. At a constant feeding rate M the time which is required to feed N number of pellets into the furnace is the melting time of a single pellet t_m. This melting time t_m is the length of the transient start up time, as shown in Figure VII-2b.

For a change in the feeding rate M during the operation of the furnace, the transient time is that required to reach the new steady number of pellets in the furnace, as shown at time t_1 in Figure VII-2a. The transient time in this case is also the melting time of a single pellet t_m, because the final pellet which was fed at time t_1 must be completely melted before a new steady number of pellets is achieved.

When the steady state number of pellets is achieved in the bath, the heat balance in Equation (2) is satisfied. This balance is shown in Figure VII-2c where the total heat input $Q_a + Q_c$ is plotted as a function of time, and the heat flow to the pellets is also plotted. Heat losses from the furnace are neglected in this figure. The heat flow to the pellets increases at a nearly constant rate as the number of pellets in the bath N increases at a constant rate. There is a slight deviation from a constant increase in heat flow because the pellets which are in the process of melting have less surface area and less heat flow per pellet. When the number of pellets in the furnace reaches a steady state, the heat flow to the pellets balances the heat input into the furnace. The temperature of the bath in the furnace also reaches a steady state at the same time t_m as shown in Figure VII-2d.

VII.B. The Melting Time for a Single Thermally Isolated Pellet

Since the melting time of a single pellet determines the transient

time for any changes in the feeding operation, it is important to establish the factors which control this melting time. The previous discussions of the heating a metal sphere in a liquid slag (Chapter VI) apply directly to the melting of the pellet in the liquid slag. Because practical porous iron pellets range in density from 2 to 6 g/cm^3, the heating and melting of the pellet occurs either entirely in the liquid slag or at the boundary between the liquid slag and the liquid iron in the furnace.

The finite difference mathematical model which is described in Chapter V was modified to calculate the time to melt a single porous iron sphere. The mathematical model calculated the temperature of the sphere, the solidification and melting of the slag on the sphere, and the melting of the porous iron sphere under idealized conditions in an electric furnace.

It is assumed that the pellet is a sphere, it is thermally isolated from the other pellets in the furnace, and the temperature of the bulk liquid metal and liquid slag is constant.

If the density of the pellet is greater than that of the liquid slag, the pellet descends at Stokes' velocity U_s

$$U_s = \frac{2}{9} \frac{(\rho_p - \rho_L)}{\mu} r_p^2 g \qquad (5)$$

where the ρ_L is the density of the liquid slag, g is the gravitational constant, and μ is the viscosity of the slag. The heat transfer coefficient h_L during this descent is calculated from Equations (6) and (7) as described in Section V.D.2 (78)

$$\bar{h} = \frac{\bar{N}_{Nu} K_L}{D} \tag{6}$$

$$\bar{N}_{Nu} = 2.0 + 0.6\, N_{Re_v}^{1/2}\, N_{Pr}^{1/3} \tag{7}$$

The D is the diameter of the pellet and K_L is the thermal conductivity of the liquid slag. The density and the thermal conductivity of the porous pellet are calculated as described in Section V.E. The numerical values which are used in this mathematical model are listed in Table VII-1. These values represent typical conditions in the refining operation of an electric furnace (14).

If the density of the porous pellet is greater than the density of the liquid slag, the pellet reaches the interface between the liquid iron and the liquid slag. At this interface the pellet displaces an appropriate mass and volume of liquid iron and liquid slag according to the balances

$$V_p = V_I + V_S \tag{8}$$

$$\rho_p V_p = \rho_I V_I + \rho_S V_S \tag{9}$$

where V_p, V_I, and V_S are the volumes of the pellet, the displaced liquid iron, and the displaced liquid slags; ρ_p, ρ_M, and ρ_S are the densities of the pellet, the liquid iron and the liquid slag, respectively. The density of the pellet at a particular time is calculated from the original density of the pellet and the mass of the slag which is frozen on the pellet. Both the surface area of the pellet in contact with the liquid iron andthe surface area in contact with the liquid slag are calculated from the condition of buoyancy in Equation (9). In this model the position of the pellet and the areas of contact are calculated

Table VII-1. Numerical Values for Calculation of the Melting Time of Various Porous Iron Pellets

Slag	
Depth (L)	30 cm
Density (ρ_L)	2.9 g/cm^3
Thermal diffusivity	0.004 cm^2/sec (Liquid-solid)
Specific heat	0.28 cm/g°C
Melting point	1500°C
Heat of fusion	110 cal/g
Bulk temperature	1600°C
Power number N_p	44
Pellet	
Density	2-6 g/cm^3
Radius	0.5, 1.5, 3.0 cm
Melting point	1530°C
Heat of fusion	60 cal/g
Initial temperature	30°C
Pore diameter	0.01 cm.

as a function of the time of immersion.

The heat transfer coefficient for the pellet, if it is suspended in the liquid slag or at the interface between the liquid iron and the liquid slag, are calculated by the power dissipation from the carbon boil. This calculation is described in Section V.D.3. The numerical values of the power number N_P (listed in Table VII-1) represents a vigorous carbon boil. The porosity of the slag is neglected in the present calculation, but during the carbon boil the slag may be filled with small gas bubbles which increase the porosity of the slag. This increased porosity decreases the density and thermal conductivity of the slag greatly, as discussed in Section VI.D.4.

The melting of the iron pellet is calculated in the present mathematical model. When all of the frozen slag melts from the pellet, the surface of the pellet heats to the melting point of iron. It is assumed that the pellet remains spherical throughout this melting. The heat balance at the melting interface is

$$K_M \frac{(T_i - T_M)}{\ell_j} + h_L (T_\infty - T_M) = \frac{\rho_M \Delta H_M}{\Delta t} (L_{j+1} - L_j) \qquad (11)$$

where K_M is the thermal conductivity of the porous iron

h_L is the heat transfer coefficient

T_M is the melting temperature of the iron

T_∞ is the bulk temperature in the furnace

ρ_M is the density of the porous iron

ΔH_M is the heat of fusion of iron

T_i is the temperature at the center of the adjacent metal element

L_j is the previous distance from the center of the metal sphere to the melting surface

L_{j+1} is the new distance from the center of the metal sphere to the melting surface after time Δt

Δt is the time increment

ℓ_j is the distance between the center of the adjacent metal element and the melting surface

Similar to the planar boundary condition for melting slag, this balance is used to calculate the movement of the solid metal-liquid slag interface. The temperature distribution in the pellet and the position of the solid-liquid interface are calculated until only 2% of the original volume of the pellet remains.

Using this mathematical model of a thermally isolated porous iron pellet, the temperatures at the surface and the center of a particular pellet are calculated as a function of time, as shown in Figure VII-3. The radius of the pellet is also shown in this figure. This particular pellet falls through the 30 cm. of liquid slag to reach the liquid iron-liquid slag interface in about one second as shown by the dashed line.

The temperature of the surface of the pellet reaches the melting temperature of iron in just over a second in Figure VII-3, but the temperature at the center of the pellet responds slowly to the flow of heat from the liquid slag and liquid iron. For these particular conditions the radius of the pellet increases slightly when the slag freezes on the pellet during the first second. During most of the time, the radius of the pellet decreases at a constant rate because the pellet is melting. The calculated melting time for this pellet is about 15 seconds.

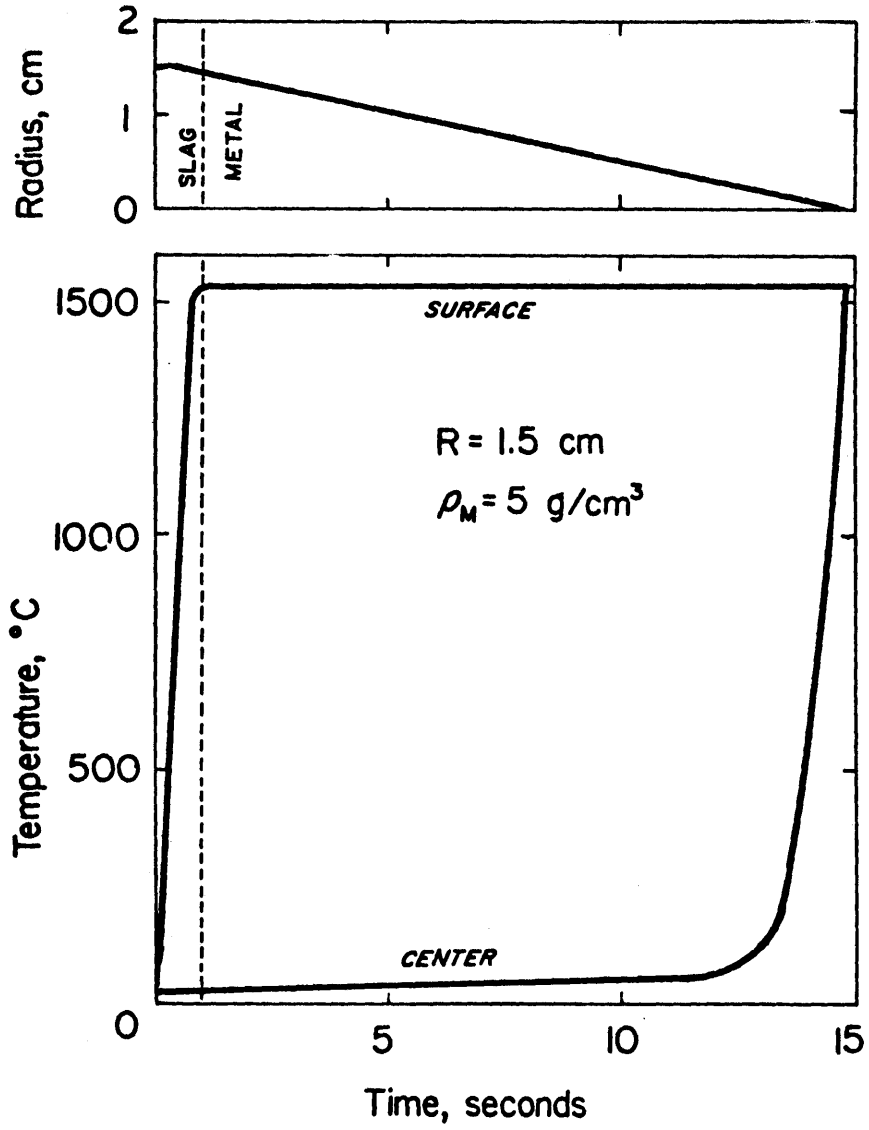

Figure VII-3 The calculated size and temperatures at the surface and the center of a thermally isolated pellet in an electric furnace as a function of the time of immersion

The calculated melting time for the pellets of various radii and densities are shown in Figure VII-4. The density represents the original density of the porous iron pellet. The melting time in this figure increases with the decreasing density, because the time for the pellet to fall through the liquid slag and make contact with the liquid iron is longer. Also when the pellet reaches the liquid iron, the area of the pellet in contact with the liquid iron is less when the density of the pellet is lower. The melting time is much greater for a pellet which has a density close to that of the liquid slag. At this density a pellet is heated and melted almost entirely in the liquid slag.

If the slag porosity is increased by the carbon boil, the density of the slag is decreased. This decrease in density shifts the curves for the melting time in Figure VII-4 to the left. The increased porosity also lowers the thermal conductivity of the slag and the melting times for a pellet with a density near the density of the porous slag is increased. During a carbon boil gas bubbles may cling to the pellet and reduce the effective density of the pellet also.

VII.C. Relationship Between the Melting Time and the Heat Transfer Coefficient

By rearranging Equation (4) the melting time for a porous pellet is

$$t_m = \frac{4\pi\rho_p r_p N}{3M} \qquad (12)$$

The feeding rate M is related to the heat flow to a collection of pellets in the furnace by Equation (3). Substituting Equation (1) and (3) into Equation (12), the melting time is

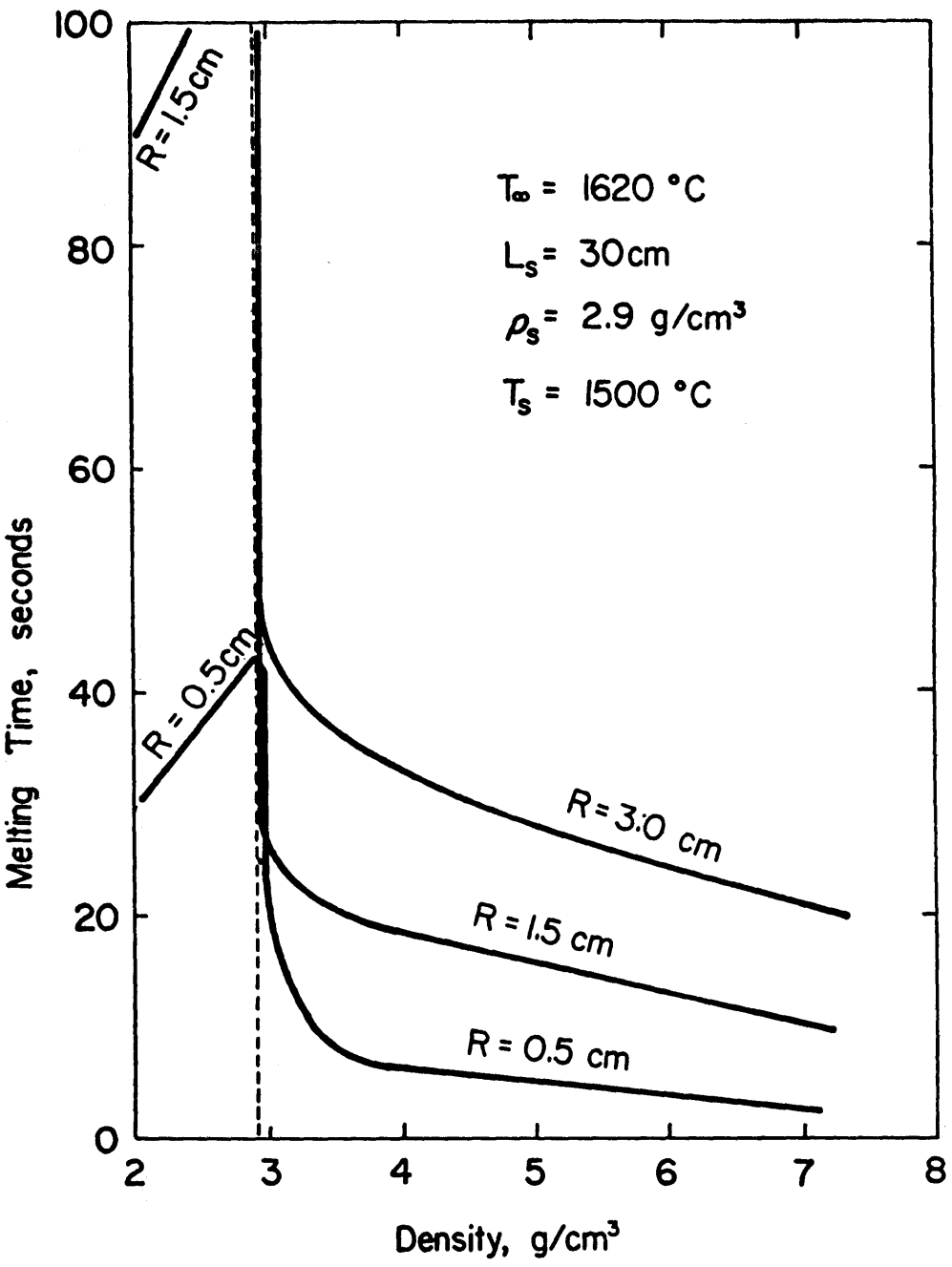

Figure VII-4 Melting time of thermally isolated pellets of various sizes and densities

$$t_m = \frac{4\, r_p^3 \rho_p N \Delta H_p}{3 \sum_{n=1}^{N} A_n h_n (T_\infty - T_n)} \qquad (13)$$

Equation (13) can be simplified by observing that the temperature at the surface of the pellet T_n remains at the melting temperature of iron throughout most of the time of immersion, as shown in Figure VII-3. Also the heat transfer coefficient based on power dissipation is nearly independent of the pellet diameter and is essentially constant throughout the melting of the pellet. For a collection of pellets in the furnace, most of the pellets would have the same heat transfer coefficient and the same temperature at the surface in Equation (13). Also, an average area $\bar{A}_n$ for the collection of pellets in the furnace can be calculated from the average radius of a melting pellet. Since the pellet melts at a constant rate as shown in Figure VII-3, the average radius is $r_p/2$. Substituting the average area, heat transfer coefficient, and surface temperature into Equation (13) gives

$$t_m \cong \frac{2\rho_p r_p \Delta H_p}{3\bar{h}(T_\infty - T_m)} \qquad (14)$$

According to Equation (14) the melting time of a porous pellet is inversely proportional to the heat transfer coefficient. This heat transfer coefficient depends on the density of the pellet relative to the slag, the mixing in the bath, and the interaction among the pellets. The effect of the heat transfer coefficient on the melting time for various modes of operation is shown in Figure VII-5. A constant heat transfer coeffficient in Equation (14) is used to calculate the melting

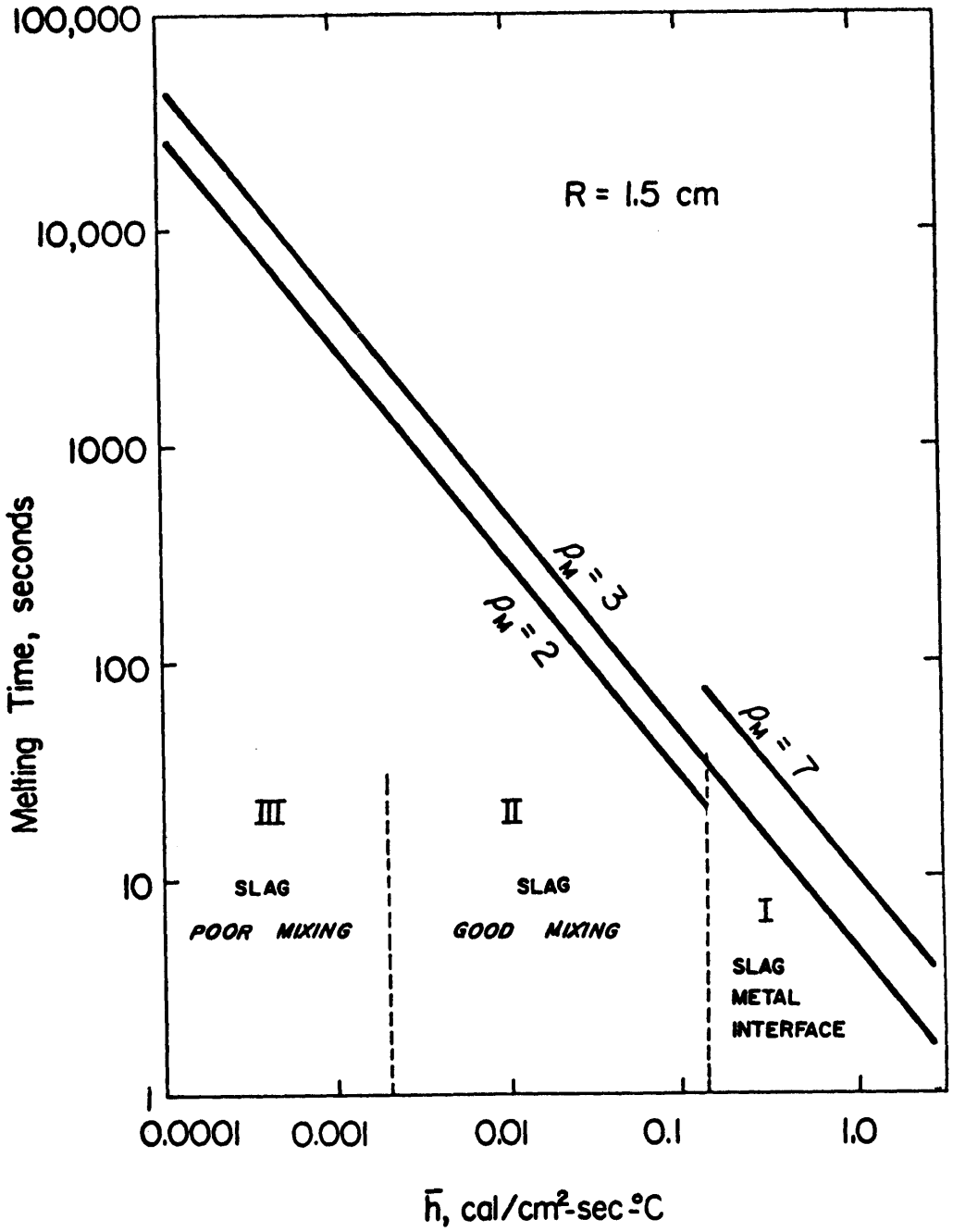

Figure VII-5 Melting time of a porous pellet as a function of heat transfer coefficient

times shown in this figure.

In region I of Figure VII-5 the metal pellets are sufficiently dense to reach the liquid slag-liquid metal interface in the furnace. The heat transfer coefficient in the liquid metal is very high. In Region II the density of the pellet is equal to or less than the density of the liquid slag. The pellet remains trapped in the liquid slag layer throughout the melting of the pellet. The mixing in the slag is sufficient to thermally isolate the pellets. At the lower limit of the region II the heat transfer coefficient is calculated from the correlation for natural convection to a thermally isolated sphere (Section V.D.2). Otherwise, the heat transfer coefficient in region II is calculated by the power dissipation in the liquid slag (Section V.D.3).

In region III of Figure VII-5, the mixing in the liquid slag is not sufficient to thermally isolate the pellets from one another. The thermal interaction among the pellets reduces the heat transfer coefficient as will be discussed in the next section. The melting time in region III may reach several hours. This is a prohibitively long transient for furnace operation.

VII.D. Heat Transfer Coefficients for Interacting Pellets

If the pellets in the furnace freeze together or effect the thermal boundary layer of adjacent pellets, they are interacting thermally, and the pellets are not thermally isolated. The factors which control the heat transfer coefficient during this interaction are the motion of the fluid between the pellets, the pellet concentration in the bath, and the

clustering or freezing of the pellets to one another.

The effect of particle interaction on the heat transfer coefficient are shown in Figure VII-6. The heat transfer coefficients for thermally isolated particles in a stirred bath are plotted as a function of the power number for the stirring in curve 1. This curve is based on the experimental and theoretical work of Brian and Hales (17) for melting ice particles. The heat transfer coefficients for particles which are not completely isolated is shown by the shaded area in this figure. This shaded area is based on the range of heat transfer coefficients which were calculated from many experimental systems compiled by Calderbank (21). A correlation was developed from these experimental heat transfer coefficients by Calderbank as shown in curve 2

$$\frac{h_L}{C_L \rho_L} N_{Pr}^{2/3} = 0.13 \left[\frac{P/m\ \mu}{\rho}\right]^{1/4}$$

The heat transfer coefficient is decreased by the interaction of the particles.

The Nusselt numbers for heat transfer to two equally sized spheres with their centers placed parallel to the direction of a laminar flow was calculated by Aminzadeh et al. (79). The average Nusselt number for the front and back sphere decreases as the distance separating the sphere decreases, as shown in Figure VII-7. When the spheres are nearly touching at a low flow velocity v_L the Nusselt number is below the value of 2. If additional spheres are brought into the area, it is reasonable to assume that the Nusselt number would decrease further.

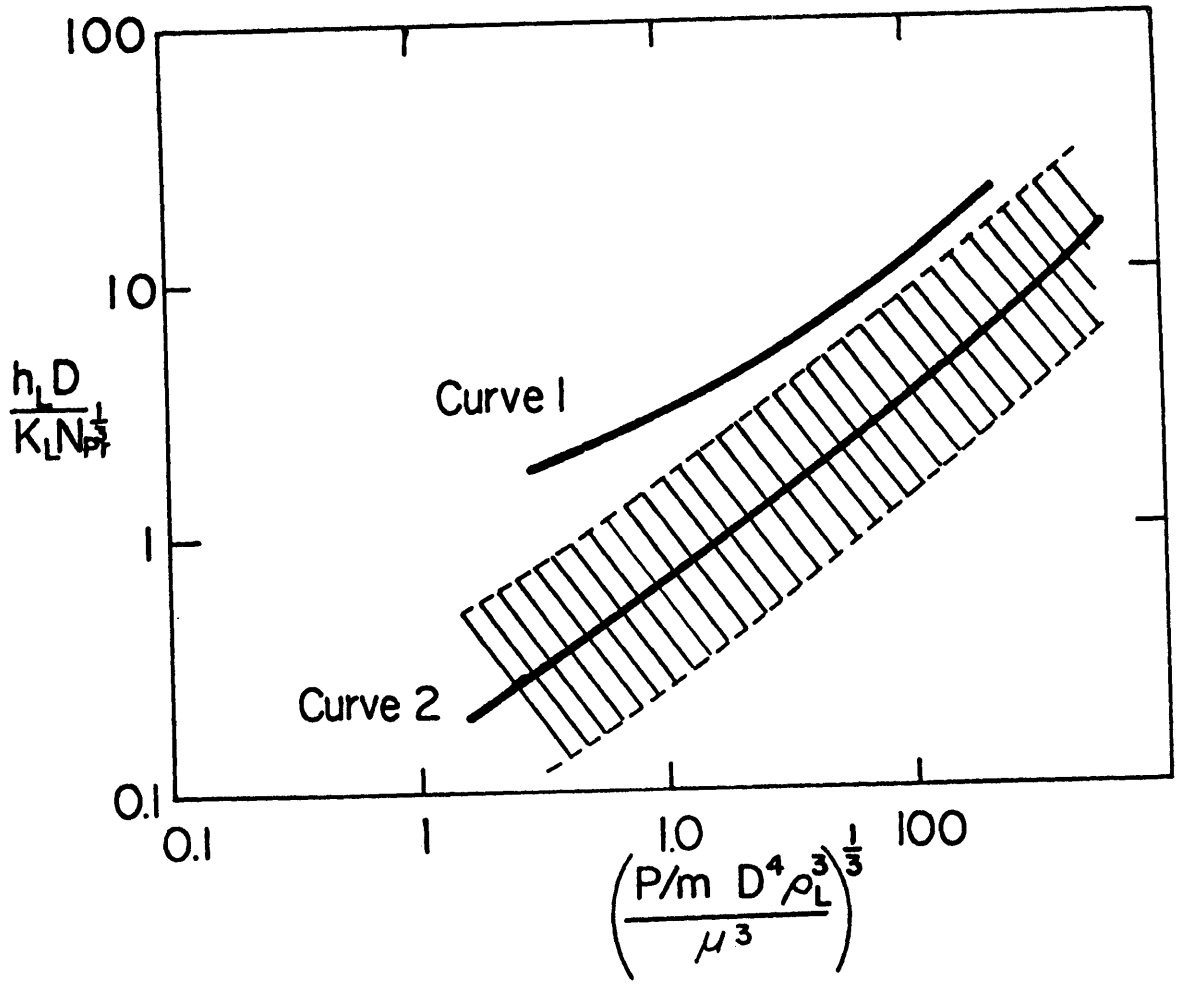

Figure VII-6 Heat transfer coefficients for suspended particles in a fluid as a function of the power dissipation. Curve 1 is for thermally isolated particles (17). Curve 2 is for interacting particles (21)

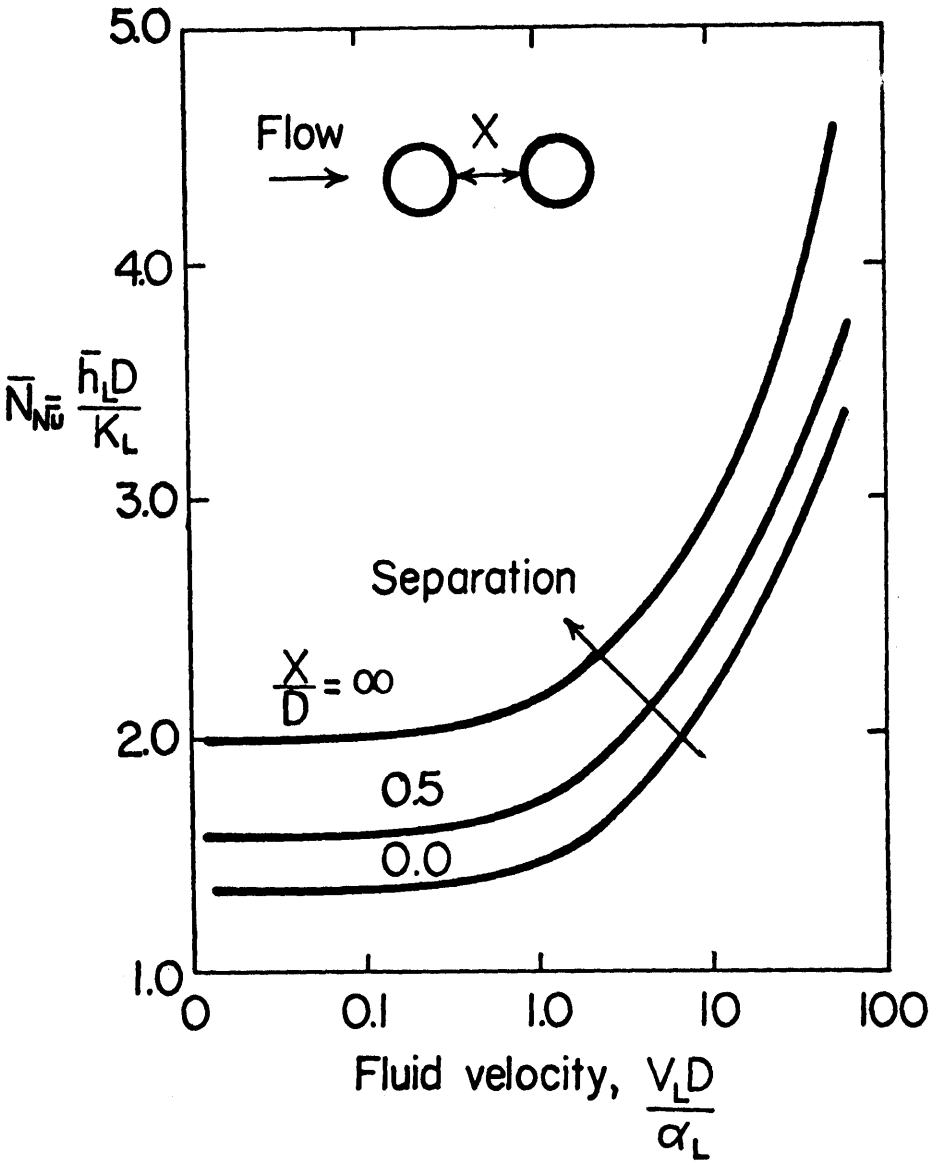

Figure VII-7 Heat transfer coefficients for two separated sphere as a function of the laminar flow rate and deparation between the spheres (79)

There are no experimental or theoretical studies available at present to quantitatively asses the effects of the interaction of multiple particles suspended in laminar or turbulent flow.

VII.E. Conclusions on the Feeding of Iron Pellets

During the continuous feeding of pellets into an electric furnace, the steady state operation is achieved in approximately the time which is required to melt a single pellet. Pellets which are much more dense than the liquid slag reach the liquid iron in the furnace and melt quickly. Pellets which are less dense remain in the liquid slag and melt more slowly. The melting time for a pellet depends directly on the heat transfer coefficient for the pellet. If the pellets are thermally isolated from one another in the furnace, the heat transfer coefficient may be determined by the power dissipation due to the carbon boil. If the pellets are not thermally isolated, then the heat transfer coefficient may be much lower. The melting time for a pellet which is thermal interacting with the other pellets is extremely long and disadvantageous to furnace operation.

In the operation of a continuous feeding process, it is necessary to minimize heat losses from the furnace, and minimize the time required to produce a heat of iron. To minimize the heat losses from the furnace the temperature of the slag layer should be kept to a minimum. Only enough heat should be added to the furnace as is required by the number of pellets that are present. During a transient in the operation of the furnace this heat input should be carefully adjusted to supply heat to the pellets which are present and maintain a constant bath temperature.

Too much heat input increases the heat losses from the furnace, and too little heat input allows the temperature of the bath to decrease and the melting time of a pellet to increase, which prolongs the transient. To minimize the time required to produce a heat of iron, fast melting pellets should be used and transients during the furnace operation should be avoided. If the pellets are allowed to freeze or cluster the melting times are greatly increased and the resulting transients in furnace operation are excessive.

VIII. GENERAL SUMMARY OF THE THESIS

Experiments were conducted to determine the heating of a metal sphere in a liquid slag. In these experiments the slag solidified on the surface of the sphere and then melted away as the sphere heated. The temperature inside nickel, copper, and porous iron sphere was measured during the heating in the slag. The composition of the liquid slag and the motion of the liquid around the metal sphere were varied.

A mathematical model was developed which could be used to calculate the temperature inside the sphere while immersed in the slag. This mathematical model solved the heat conduction equations in the solid metal and solid slag using a smooth or planar moving boundary condition for the solidification and melting of the slag. The heating curves for the sphere which were calculated with this model were compared to the experimental heating curves. The agreement was good for most of the slags and conditions which were studied. The smooth or planar interface may have resulted when the mushy region at the solid-liquid interface was sheared away by the motion of the liquid.

Comparisons between the calculated and experimental heating curves indicated that the temperature at the solid slag-liquid slag interface was the solidus temperature of the slag in most cases. This solidus temperature and the thermal conductivity of the solid slag had the greatest effect on the heating of the sphere in the liquid slag. The thermal conductivity of the solid slag may have been increased in some cases by the orientation of the crystals in the direction of heat flow.

At the solid-liquid slag interface the heat flux from the liquid slag was controlled by the difference between the solidus temperature and the bulk temperature of the slag, and the heat transfer coefficient in the liquid. The heat transfer coefficient for the spinning sphere and natural convection to the sphere could be accurately calculated, while the heat transfer coefficient for bubble stirring in the slag was not as accurately calculated. For the porous iron sphere, the calculated heating curves indicated that the surface of these spheres heated faster than the surface of the solid spheres because of the low thermal conductivity of the porous spheres.

Dimensionless heating curves for the surface of a sphere immersed in slag were calculated with the mathematical model. These curves could be used to estimate the effects of the thermal diffusivity of the solid slag, the solidus temperature of the slag, the diameter of the sphere, the bulk temperature of the slag, the initial temperature of the sphere, the heat transfer coefficient in the liquid, and the thermal diffusivity of the sphere.

The mathematical model which was developed and tested by the comparisons with the experimental heating curves was used to simulate the heating and melting of a porous iron pellet in an idealized electric furnace. The melting time for porous pellets was calculated for a practical range of pellet sizes and densities. For a collection of pellets, it was shown that the heat transfer coefficient in the liquid slag is inversely proportional to this melting time. The heat transfer coefficient was controlled by the mixing in bath, the thermal conductivity

of the liquid slag, and the thermal interaction among the pellets in the bath.

During the continuous feeding of pellets into an electric furnace, the melting time of a single pellet determines the time which is required to reach a steady state following a change in the feeding or heating operation. The time for melting a pellet in the slag is not important to the steady state operation of the furnace but it is critical to any transients in the operation.

IX. FURTHER RESEARCH

Further studies on the heat transfer in silicate slags should concentrate on the properties of the solidified slag shell. These studies should center on the thermal conductivity of the phases present in the solid, the effects of orientation on the thermal conductivity of solidified slag, the solidus temperature of practical metallurgical and coal slags, and the mechanical strength of the solid at high temperatures.

Study is also needed to describe the effects of gas bubbles rising from the bottom of the slag and from the surface of the porous sphere. The effects of the expanding gas in the porous sphere on the thermal conductivity of the sphere should be considered.

An experimental and theoretical study is needed on the interaction among particles suspended in a liquid, like pellets in an electric furnace. Such a study should determine the criterion for thermal isolation and an effective heat transfer coefficient for a particle as a function of the particle concentration in the liquid and the clustering of the particles.

For the analysis on continuous feeding of pellets into an electric furnace, the model for melting a porous sphere in slag should be tested by experiments. The transient time for a continuous feeding operation should be measured and compared to the melting time of an individual pellet. Also, the specific case of a porous metal melting in a slag with a solidus temperature of the slag below the melting temperature of the metal should be tested separately.

The mathematical model which is developed in this thesis could be modified for application to the solidification of slag on boiler tubes and furnace walls. The model may also be applied to the solidification of a continuously cast strand of steel whose surface is protected by a slag flux.

APPENDIX A. THE EFFECT OF THE THERMOCOUPLE PROTECTION

The temperature recorded by the thermocouple at the center of the metal sphere in the heat transfer experiments described in Chapter III was affected by the material which was used to protect it from contamination. In the experimental heating curves, the effects of the protection of the thermocouple was most noticeable during the initial heating. When alumina was used to protect the thermocouple there was a 10 to 15 second delay before the thermocouple responded to the heating of the sphere. When the platinum foil was used, this delay was usually less than five seconds. The delay in response was very important in developing the mathematical model which simulated the heating of the metal sphere in the slag and the response of the thermocouple to this heating.

To determine the effect of the protection of the thermocouple on the temperature response, experiments were conducted in a thermal radiation furnace with the nickel sphere in the absence of slag. The radiation furnace was prepared by inductively heating a graphite crucible (30.5 cm. deep and 1.5 cm. thickness of the walls), covered by a 3.0 cm. thick graphite lid with a 4.5 cm. diameter opening. A 3.0 cm. nickel sphere was attached to an iron tube for support. Then a platinum/platinum 10% rhodium thermocouple was positioned at the center of the sphere with one of the following protective materials between the thermocouple bead and the nickel sphere: 1) tightly packed zinc powder, 2) 1 mm. thick dense alumina protection tube, and 3) nothing. The crucible was heated to 1200°C, as measured on the inside wall by an optical pyrometer. Once the furnace reached a steady temperature, the

sphere was inserted through the opening in the lid so that the sphere was suspended at the center of the graphite crucible. The response of the thermocouple was recorded by a millivolt recorder as a function of time.

Using the same sphere and same furnace temperature, the temperature which was recorded by the thermocouple is shown in Figure A.1. The temperature recorded when the thermocouple is packed with zinc powder best indicates the temperature at the inside wall of the nickel sphere, since the heat transfer through the zinc should be the best. The temperature recorded by the thermocouple which is protected by the alumina lags about 10 to 15 seconds behind the temperature recorded with the zinc. With no protection the temperature lags about 5 to 10 seconds. The four temperature recordings taken with the zinc protection (shaded area) and the 6 recordings taken with no protection are fairly consistant, while the 8 separate recordings with the alumina protection vary over a range of about 5 seconds or 30°C. The heating rate is slightly faster in the experiments with slag and the range in response should be larger.

The comparison of the temperatures which are recorded by the thermocouple inside the nickel sphere in Figure A-1 demonstrate that the thermocouple which is protected by the alumina is not a reliable indicator of the temperature inside the metal sphere. This is due to the long lag in response of such a thermocouple and the scatter of the response data. The thermocouple with no protection is not much better because its delay in response is also substantial. The best form of protection of the thermocouple is some metal packing which gives the

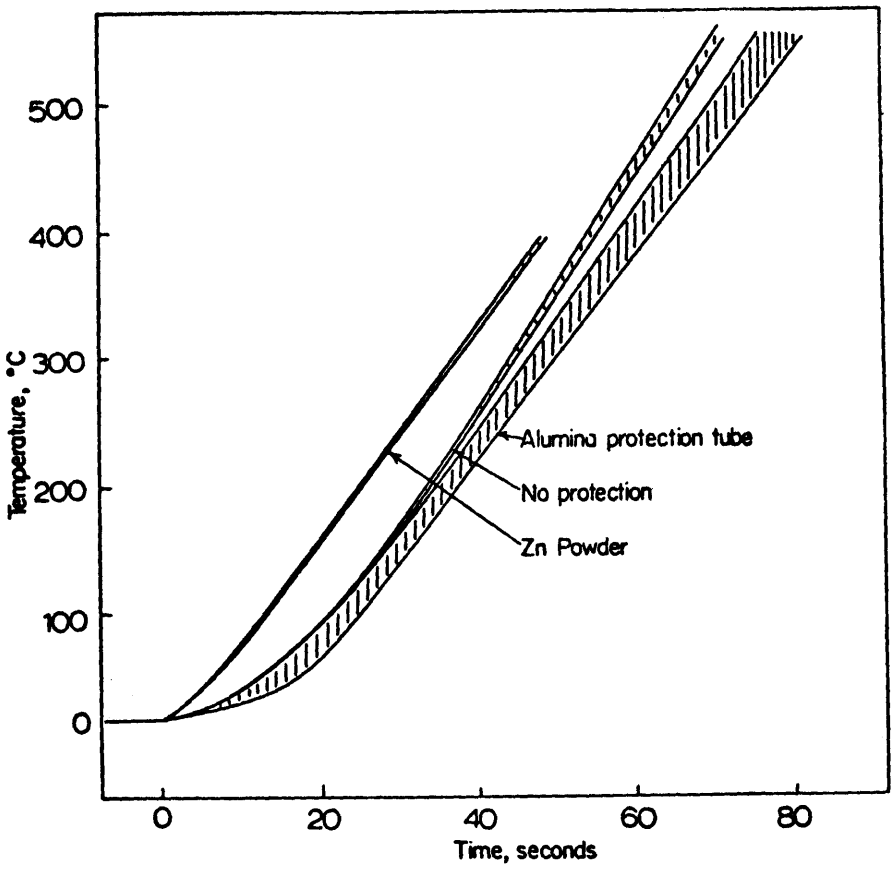

Figure A-1 Recorded response of a thermocouple with various forms of protection positioned at the center of a nickel sphere which is heated in a radiation furnace

bead an intimate contact with the nickel surface. For this reason the platinum foil was used on all of the heat transfer measurements in the liquid slag except for the early measurements with slag N-IR. The delay in the response for the thermocouple protected with platinum foil is expected to be about the same as the delay for the zinc powder. The delay for the platinum foil was not measured in this radiation furnace, but it is observed in the initial response of the thermocouple during the experiments with liquid slag, as shown in Figure IV-6.

APPENDIX B. THE EFFECTS OF THE SUPPORTING TUBE AND STEM

In the heat transfer experiments described in Chapters III and IV, the supporting iron tube and the metal stem, which is inserted into the tube, have a small effect upon the heating of the metal sphere in the slag. The surface of the metal sphere attached to the stem and iron tube is initially cooler than the surface exposed to the slag. Later, the stem and tube provide additional heat to the attached surface. The effects of the stem and iron tube as a heat sink and later as a heat source are discussed in this section. Two cases are considered: good contact between the stem and the tube and an interfacial resistance between the stem and the tube.

Since the 1.3 cm. diameter supporting iron tube is immersed about 5 cm. into the liquid slag, the tube is assumed to be heated only by the slag. The temperature distribution throughout the iron tube and the nickel stem is calculated directly from the mathematical model described in Chapter V using cylindrical coordinates and a heat transfer coefficient for a spinning cylinder. For perfect contact between the iron and the nickel, the temperature at the inside of the stem is shown by the dashed line in Figure B-1. The solid line in this figure represents the temperature calculated for the surface of the 3.0 cm. nickel sphere under the same slag conditions. Comparing the solid and dashed curves, the stem and tube act as a heat sink during the first 30 seconds and as a heat source, later. The overall effect of the stem and the tube is quite small because 1) the additional heat from the stem is nearly equal to the heat absorbed initially by the stem later, and 2) the area

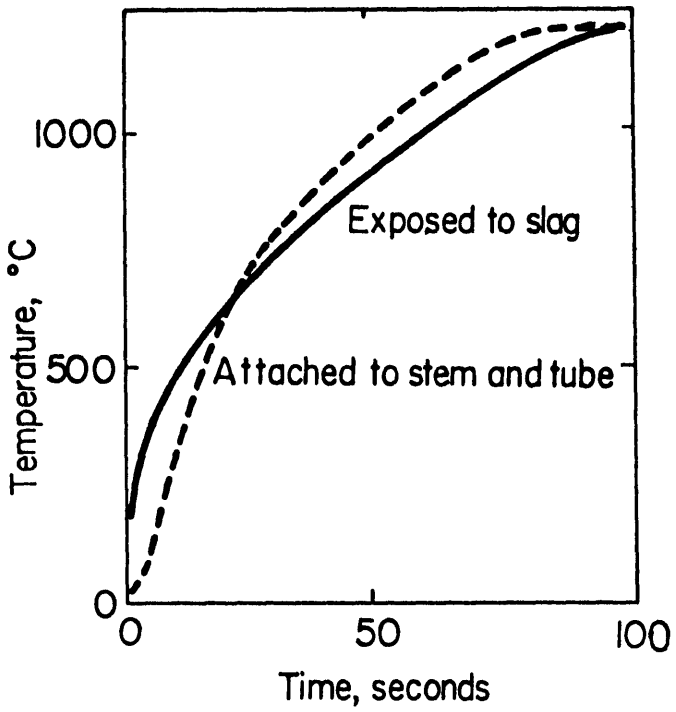

Figure B-1 Comparison between the temperature at the surface of a nickel sphere exposed to the slag and the surface attached to the nickel stem and iron tube. Calculated with the mathematical model assuming perfect contact between the stem and the tube

of the stem in contact with the sphere is only 1.2% of the total area of the sphere. For a 1.8 cm. sphere the surface temperature increases much more rapidly and the stem and tube draw heat from the sphere for a larger percentage of time. Also the effect of the stem and the tube is much more pronounced on the smaller sphere because the area of the stem is over 5% of the surface area of the sphere.

Because the contact between the iron tube and the nickel sphere is not perfect an interfacial resistance should be included in the calculations. The temperature of the iron tube, T_R, in contact with the metal stem is calculated with the mathematical model of slag heat transfer as before. The temperature of the stem T_{St} is calculated from Equation (1) if the temperature distribution within the stem is neglected.

$$\rho_{St} C_{St} V_{St} \frac{dT_{St}}{dt} = h_I A_{St} (T_R - T_{St}) \qquad (1)$$

where T_{St}, ρ_{St}, C_{St}, V_{St} and A_{St} are the temperature, density, specific heat, volume, and surface area of the stem, respectively. The h_I is the interfacial resistance between the tube and the stem. To calculate the temperature of the stem as a function of time, Equation (1) is written in finite difference form as shown in Equation (2) and inserted into the finite difference mathematical model

$$T_{St,\ j+1} = T_{St,j} - \frac{\Delta t A_{St} \bar{h}_I}{V_{St} C_{St} \rho_{St}} (T_{R,j} - T_{St,j}) \qquad (2)$$

The temperature of the stem T_{St} is calculated along with that of the tube wall, $T_{R,j}$, at each time step, j, in the model.

The temperature of the stem from this calculation is shown by the shaded area in Figure B-2, for a range of interfacial resistance from 0.02 ro 0.04 cal/cm^2-sec $^{\circ}C$ (66, 67). The solid line represents the calculated temperature at the surface of the exposed 3.0 cm. nickel sphere. Comparing the two curves, the stem and tube act as a heat sink throughout most of the time of immersion in the slag. The presence of the stem and tube should lower the heating curve of the immersed sphere. In the comparisons between the experimental and the calculated heating curves, no systematic lowering was observed. The effect is apparently absent because of the limited area of contact between the stem and the sphere.

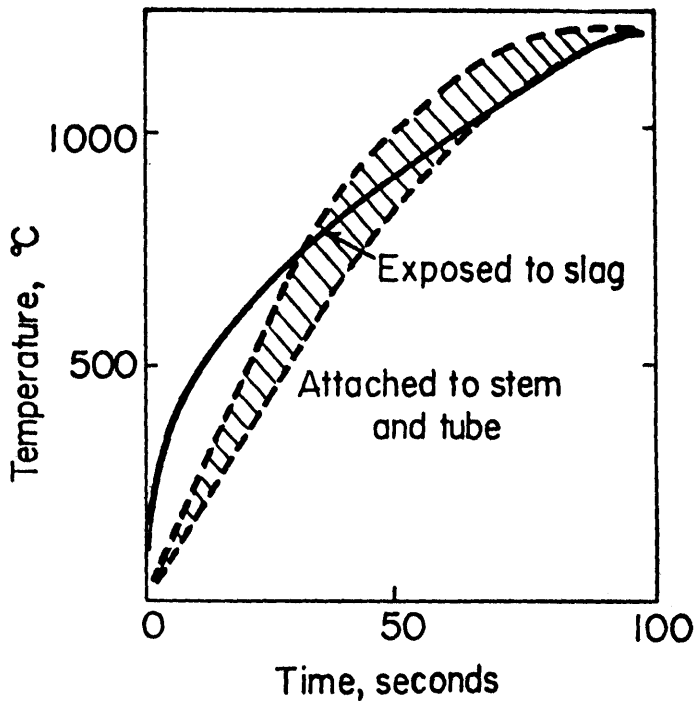

Figure B-2 Comparison between the temperature at the surface of a nickel sphere exposed to the slag and the surface attached to the nickel stem and iron tube. Calculated with the mathematical model assuming an interfacial resistance between the stem and the tube

APPENDIX C. RANDOM ERRORS IN EXPERIMENTAL HEATING CURVES

The temperature at the center of a 3cm. spinning nickel sphere in slag N-1CU or N-2CU at various bath temperatures is summarized in Figure C-1. In this figure the temperature recorded by the thermocouple after 50 and 100 seconds is plotted as a function of the measured liquid bath temperature for 14 different experiments. The temperatures recorded in the sphere is fairly consistent between one experiment and the next, but there is a distribution caused by random errors in the measurement of temperature.

Most of the error is probably due to variations in the position of the thermocouple inside the sphere. The measurements shown in Appendix A with a static sphere in a radiation furnace indicate a range of 5 to 15 degrees in the temperature inside the sphere. This range depends upon the protection and the position of the thermocouple. For a spinning sphere the position of the thermocouple is even less certain.

There are also several sources of error in the determination of the liquid slag temperature. As described in Chapter III the temperature of the liquid slag is determined from the temperature recorded by the thermocouple at the center of the metal sphere after reaching a steady value. The temperature measurement with the optical pyrometer sighted on the top of the liquid slag is consistently higher than the steady value which is recorded by the thermocouple in the sphere. Sometimes the steady temperature in the sphere is difficult to determine. The difficulty is due to fluctuations in the heating curve at the high temperatures and

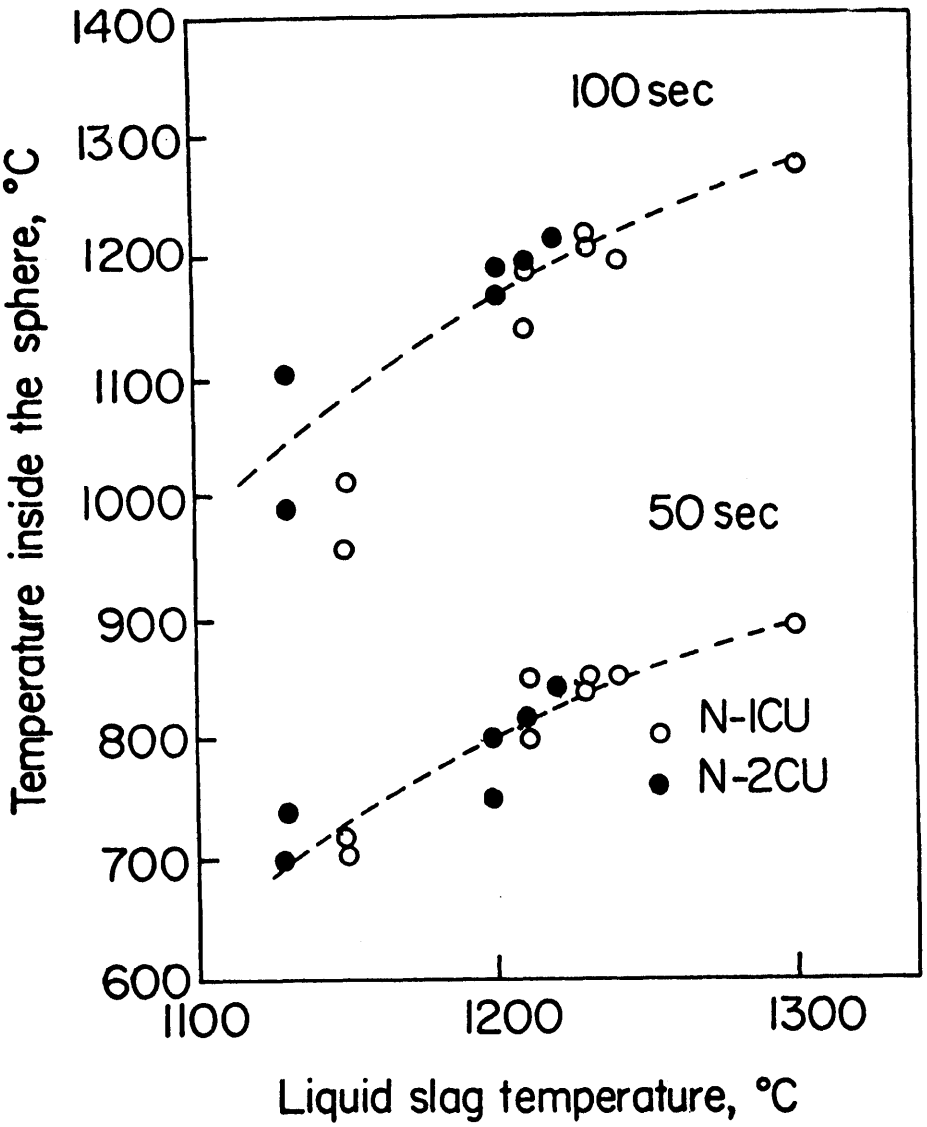

Figure C-1 Temperature inside a 3 cm. nickel sphere after 50 and 100 seconds of immersion in a liquid slag at various bath temperatures

occasional contamination of the thermocouple by liquid slag, which seeps into the supporting tube. There is also about 2 to 10°C of noise in the output of the thermocouple due to the spinning of the sphere, the vibrations of the slip rings and brush contacts, and the high frequency induction field. This noise is more pronounced at temperatures above 1000°C.

The liquid slag and metal sphere are sources of some random error. The temperature distribution in the bath is minimized before immersing the sphere by stirring the slag by hand. There is still a likely variation of 10° in the temperature of the liquid slag at the walls and in the center of the crucible. The mass of the solid metal sphere does not vary by more than 2%.

The composition of the slags is relatively consistent. The total iron content of the liquid slags was analyzed as described in Appendix G and it was found to agree well with the iron content as mixed and did not change more than 1% during an expeimental period. The iron crucible fixed the oxygen potential in the slags, so that diffusion of oxygen from the air into the slag was balanced by the dissolution of iron from the crucible. For the slag N-IR the oxygen potential was initially fixed by the excess iron which was added to saturate the slag with iron. In many experiments an iron sheet was inserted inside the MgO crucible to lengthen the life of the MgO crucible and to maintain the iron saturation. In the case of slag N-IR the graphite lid and susceptor lowered the oxygen potential in the gas surrounding slag N-IR so the oxygen diffusion

into the slag would be limited. Finally, no systematic effects on the heating curves were observed after the 10 to 12 hours of experiments with any of the slags in the MgO or iron crucible. The composition of the slag remained fairly consistent and what small changes occurred had not apparent effect on the heating curves measured.

Another possible source of error is the separation of the slag shell from the metal sphere due to the difference in thermal expansion between the nickel and the slag. A 3 cm. nickel sphere expands 1.7% (69) when it is heated from room temperature to 1000°C or 0.38 cm. along the circumference. The solid slag shell expands only about 1% (Fe_2SiO_4) (69) during this heating or 0.38 cm. along the interface with the nickel. This difference in expansion places the metal surface under compression and the slag shell under tension which may cause the shell to crack. The cracking of the shell at the interface would create a gap between the slag and the metal which may act as an additional resistance to the flow of heat to the sphere. In all of the experiments with liquid slag the shell was very adherent. No cracks in the slag shell were observed in any of the slag samples which adhered to the sphere. Either the solid slag was sufficiently plastic to accommodate the stress or it was strong enough to withstand the stress. An interfacial resistance at the slag metal interface was neglected.

APPENDIX D. COMPUTER PROGRAMS FOR SIMULATION MODELS

There are three computer programs which are used to simulate the heating of particles in the liquid slag:

1. Program for heating a sphere in liquid slag (with options for a copper sphere which melts in the slag, a nickel sphere, and a porous iron sphere).

2. Program for heating an infinite cylinder in liquid slag.

3. Program for heating and melting a porous iron sphere in an electric furnace.

The scheme for the initial heating of the metal object is the same in all of these programs.

1. Initialize the temperatures, areas, and volumes of all the finite difference elements.

2. Set an initial slag thickness.

3. Calculate the temperature distribution in the metal and solid slag with finite difference equations.

4. Calculate the movement of the liquid-solid slag interface.

5. Return to step 3 for the next time step.

Copies of the three programs are presented on the following pages with brief notes on the meaning of the terms and the calculations. All calculations were done in cgs units and °K.

```
PROGRAM FOR HEATING A SPHERE IN A LIQUID SLAG


*******  INPUT PROPERTIES OF SLAG AND SPHERE

      REAL M,IDT,IDR
      DIMENSION A(99),V(99),T(99),E(99)
200   READ(5,100)NO, NOT, NOS,NALP,NOME,IDR,IDT,TI,TO,TMS,TMSP
     C,ACR,ALP,SPIN,R,D,DS,CPL,CPS,U,CPM,CIN,DL,ALL,TM,PORE,CORR,ZZ
100   FORMAT(5I5/(8F10.4))
1002  WRITE(6,100)NO,NOT,NOS,NALP,NOME,IDR,IDT,TI,TO,TMS,TMSP
     C,ACR,ALP,SPIN,R,D,DS,CPL,CPS,U,CPM,CIN,DL,ALL,TM,PORE,CORR,ZZ
70    FORMAT( 8F10.4)
      IF(NO)201,201,50

                    NO = TOTAL NUMBER OF ELEMENTS
                    NOT = TOTAL NUMBER OF TIME STEPS ALLOWABLE
                    NOS = NUMBER OF ELEMENTS IN THE SLAG
                    IDR = WIDTH OF AN ELEMENT
                    IDT = LENGTH OF A TIME ELEMENT
                    TI = TEMPERATURE OF THE BULK LIQUID SLAG
                    TO = INITIAL TEMPERATURE OF THE METAL SPHERE
                    TMS = SOLIDUS TEMPERATURE OF THE SLAG
                    TMSP = LIQUIDUS
                    TMSP = LIQUIDUS TEMPERATURE OF THE SLAG
                    ACR = HEAT OF FUSION FOR THE SLAG
                    ALP = THERMAL DIFFUSIVITY OF THE SOLID SLAG
                    SPIN = NUSSELT NUMBER
                    R = RADIUS OF THE METAL SPHERE
                    D = DENSITY OF THE METAL SPHERE
                    DS = DENSITY OF THE SOLID SLAG
                    CPL = SPECIFIC HEAT OF THE LIQUID SLAG
                    CPS = SPECIFIC HEAT OF THE SOLID SLAG
                    U = VISCOSITY OF THE LIQUID SLAG
                    CPM = SPECIFIC HEAT OF THE METAL SPHERE
                    CIN = THERMAL CONDUCTIVITY OF THE SLAG METAL INTERFACE
```

```
                    DL  = DENSITY OF THE LIQUID SLAG
                    ALL = THERMAL DIFFUSIVITY OF THE LIQUID SLAG
                    TM = MELTING TEMPERATURE OF THE METAL SPHERE
                    PORE = POROSITY OF THE METAL SPHERE
                    CORR = SURFACE AREA AND THERMAL DIFFUSIVITY OF THE
                           THERMOCOUPLE PROTECTION TUBE
                    ZZ = THERMAL DIFFUSIVITY OF THE METAL SPHERE

*******  INITIALIZE AREA, VOLUMES, AND TEMPERATURES OF ELEMENTS

50      DR=(R-.1)/(NO-NOS-1)
        WRITE(6,71)
71      FORMAT('  TIME      RADIUS    SURFACE    CENTER  CAL/CM2-SEC')
        NOM=NO-1
        ALPM= ZZ
        KL = 0
72      DO 101 N=1,NOS
        J=0
        F(N)=TMS
        A(N)=((N-.5)*IDR+R)**2
101     V(N)=.333*((N-.5)*IDR+R)**3 -.333*((N-1.5)*IDR+R)**3
        DO 102 N=NOS,NO
        T(N)=TO
        A(N)=((N-NOS- .5)*DR+.1)**2
102     V(N)=.333*((N-NOS-.5 )*DR+.1)**3-.333*((N-NOS-1.5)*DR+.1)**3
        T(1) =TO
        KP=100
        BOND=R
        X=.10*IDR
        PI = (7.874 - D)/7.873
        ACRM = 50.
        SDV = 0.0
        DV= 0.0
        DM = X
        XN=X
        ALPL=.019
```

```
      HTRANS = SPIN*ALL*DL*CPL/R/2
      M=IDT*ALP/IDR
      CKM = ALPM*D*CPM
      CK=ALP*DS*CPS

                  T(N) = TEMPERATURE OF ELEMENT AT PREVIOUS TIME STEP
                  A(N) = AREA OF ELEMENT
                  V(N) = VOLUME OF ELEMENT
                  BOND = DISTANCE FROM THE CENTER OF THE SPHERE TO THE
                         MOVING BOUNDARY
                  X = DISTANCE FROM THE CENTER OF THE FURTHEST ELEMENT
                      TO THE MOVING BOUNDARY
                  ACRM = HEAT OF FUSION OF THE METAL SPHERE
                  SDV = TOTAL VOLUME OF METAL MELTED
                  DV = METAL MELTED IN A SINGLE TIME STEP
                  XN = MOVEMENT OF THE MOVING BOUNDARY IN ONE TIME STEP
                  HTRANS = HEAT TRANSFER COEFFICIENT

*******  MAIN LOOP OUTPUT AND PROPERTIES CALCULATIONS

88    BOND=BOND+XN
      IF(PORE)89,89,90
90    N = (NO + NOS)/2
      CKM = (42.0/T(N) + 0.0519)**(1 - PI)*(3.04E-04*(1 -
     C EXP(-7.65E-04*T(N))) + 3.66E-12*T(N)*T(N)*T(N)*PORE)**PI
      ALPM = CKM/D/CPM
89    TIME=I*IDT
      IF(TIME- NOT)87,200,200
87    IF(T(1)) 86,86,85
86    IDT  = IDT-IDT/10
      GO TO 200
85    IF(TI-T(1))86,86,84
84    T(NO)=T(1)
      KL = KL + 1
      J=J+1
      IF(KP- 5/IDT)4,5,5
```

```
5       WRITE(6,70)TIME,BOND,T(1),T(NOS),DM,GRD
        KP=0
4       KP=KP+1

                        TIME = TIME OF IMMERSION
                        CKM = THERMAL CONDUCTIVITY OF A POROUS IRON SPHERE
                        ALM = THERMAL DIFFUSIVITY OF A POROUS IRON SPHERE

*******  CALCULATION OF TEMPERATURES AT THERMOCOUPLE AND THROUGHOUT
                        METAL SPHERE
        HIN=3.587E-15*(T(NOS+1))**4-T(NOS)**4)+CORR      *(T(NOS-1)-T(NOS))
        E(NOS)=HIN*IDT*3/.001+T(NOS)
        GRD=-(E(NOS) - T(NOS))/(T(NOS)-TI)
        HOUT=A(NOS+1)*(T(NOS+2)-T(NOS+1))*ALPM/DR
        E(NOS+1)=(HOUT-HIN)*IDT*3/((DR*.5+.1)**3-.001)+T(NOS+1)
        NA=NOS+2
105     DO 51 N=NA,NOM
        HIN=A(N-1)*(T(N-1)-T(N))
        HOUT=A(N)*(T(N+1)-T(N))
51      E(N)=(HIN+HOUT)*ALPM*IDT/V(N)/DR+T(N)
        N=1

                        E(N) = TEMPERATURE OF ELEMENT AT PRESENT TIME STEP

*******  CALCULATION OF TEMPERATURES AT THE SURFACE OF SPHERE WITH A SLAG
                        SHELL THICKNESS LESS THAN IDR
        IF(R+IDR-BOND)108,108,103
103     HIN=-HOUT*CKM /DR
        VU = DS*CPS*(.333*(R + .5*X)**3 - R*R*R*.333)
        V1 = VU + CPM*D*.333*(R*R*R - (R - .5*DR)**3)
        IF(BOND - R)1031,1031,1032
1031    X = 0.0
        HOUT = R*R*HTRANS*(TI - T(1))
        E(1)=(HIN+HOUT)*IDT/V1       +T(1)
        BOND = R
        GO TO 203
```

```
1032  A1=(R+.5*X)**2
      HOUT=A1   *(TMS   -T(1))*CK  /X
      E(1)=(HIN+HOUT)*IDT/V1        +T(1)
      H=-ACR
      XN=IDT/H/DS*(CK*(T(1)-TMS )/X+(TI-TMSP)*HTRANS)
      BA=BOND+XN-R
      L=BA/IDR
      X=IDR*(BA/IDR-L )
      IF(DM - IDR/10.)9,9,8
9     DM = IDR/10
8     IF(X-IDT/10)7,203,203
7     X = IDR/10

******* CHECK FOR MELTING OF SPHERE AND RESET PREVIOUS TEMPERATURE
                    DISTRIBUTION

203   IF(T(1)        - TM    )106,198,198
198   IF(SDV-4.*R*R*R*3.1417/3) 1001,200,200
1001  QR=4.*3.1417*A(1)*CK*(T(2)-1357.)/IDR
      DV=IDT*QR/(D*ACRM)
      SDV=SDV+DV
      E(1)=TM
106   IF(NOT - NO)200,200,99
99    DO 705 K=1,NOM
705   T(K)=E(K)
      GO TO 88

******* CALCULATE TEMPERATURES AT THE SURFACE OF THE SPHERE AND THROUGHOUT
                    THE SOLID SLAG SHELL
108   HIN=-HOUT*CKM /DR
      HOUT=A(1)*(T(2)-T(1))*CK /IDR
      VU = DS*CPS*(.333*(R+.5*IDR)**3 - R*R*R*.333)
      V1 = VU + CPM*D*.333*(R*R*R - (R - .5*DR)**3)
      E(1)=(HIN+HOUT)*IDT/V1        +T(1)
109   N=N+1
      IF (R+(N   )*IDR-BOND)115,115,110
```

```
110     AX=(BOND-X/2.)*(BOND-X/2.)
        VX=.333*(BOND-X/2)**3-.333*(BOND-IDR/2-X)**3
        HIN=A(N-1)*(T(N-1)-T(N))/IDR
        HOUT=AX*(TMS -T(N))/X
        E(N)=(HIN+HOUT)*ALP*IDT/VX+T(N)
        H=-ACR
        XN=IDT/H/DS*(CK*(T(N)-TMS )/X+(TI-TMSP)*HTRANS)
        BA=BOND+XN-R
        L=BA/IDR
        X=IDR*(BA/IDR-L)
        IF(DM - IDR/10.)9,9,8
115     IF(N-NO+1)116,86,86
116     G=A(N-1)*T(N-1)   +A(N)*T(N+1)
        H=(M/V(N))*(A(N-1)+A(N))
        E(N)     =(M/V(N))*G+T(N)   *(1-H)
        IF(E(N)-TMS   )401,402,402
402     E(N)=TMS
401     GO TO 109
201     STOP
        END
```

PROGRAM FOR HEATING AN INFINITE CYLINDER IN LIQUID SLAG

```
        REAL M,IDT,IDR
        DIMENSION A(99),V(99),T(99),E(99)
200     READ(5,100)NO, NOT, NOS,NALP,NOME,IDR,IDT,TI,TO,TMS,TMSP
      C,ACR,ALP,SPIN,R,D,DS,CPL,CPS,U,CPM,CIN,DL,ALL
100     FORMAT(5I5/(8E10.4))
1002    WRITE(6,100)NO,NOT,NOS,NALP,NOME,IDR,IDT,TI,TO,TMS,TMSP
      C,ACR,ALP,SPIN,R,D,DS,CPL,CPS,U,CPM,CIN,DL,ALL
70      FORMAT( 8F10.4)
        IF(NO)201,201,50
```

```
50      DR=(R-.1)/(NO-NOS-1)
        WRITE(6,71)
71      FORMAT('  TIME      RADIUS     SURFACE     CENTER  CAL/CM2-SEC')
        NOM=NO-1
        ALPM= .093
        KL = 0
72      DO 101 N=1,NOS
        J=0
        F(N)=TMS
        A(N)=((N-.5)*DR+R)**2
101     V(N)=       ((N-.5)*DR+R)**2 -       ((N-1.5)*DR+R)**2
        DO 102 N=NOS,NO
        T(N)=TO
        A(N)=((N-NOS- .5)*DR+.1)**2
102     V(N)=       ((N-NOS-.5 )*DR+.1)**2-       ((N-NOS-1.5)*DR+.1)**2
        T(1) =TO
        KP=100
        BOND=R
        X=.10*IDR
        DM = X
        XN=X
        ALPL=.019
        HTRANS = SPIN*ALL*DL*CPL/R/2
        M=IDT*ALP/IDR
        CKM = ALPM*D*CPM
        CK=ALP*DS*CPS
88      BOND=BOND+XN
        TIME=J*IDT
        IF(T(NOS)-.99*TI)87,200,200
87      IF(T(1)) 86,86,85
86      IDT  = IDT-IDT/10
        WRITE(6,73) IDT
73      FORMAT('  IDT = CHANGED',F10.6)
        GO TO 72
85      IF(TI-T(1))86,86,84
84      T(NO)=T(1)
```

```
      KL = KL + 1
      J=J+1
      IF(KP-100)4,5,5
5     TH =(T(1)-T0)/(TI-T0)
      THM = (T(1)-T0)/(TMS-T0)
      WRITE(6,70)TIME,BOND,T(1),T(NOS),DM,GRD
      KP=0
4     KP=KP+1
      HIN=7.287E-14*(T(NOS+1)**4-T(NOS)**4)+ .04*ALPL*(T(NOS+1)-T(NOS))
      E(NOS)=HIN*IDT*2/ .01+T(NOS)
      GRD=-(E(NOS) - T(NOS))/(T(NOS)-TI)
      HOUT=A(NOS+1)*(T(NOS+2)-T(NOS+1))*ALPM/DR
      E(NOS+1)=(HOUT-HIN)*IDT*2/((DR*.5+.1)**2- .01)+T(NOS+1)
      NA=NOS+2
105   DO 51 N=NA,NOM
      HIN=A(N-1)*(T(N-1)-T(N))
      HOUT=A(N)*(T(N+1)-T(N))
51    E(N)=(HIN+HOUT)*ALPM*IDT/V(N)/DR+T(N)
      N=1
      IF(R+IDR-BOND)108,108,103
103   HIN=-HOUT*CKM /DR
      VU = DS*CPS*(      (R + .5*X)**2 - R*R)
      V1 = VU + CPM*D*      (R*R    - (R - .5*DR)**2)
      IF(BOND - 2)1031,1031,1032
1031  X = 0.0
      HOUT = 2*R*HTRANS*(TI - T(1))
      E(1)=(HIN+HOUT)*IDT/V1       +T(1)
      BOND = R
      GO TO 203
1032  A1=(R+.5*X)*2
      HOUT=A1   *(TMS   -T(1))*CK /X
      E(1)=(HIN+HOUT)*IDT/V1       +T(1)
      H=-ACP
      XN=IDT/H/DS*(CK*(T(1)-TMS )/X+(TI-TMSP)*HTRANS)
      BA=BOND+XN-R
      L=BA/IDR
```

```
      X=IDR*(BA/IDR-L)
      IF(DM - IDR/10.)9,9,8
9     DM = IDR/10
8     IF(X-IDT/10)7,203,203
7     X = IDR/10
203   IF(NOT - NO)200,200,99
99    DO 705 K=1,NOM
705   T(K)=E(K)
      GO TO 88
108   HIN=-HOUT*CKM /DR
      HOUT=A(1)*(T(2)-T(1))*CK /IDR
      VU = DS*CPS*(      (R+.5*IDR)**2 - R*R)
      V1 = VU + CPM*D*      (R*R    - (R - .5*DR)**2)
      E(1)=(HIN+HOUT)*IDT/V1       +T(1)
109   N=N+1
      IF (R+(N  )*IDR-BOND)115,115,110
110   AX=(BOND-X/2.)*2
      VX=      (BOND-X/2)**2-      (BOND-IDR/2-X)**2
      HIN=A(N-1)*(T(N-1)-T(N))/IDR
      HOUT=AX*(TMS -T(N))/X
      E(N)=(HIN+HOUT)*ALP*IDT/VX+T(N)
      H=-ACP
      XN=IDT/H/DS*(CK*(T(N)-TMS )/X+(TI-TMSP)*HTRANS)
      BA=BOND+XN-R
      L=BA/IDR
      X=IDR*(BA/IDR-L)
      IF(DM - IDR/10.)9,9,8
115   IF(N-NO+1)116,86,86
116   G=A(N-1)*T(N-1)   +A(N)*T(N+1)
      H=(M/V(N))*(A(N-1)+A(N))
      E(N)     =(M/V(N))*G+T(N)   *(1-H)
      IF(E(N)-TMS  )401,402,402
402   E(N)=TMS
401   GO TO 109
201   STOP
      END
```

PROGRAM FOR HEATING AND MELTING A POROUS IRON SPHERE IN AN ELECTRIC FURNACE

```
      REAL M,IDT,IDR,NU
      DIMENSION A(99),V(99),T(99),E(99)
200   READ(5,100)NO, NOT, NOS,NALP,NOME,IDR,IDT,TI,TO,TMS,TMSP
     C,ACR,ALP,SPIN,R,D,DS,CPI ,CPS,U   ,CPM
100   FORMAT(5I5/(8F10.4))
1002  WRITE(6,100)NO,NOT,NOS,NALP,NOME,IDR,IDT,TI,TO,TMS,TMSP
     C,ACR,ALP,SPIN,R,D,DS,CPI ,CPS,U   ,CPM
70    FORMAT( 8F10.4)
      IF(NO)201,201,50
50    DR=(R-.1)/(NO-NOS-1)
      WRITE(6,71)
71    FORMAT('  TIME     RADIUS     SURFACE   CENTER    INTERFACE HTRANS
     C  PENETRATE METAL K')
      NOM=NO-1
      DO 101 N=1,NOS
      E(N)= TMS
      A(N)=((N-.5)*IDR+R)**2
101   V(N)=.333*((N-.5)*IDR+R)**3 -.333*((N-1.5)*IDR+R)**3
      DO 102 N=NOS,NO
      T(N)=TO
      A(N)=((N-NOS- .5)*DR+.1)**2
102   V(N)=.333*((N-NOS-.5 )*DR+.1)**3-.333*((N-NOS-1.5)*DR+.1)**3
      T(1) =TO
      ACRM=  65.
      KP=50
      ROND=R
      X=.10*IDR
      XN=X
      HSLAG = .081
      HMET = 3.17
      ALPL=.019
      PI = (7.874 - D)/7.873
      SLAG = 30.
      DROP = 0.0
      RADIUS = R
```

```
      PEN = R
      J=0
      R=6.
      C=.0018
      ALP=ALP*10/NALP
      M=IDT*ALP/IDR
      CK=ALP*DS*CPS
88    BOND=BOND+XN
      N = (NO + NOS)/2
      CKM = (42.0/T(N) + 0.0519)**(1 - PI)*(3.04E-04*(1 -
     C EXP(-7.65E-04*T(N))) + 3.66E-14*T(N)*T(N)*T(N))**PI
      ALPM = CKM/D/CPM
       IF(DR + .1- BOND)85,85,204
204   RATE = D*RADIUS/TIME
      WRITE( 6,70)RATE,TIME
      GO TO 200
85    T(NO)=T(1)
      TIME=J*IDT
      VT = BOND*BOND*BOND*4.189
      VM = R*R*R*4.189
      DTOT  = DS* (VT -VM)/VT + D          *VM/VT
      IF(SLAG - DROP)1050,1050,1055
1055  VEL = 163*BOND*BOND*  (DTOT-DS)/    U
      DROP = DROP + VEL*IDT
      HTRANS = 0.69*VEL**.5*DS**1.167*ALP**.67*CPL/BOND**.5/U**.167/.14
      HTRANS = HTRANS + ALP*DS*CPL/BOND
      GO TO 1060
1050  VM = VT*(DTOT - DS)/(7.874 - DS)
      PEN=(2*BOND*BOND*BOND - 3*VM/3.1417) /(3*BOND*BOND - PEN*PEN)
      ST = BOND*BOND*12.57
      IF(PEN)1051,1052,1052
1051  SM =ST- ( 4.93    *    BOND*BOND + 3.1417*PEN*SQRT(BOND*BOND
     C -PEN*PEN) - 3.1417*PEN*PEN* ARSIN(-PEN/BOND))
      HTRANS = SM/ST*HMET + (ST-SM)/ST*HSLAG
      GO TO 1060
1052  SM =       4.93    *    BOND*BOND - 3.1417*PEN*SQRT(BOND*BOND
     C -PEN*PEN) - 3.1417*PEN*PEN* ARSIN(PEN/BOND)
```

```
      HTRANS = SM/ST*HMET + (ST-SM)/ST*HSLAG
1060  J=J+1
      IF(KP-50)4,5,5
5     WRITE(6,70)TIME,BOND,T(1),T(NOS), XN    ,HTRANS,PEN,CKM
      KP=0
4     KP=KP+1
      HIN=3.587E-15*(T(NOS+1)**4-T(NOS)**4)+.001*ALPL*(T(NOS+1)-T(NOS))
      E(NOS)=HIN*IDT*3/.001+T(NOS)
      HOUT=A(NOS+1)*(T(NOS+2)-T(NOS+1))*ALPM/DR
      E(NOS+1)=(HOUT-HIN)*IDT*3/((DR*.5+.1)**3-.001)+T(NOS+1)
      NA=NOS+2
      IF(E(1) - 1800.)105,198,198
198   DO 52 N=NA,NO
      IF(DR*(N - NOS - 1)- BOND + .1)197,199,199
199   AX = (BOND- X/2)*(BOND - X/2)
      VX = .333*(BOND - X/2)**3 - .333*(BOND - DR/2-X)**3
      HIN = A(N-1)*(T(N-1) -T(N))/DR
      HOUT = AX*(1800.-T(N))/X
      E(N) = (HIN + HOUT)*ALPM*IDT/VX + T(N)
      H = -ACRM
      XN = IDT/H/(D          )*(CKM *(T(N) - 1800.)/X + (TI -1800.)*
     C HTRANS )
      R = BOND + XN
      BA = BOND + XN - .1
      L = BA/DR
      X = DR*(BA/DR - L)
      IF(X-DR/10)8,106,106
8     X = DR/10
      GO TO 106
197   HIN=A(N-1)*(T(N-1)-T(N))
      HOUT=A(N)*(T(N+1)-T(N))
52    E(N)=(HIN+HOUT)*ALPM*IDT/V(N)/DR+T(N)
      GO TO 200
105   DO 51 N=NA,NOM
      HIN=A(N-1)*(T(N-1)-T(N))
      HOUT=A(N)*(T(N+1)-T(N))
51    E(N)=(HIN+HOUT)*ALPM*IDT/V(N)/DR+T(N)
      IF(R - BOND)87,86,86
```

```
86      HIN = -HOUT*CKM /DR
        A1 = R*R
        HOUT = A1*(TI - T(1))*HTRANS
        V1 =(.333*R*R*R -.333*(R-.5*DR)**3)/J/CPM
        E(1) = (HIN + HOUT)*IDT/V1 +T(1)
        XN = 0.0
        GO TO 106
87      N=1
        IF(R+IDR-BOND)108,108,103
103     HIN=-HOUT*CKM /DR
        A1=(R+.5*X)**2
        HOUT=A1  *(TMS  -T(1))*CK /X
        VU = DS*CPS*(.333*(R + .5*X)**3 - R*R*R*.333)
        V1 = VU + CPM*D*.333*(R*R*R - (R - .5*DR)**3)
        E(1)=(HIN+HOUT)*IDT/V1       +T(1)
        H=-ACR
        XN=IDT/H/DS*(CK*(T(1)-TMS )/X+(TI-TMSP)*HTRANS)
        BA=BOND+XN-R
        L=BA/IDR
        X=IDR*(BA/IDR-L)
        IF(X-IDR/10)7,203,203
7       X = IDR/10
203     IF(E(1)       -1800.0)106,205,205
205     X = DR
        BOND = R
106     IF(NOT-J)200,200,99
99      DO 705 K=1,NOM
705     T(K)=E(K)
        GO TO 88
108     HIN=-HOUT*CKM /DR
        HOUT=A(1)*(T(2)-T(1))*CK /IDR
        VU = DS*CPS*(.333*(R+.5*IDR)**3 - R*R*R*.333)
        V1 = VU + CPM*D*.333*(R*R*R - (R - .5*DR)**3)
        E(1)=(HIN+HOUT)*IDT/V1       +T(1)
109     N=N+1
        IF (R+(N  )*IDR-BOND)115,115,110
110     AX=(BOND-X/2.)*(BOND-X/2.)
```

```
      VX=.333*(BOND-X/2)**3-.333*(BOND-IDR/2-X)**3
      HIN=A(N-1)*(T(N-1)-T(N))/IDR
      HOUT=AX*(TMS -T(N))/X
      E(N)=(HIN+HOUT)*ALP*IDT/VX+T(N)
      H=-ACR
      XN=IDT/H/DS*(CK*(T(N)-TMS )/X+(TI-TMSP)*HTRANS)
      BA = BOND+XN-R
      L=BA/IDR
      X=IDR*(BA/IDR-L)
      IF(X-IDR/10)7,203,203
115   G=A(N-1)*T(N-1)   +A(N)*T(N+1)
      H=(M/V(N))*(A(N-1)+A(N))
      F(N)     =(M/V(N))*G+T(N)   *(1-H)
      IF(E(N)- TMS )401,402,402
402   E(N)=TMS
401   GO TO 109
201   STOP
      END
```

APPENDIX E. RADIATION HEAT TRANSFER IN A BOUNDARY LAYER

This appendix presents the mathematics for calculating the relative amounts of heat transfered by radiation and conduction in a fluid boundary layer at steady state.

Heat Transfer by Conduction

The system consists of a solid adjacent to a liquid slag with a smooth interface separating the two phases as shown in Figure E-1. The solid material is either metal or frozen slag. In the latter case the interface moves according to the balance presented in Chapter V, and the temperature at the interface is at the solidus temperature of the slag. Radiation through the bulk of the frozen slag shell is neglected due to the high extinction coefficient caused by the absorption and scattering of the photons by the crystalline slag.

The liquid slag is bounded by the metal or solid slag on one side and unbounded on the other. The heat conduction from the liquid to the solid through the boundary layer is represented by a mean heat transfer coefficient, $\bar{h}_L$. The heat transfer coefficient is a function of the fluid motion and is assumed to be constant. If radiation heat transfer is neglected, the heat flux, q_c, to the surface of the solid depends on the heat transfer coefficient, h_L, the surface temperature, T_S, and the bulk liquid temperature, T_∞, as shown in Equation (1)

$$q_c = \bar{h} (T_\infty - T_S) \qquad (1)$$

With the addition of radiation heat transfer, the total heat flux is

$$Q = q_c + q_r$$

when coupling between the radiation and conduction is neglected.

Heat Transfer by Radiation

Radiation is only significant in the liquid phase. One can solve the radiation transport equations for a region bounded by the surface of the slag at its melting temperature and the infinite bulk of liquid slag. This solution is done in one dimension considering energy balances at an arbitrary element in the liquid of width dx_o (41).

The element dx_o shown in Figure E-1 is at steady state, the radiation received must be equal to the radiation emitted.

$$I_{x-} + I_{x+} = 2Ix_o \tag{1}$$

Also because there is a net flow of heat through the plane at x_o

$$I_{x+} - I_{x-} = q_r \tag{2}$$

Subtracting the Equations (1) and (2)

$$2I_{x-} = 2Ix_o - q_r \tag{3}$$

where $I_{x-} = \alpha_o' I_f e^{-\beta x_o} + \int_o^{x_o} \beta I e^{-\beta(x_o - x)} dx$

α_o' = (1-r) fraction adsorbed + fraction transmitted x_o

I_f = radiation from solid surface

β = absorption coef.

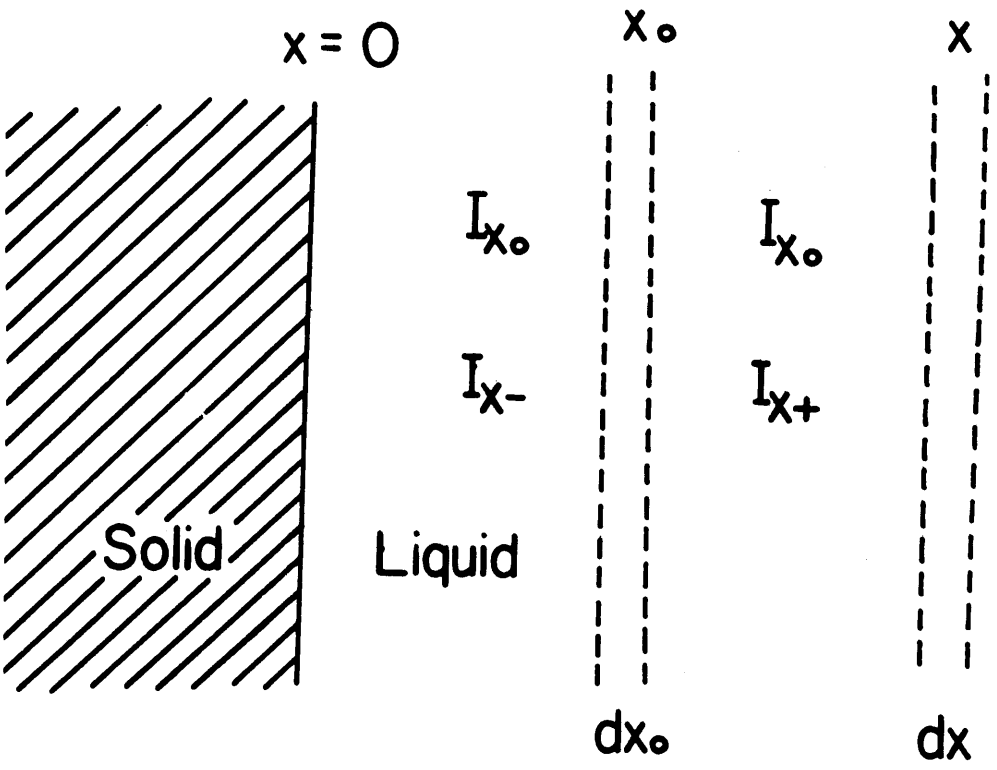

Figure E-1 Radiating liquid bounded by a solid

Equation (3) becomes

$$2\int_{o}^{x_o} \beta I e^{-\beta(x_o-x)}\, dx = 2I_{x_o} - 2\alpha_o' I_f e^{-\beta x_o} - qr \qquad (4)$$

To remove the integral, Leibnitz rule is applied to the differentiation of Equation (4) with respect to x_o.

That is

$$\frac{d\left(\int_{o}^{x_o} \beta I e^{-\beta(x_o-x)}\, dx\right)}{dx_o} = \int_{o}^{x_o} \frac{d(\beta I e^{-\beta(x_o-x)}}{dx_o}\, dx$$

$$+ \beta I e^{-\beta(x_o-x)} \Big|_{x=x_o} \frac{dx_o}{dx_o} - \beta I e^{-\beta(x_o-x)} \Big|_{x=0} \frac{d(o)}{dx_o}$$

$$= \int_{o}^{x_o} -\beta^2 I e^{-\beta(x_o-x)} + \beta x_o$$

And Equation (4) becomes upon differentiation with respect to x_o

$$2\int_{o}^{x_o} -\beta^2 I e^{-\beta(x_o-x)}\, dx + 2\beta I_o = \frac{2dI_{x_o}}{dx_o} + 2\alpha_o'\beta I_f e^{-\beta x_o} \qquad (5)$$

Dividing Equation (5) by β and adding it to Equation (4) results in

$$q_r\, \beta dx_o = 2dI_{x_o} \qquad (6)$$

Thus (6) is integrated over the limits

at $x_o = 0$, $I_{x_o} = I_f$

at $x_o = x$, $I_{x_o} = I$

Resulting in $I_f - I = \frac{q_r \beta x}{2}$ (7)

which gives the temperature distribution if

$$I = \sigma T^4$$

$$I_f = \sigma T_S^4$$

If the heat transfer coefficient represents a linear boundary layer, δ,

$$h = \frac{\delta}{K_c}$$

where K_c is thermal conductivity of the liquid. The net heat flux due to radiation through the boundary layer is

$$q_r = \frac{-\sigma 2 (T_S^4 - T_\infty^4)}{\beta \delta} = \frac{(T_\infty^4 - T_S^4)\ \sigma 2h}{\beta K}$$

Then the total fraction of heat transfer by radiation is

$$f_{rad} = \frac{q_r}{q_r + q_c} = \frac{(T_\infty^4 - T_S^4)\ \sigma 2}{(T_\infty^4 - T_S^4)\sigma 2 + \Delta T \beta K_c}$$

It should be noted that the above calculations are based on the assumption that the solid surface acted as a black body and that the liquid slag acted as a grey medium. The assumption of a black body for nickel may be very good if there is an oxide layer on the surface (likewise true for iron). But crystalline slags have emissivities of the order of 0.6 to 0.8 and therefore may scatter much of the radiation back into the liquid. This would have the effect of increasing the thermal gradient at the solid surface, but on the whole the radiation heat transfer would be less due to less absorption at the surface.

APPENDIX F. CHEMICAL ANALYSIS OF THE SLAGS

A total iron analysis was performed on the ferrous silicate slags. Powdered slag samples, which were taken from the liquid slag, were dissolved in hot hydrochloric acid or fused with molten calcium carbonate and then dissolved in the acid. Once in an aqueous solution the iron present was reduced to Fe^{++} by reduction with tin (II) chloride and titrated with a potassium permaganate solution. A Zimmermann-Reinhardt reagent was used to inhibit the oxidation of the chloride ions by the permanganate (73). The detailed procedure for the iron analysis is presented by Skoog and West (73).

Comparisons between the total iron calculated from the mixed reagent powders and the total iron from the analysis are shown in Table III-1. The agreement is good except for the synthetic copper smelting slag N-1CU. The excess iron which is present in this slag is the result of oxidation of the iron crucible by the Fe_2O_3.

Slag samples were taken just after the initial melting of a powder and also after several hours of experiments with the slag. These samples were analyzed for total iron, and there was no more than 0.1% variation in iron present. Such a small change in the iron content would have a negligible effect on the thermal conductivity or melting range of the slag.

APPENDIX G. SIMILARITY BETWEEN THE SLAG AND THE GLYCEROL SOLUTION

The principle parameters which characterize the motion of bubbles (36) are the bubble Reynolds number

$$N_{Re_b} = \frac{d_b u \rho_L}{\mu}$$

where d_b is the diameter of a sphere of equal volume to the bubble

u is the velocity of the rising bubble

ρ_L is the density of the liquid

μ is the viscosity of the liquid

the Weber number

$$N_{We} = \frac{d_b u^2 \rho_L}{\sigma_s}$$

where σ_s is the surface tension

The Morton number

$$N_{Mo} = \frac{g\mu}{\rho_L g^3 \sigma^3}$$

where g is the gravitational constant.

Although there is a limited amount of data on the relationship between bubble velocity and bubble size for a variety of gas liquid systems, an empirical relationship has been derived by Davies and Taylor (80) which is independent of the properties of the liquid

$$u = 1.02 \left(\frac{g d_b}{2}\right)^{1/2}$$

This relationship appears to hold true for equivalent bubble diameters between 0.2 cm. to 4 cm.

For the formation of a bubble at a orifice, the mean bubble diameter appears to be related to the orifice Reynolds number

$$N_{Re_o} = \frac{d_o V_o \rho_L}{\mu}$$

where d_o is the diameter of the orifice and V_o is the velocity of the gas at the orifice. Since the orifice is the same in both the slag and the glycerine experiments, the similarity between the bubble diameters of the two systems depends only on the kinematic viscosity $\frac{\mu}{\rho_L}$. Also, since the rising velocity of a bubble is independent of the properties of the liquid, similarity in the motion of the bubble depends only on the kinematic viscosity. For the glycerol 10% water system the kinematic viscosity is

$$\frac{\mu}{\rho_L} = \frac{1 \text{ poise}}{1.25 \text{ g/cm}^3} = 0.80 \text{ cm}^2/\text{sec}.$$

For the slag N-1CU the kinematic viscosity is estimated from the properties presented in Chapter V.

$$\frac{\mu}{\rho_L} = \frac{2}{3.5} = 0.57 \text{ cm}^2/\text{sec}.$$

The similarity is not perfect, as the kinematic viscosity of the glycerol solution is somewhat higher than the slag. The higher viscosity may result in slightly larger bubbles in the glycerol solution.

REFERENCES

1. J.F. Elliott: Can. Met. Quart., vol. 14, No.3, 1975, pp. 199-204.

2. J.F. Elliott and J.D. Nauman: Proceeding, Symposium on Metal-Slag Gas Reactions and Processes, Electrochem. Soc., Toronto, Canada, 1975, pp. 283-250.

3. H.A. Fine, T. Engh, and J.F. Elliott: Met. Trans. B., 1976, pp. 277-85.

4. J.Nauman, G. Foo, and J. Elliott: Proceeding, Symposium on Copper Extraction and Refining, AIME, Las Vegas, Nevada, 1976, pp. 237-58.

5. T. Murase and A. McBrirney: Science, vol. 170, 1970, p. 165.

6. R.L. Gibby and J.L. Bates: Proceedings, Tenth Thermal Conductivity Conf., Newton, Mass., Sept. 28-30, IV, 1970, pp. 7-8.

7. J.L. Bates: Proceedings, Sixth International Conference on Magnetohydrodynamic Electrical Power Generation, vol. II, Open Cycle Components and Materials, Washington, D.C., June 9-13, 1975.

8. Y.E. Lee, and D.R. Gaskell: Met. Trans., 1964, vol. 5, p. 853.

9. Y.S. Touloukian, R.W. Powell, C.Y. Ho, and P.G. Klemers; eds., Thermophysical Properties of Matter, Plenum Publishing Co., New York, 1970.

10. K.K. Kelley: Bul. 393, U.S. Bureau of Mines, 1936.

11. F. Kreith, L.G. Roberts, J.A. Sullivan, and S.N. Sinha: Intern. J. Heat Mass Transfer, vol. 6, 1976, p. 885.

12. M. Bogdanska, W.S. Brzozowski, J. Charuba, K. Dabrowski, M. Plata, M. Zielinski: Proceedings, Sixth International Conference on Magnetohydrodynamic Electrical Power Generation, vol.II, Open Cycle Components and Materials, Washington, D.C., June 9-13.

13. H.G. Braun: Int. Z. Gaswarme, vol. 15, No.7, 1966, pp. 207-18.

14. J.G. Sibakin, P.H. Hookings, and G.A. Roeder: J. Iron Steel Inst., October 1967, pp. 1005-17.

15. A. Mitchell and S. Joshi: Met. Trans., vol. 4, 1973, pp. 631-42.

16. H. Hales: Sc.D. Thesis, Mass. Inst. Tech., 1967.

17. P.L.T. Brian, H.B. Hales, and T.K. Sherwood: AICHE J., vol. 15, No. 5, 1969, pp.727-32.

18. H. B. Jensen: Iron and Steel Engr., Nov. 1972, pp. 59-66.

19. E.L. Foleman, D.O. Gloven, H.B. Jensen: Blast Furn. Steel Plant, Oct. 1970, pp. 733-43.

20. I. Yaron and B. Gal-Or, Int. J. Heat Mass Transfer, vol. 14, 1971, pp. 727-37.

21. P.H. Calderbank and M.B. Moo-Young, Chem. Eng. Sci., Vol. 16, 1961, pp. 39-54.

22. H.S. Carslaw and J.C. Jaeger: Conduction of Heat in Solids, 2nd ed., Oxford University Press, 1959, pp. 282-96.

23. W.S. Chang: Int. J. Heat Mass Transfer, vol. 16, 1963, pp. 2275-96.

24. G. Tripathi, K.N. Shukla, and R.N. Pandey: Int. J. Heat Mass Transfer, vol. 18, 1975, pp. 351-62.

25. K. Stepan: Int. J. Heat Mass Transfer, vol. 12, 1969, pp. 199-124.

26. T.G. Theofanous and H.C. Lim: Chem. Eng. Sci., vol. 26, 1971, pp. 1297-1300.

27. T.E. Cooper and G.J. Trezek: Cryobiology, vol. 7, Nos. 4-6, 1971, pp. 183-90.

28. Y. Chuang, and O. Ehrich: Int. J. Heat Mass Transfer, vol. 17, 1974, pp. 945-53.

29. Y.K. Chuang and J. Szekely: Int. J. Heat Mass Transfer, vol. 14, 1971, pp. 1285-94.

30. R.H. Tien and G.E. Geiger: Trans. ASME, J. Heat Transfer, Aug. 1967, pp. 230-4.

31. R.H. Tien: Trans. AIME, vol. 242, 1968, pp. 1289-92.

32. Y. Kinm and R.D. Pehlke: Met. Trans. B., vol. 6B, 1975, pp. 585-91.

33. J. Crank: Quart. J. Mech. App. Math., vol. 10, 1957, pp. 220-31.

34. M. Cable and D.J. Evans: J. App. Phys., vol. 38, No. 7, 1967, pp. 2899-906.

35. J. Szekely and R.G. Lee, Trans. Met. Soc. AIME, vol. 209, 1968, p. 961.

36. J. Szekely and N.J. Themelis: Rate Phenomena in Process Metallurgy, Wiley-Interscience, New York, 1971.

37. G.M. Dusinberre: Heat Transfer Calculations by Finite Differences, International Textbook Co., 1961.

38. J.G. Elliott, M. Gleiser, and V. Ramakrishna: Thermochemistry for Steelmaking, vol. II, Addison-Wesley Press, No. Reading, Mass., 1965.

39. Y.S. Touloukan, Ed.: Thermophysical Properties of High Temperature Solid Materials, The Macmillan Co., New York, 1967.

40. W.A. McAdams: Heat Transmission, 3rd ed., McGraw Hill Book Co., 1954.

41. R.H. Essenhigh: AIAA Themophysics Specialist Conference, No. 67-287, New Orleans, Louisiana, April 17-20, 1967.

42. E.M. Levin, C.R. Robbins, and H.F. McMurdie: Phase Diagrams for Ceramists, Am. Cer. Soc., 1964.

43. M. Ben-Amoz: Int. J. Eng. Sci., vol. 8, 1970, pp. 39-47.

44. G.P. Marino: WAPD-TM-807, UC-25, U.S. Atm. Energy Com., Feb. 1970.

45. M.S. Kolansky and R. Pfeffer: Int. J. Heat Mass Transfer, vol. 17, 1974, pp. 1425-36.

46. A.R.H. Cornish, Trans. Instn. Chem. Engrs., vol. 43, 1965, pp. 332-3.

47. J.C.Y. Koh and A. Fortini: Int. J. Heat Mass Transfer, vol. 16, 1973, pp. 2013-22.

48. W. Woodside and J.H. Messmer: J. Appl. Phys., vol. 32, No. 9, 1961, pp. 1688-1711.

49. D.L. Swift: Int. J. Heat Mass Transfer, vol. 9, 1966, pp. 1061-74.

50. M. Eisenberg, C.W. Tobias, and C.R. Wilke: Chem. Eng. Progr. Symp. Ser., vol. 51, No. 16, 1955, p. 1.

51. G.H. Garner and J.M. Hoffman: AICHE J., vol. 7, 1961, p. 148.

52. M. Fowler: Quart. of Appl. Math., vol. 3, 1945, p. 4.

53. M.T. Hsu, K. Sato, and B.H. Sage: Ind. Eng. Chem., vol. 46, p. 870.

54. F.A.M. Schenkels and J. Schenk: Chem. Eng. Sci., vol. 24, 1969, p. 585.

55. A.H.P. Skelland and A.R.H. Cornish: AICHE J., vol. 9, 1963, p. 73.

56. T.K. Sherwood, R.L. Pigford, and C.R. Wilke: Mass Transfer, McGraw Hill Book Company, New York, 1975.

57. R.A. Smith: M.S. Thesis, Mass. Inst. Tech., 1967.

58. I. Yaron and B. Gal-Or: Int. J. Heat Mass Transfer, vol. 14, 1971, pp. 727-37.

59. B. Gal-Or and S. Waslo: Chem. Eng. Sci., vol. 33, 1968.

60. H. Yoshitome, Y. Mannami, K. Mukai, T. Kanazawa, and N. Yoshikoshi: Chem. Eng. (Japan), vol. 29, No. 1, 1965, pp. 19-25.

61. K. Shermer: Ironmaking Steelmaking Quart., No. 3, 1975, pp. 188-92.

62. K. Nakaniski, T. Fugii, and J. Szekely: Ironmaking Steelmaking Quart., No. 3, 1975, pp. 193-8.

63. M. C. Flemings: Solidification Processing, McGraw-Hill Book Company, New York, 1974.

64. H.F. Taylor, M.C. Flemings, and J. Wulff: Foundry Engieering, John Wiley and Sons, Inc., New York 1959.

65. J.D. Hunt and K.A. Jackson: Trans. AIME, vol. 236, 1966, p. 843.

66. G.H. Geiger and D.R. Poirier: Transport Phenomena in Metallurgy, Addison-Wesley Publishing Company, Reading, Mass., 1973.

67. W. Kingery, H. Bowen and D. Uhlmann: Introduction to Ceramics, Wiley, New York, 1976.

68. B. Boulton, and J.J. Taylor: Inst. of Fuel J., 1963, p. 463.

69. V.N. Golovin, Thermal Eng., vol. 12, No. 4, 1965, p. 56.

70. G.W. Morey: The Properties of Glass, Reinhold, New York, 1954.

71. M. Jakobi: Heat Transfer, vols. I and II, Wiley, New York, 1944.

72. A. Maun and E.F. Osborn: Phase Equilibria Among Oxides in Steelmaking, Addison-Wesley Publishing Co., Reading, Mass., 1965.

73. D.A. Skoog, and D.M. West: Fundamentals of Analytical Chemistry, Holt, Rinehart and Winston, Inc., New York, 1969.

74. N.D. Eryou and L.R. Glicksman: J. Heat Trans., vol. 94, 1972, pp. 224-34.

75. F. Megerlin: Dis. TH Aachen, 1965.

76. A.L. Loeb: J. Amer. Cer. Soc., vol. 37, No. 2, 1954, pp. 96-9.

77. C.C. Reynolds: Simulation, Jan. 1968, pp. 29-36.

78. W.E. Ranz and W.F. Marshall: Chem. Eng. Prog., vol. 48, 1952, p. 141.

79. K. Aminzadeh, T.R. AlTaha, A.R.H. Cornish, M.S. Kolansky, and R. Pfeffer: Int. J. Heat Mass Transfer, vol. 17, 1974, pp. 1425-36.

80. R.M. Davies and G.I. Taylor: Proc. Roy. Soc. (London), A200, 1950, p. 375.

BIOGRAPHICAL NOTE

The author was born November 1950 in Rapid City, South Dakota. He graduate from Rapid City High School in 1969.

The author graduated from South Dakota School of Mines and Technology in January 1973 with the degree of Bachelor of Science in Chemistry. He entered Massachusetts Institute of Technology in June 1973 as a candidate for the degree of Doctor of Science in Metallurgy.

He was married to Barbara Jo Wallace on September 25, 1973.

He is a member of AIME, ASM, and ECS.